To the Graduate Council:

I am submitting herewith a dissertation written by George Hutchinson Neilson, Jr. entitled "Charge Exchange Measurements of Ion Behavior in the ISX Tokamak." I recommend that it be accepted in partial fulfillment of the requirements for the degree of Doctor of Philosophy, with a major in Physics.

Edward G. Harris, Major Professor

We have read this dissertation
and recommend its acceptance:

Accepted for the Council:

Vice Chancellor
Graduate Studies and Research

CHARGE EXCHANGE MEASUREMENTS OF ION BEHAVIOR IN THE ISX TOKAMAK

A Dissertation
Presented for the
Doctor of Philosophy
Degree
The University of Tennessee, Knoxville

George Hutchinson Neilson, Jr.

December 1979

ACKNOWLEDGMENTS

The work reported in this document was performed in the context of the experimental program of the Impurity Study Experiment at the Oak Ridge National Laboratory. Accordingly, the author is grateful to the Laboratory, and in particular, to his supervisors, L. A. Berry and J. Sheffield, and to the members of the ISX group, whose encouragement and indulgence were indispensable to the completion of this thesis.

The author especially wishes to thank J. F. Lyon, M. Murakami, S. L. Milora, and H. C. Howe for their scientific guidance and contributions to this effort. Thanks are also due Dr. J. P. Girard of the Centre d'Etudes Nucleaires, Fontenay-aux-Roses, France, whose own work and cooperation with the author started him in the right direction. The contributions of H. C. Sanderson, R. E. Worsham, and J. J. Schmitt in design and engineering are also acknowledged, as are the technical contributions of L. A. Massengill. The computer systems development efforts of D. R. Overbey are greatly appreciated, as they made possible the acquisition and analysis of a voluminous data base. Thanks also go to the ISX operations and maintenance crews, particularly T. F. Rayburn, W. J. Redmond, H. C. Boyd, G. D. King, C. W. McCullah, M. L. Peterson, E. E. Purdy, and B. S. Turner. Data which are the result of the ISX group's effort have been used extensively; acknowledgments of specific contributions are made throughout the text.

I am especially indebted to those who assisted in the final preparation of this thesis: Ms. Janice Cox and members of the F. E. D. Communications staff.

Finally, no acknowledgment can possibly encompass the dimensions of the sacrifices made by my wife, Linda, and daughter, Rebecca, so it can only be hoped that the final completion of this thesis and return to a normal existence will suffice.

ABSTRACT

Analysis of charge exchange neutrals is the standard method for measuring ion behavior in tokamak plasmas. Limitations of this technique, which arise in dense and neutral beam heated plasmas, are discussed. Two refinements which address these limitations are described: a neutral particle analyzer which incorporates both mass and energy resolution to distinguish different ion components such as the fast and thermal ions in beam-heated plasmas; and an improved data analysis procedure which accounts for the effects of profiles and neutral attenuation in dense plasmas. A simple 2D Monte Carlo neutral transport code was developed and used to investigate the effects of toroidally asymmetric neutral density profiles. Applications of these methods to experiments in ISX are discussed; they include energy confinement studies on ISX-A, neutral beam heating and high beta studies on ISX-B, and pellet fueling studies on ISX-B.

TABLE OF CONTENTS

LIST OF TABLES

LIST OF FIGURES

CHAPTER 1

INTRODUCTION: TOKAMAKS

Since the late 1960's and early 1970's substantial progress has been made towards the development of systems for the generation of commercial power by controlled thermonuclear fusion. In their simplest form, the requirements for reaching this goal are expressed in terms of the Lawson criterion, which states that a deuterium-tritium plasma at a temperature of about 6 to 10 keV must be confined with a density-confinement time product of about 10^{14} cm^{-3}-s, to achieve "breakeven" conditions. Two general types of confinement system have been pursued: inertial confinement, typified by the laser implosion scheme, in which the confinement times are short, less than 1 ns, and the densities very high, greater than 10^{24} cm^{-3}; and magnetic confinement, which utilizes magnetic fields to confine plasmas at densities ranging from 10^{13}-10^{18} cm^{-3} for confinement times of 0.1 to 100 ms. Much of the progress in the latter area may be attributed to the development of the tokamak,[1,2] a toroid-shaped magnetic confinement system, developed in the U.S.S.R. in the 1950's and 1960's. The experimentally measured confinement properties of the Soviet tokamak, T-3, reported in 1968 by a team of Soviet scientists headed by Academician L. A. Artsimovich[3], were so favorable that the concept quickly became the focus for both experimental and theoretical physics research in fusion laboratories throughout the world.

At this time, the tokamak concept is being pursued in the United States as the most promising candidate for a fusion reactor core. Accordingly, there are five major confinement-oriented tokamaks and several basic research tokamaks now operating in this country. A tokamak designed to achieve breakeven, that is, to produce fusion power equal to the power input to the plasma, is the Tokamak Fusion Test Reactor (TFTR), now under construction at the Princeton Plasma Physics Laboratory and scheduled to begin operation in 1982. Major tokamak experimental programs are also being carried out in the U.S.S.R., United Kingdom, France, Germany, Italy, and Japan. TFTR-class breakeven experiments being planned and/or built abroad include JET (Joint European Tokamak), and JT-60 (Japan).

The research reported in this document was performed in the context of one of these confinement programs, the Impurity Study Experiment (ISX), at the Oak Ridge National Laboratory. A photograph of the ISX-B tokamak is shown in Fig. 1-1, and the major parameters of the device, in both its "A" and "B" configurations, are given in Table 1-1.[4] Some of the motivation for the work was drawn from an earlier ORNL experiment, the Oak Ridge Tokamak (ORMAK). In this chapter we briefly introduce some of the mechanisms of plasma confinement, heating, and fueling in tokamaks, as they relate to these two devices, and some of the physics problems which will be addressed in the remainder of this report.

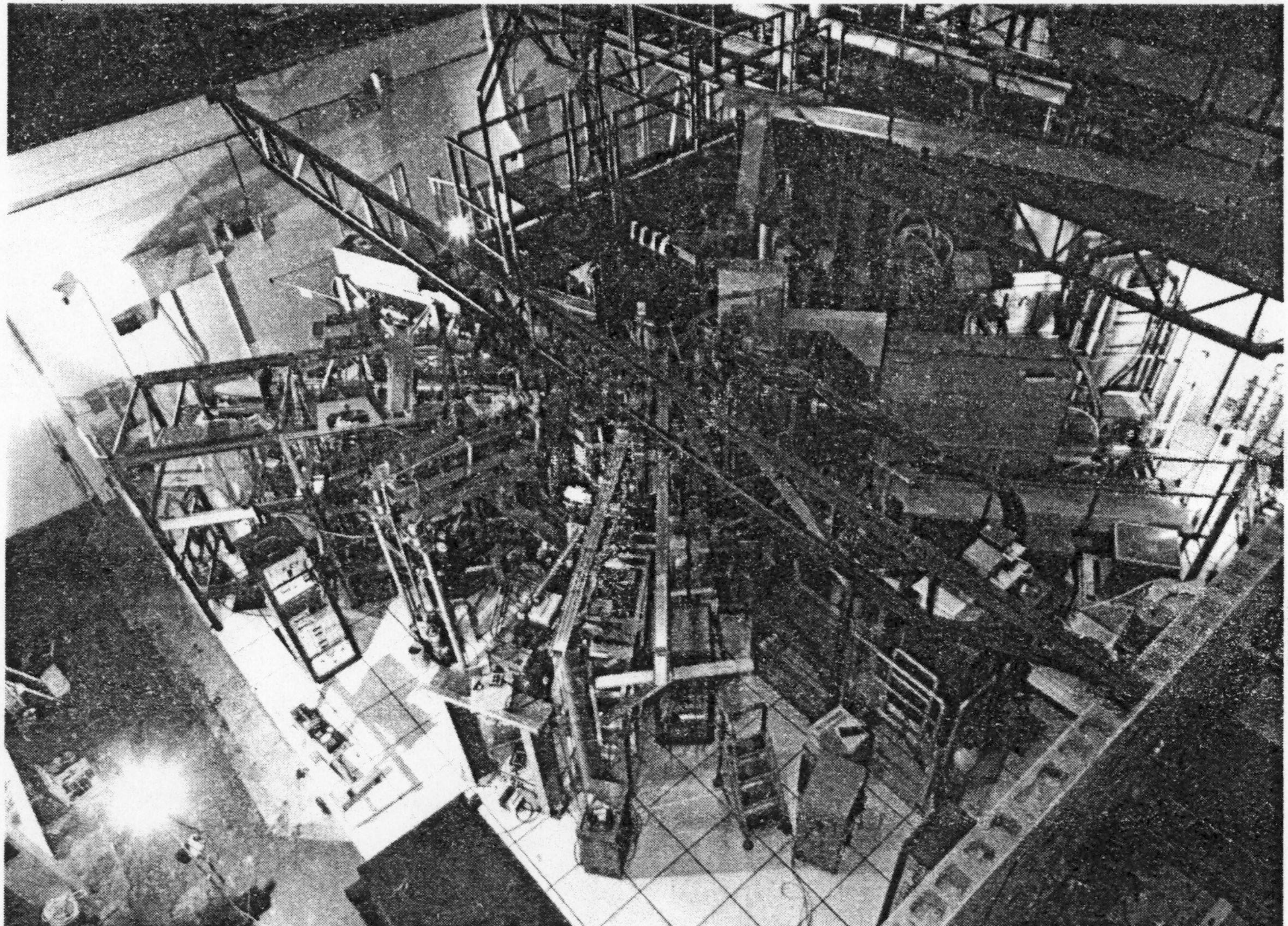

Figure 1-1. Photograph of the ISX-B tokamak.

TABLE 1-1

COMPARISON OF ISX-A AND ISX-B
PARAMETERS FOR THIS STUDY

	ISX-A	ISX-B
Size		
R_o (major plasma radius)	92 cm	92 cm
a (horizontal semi-minor axis)	26 cm	27 cm
b (vertical semi-major axis)	26 cm	49.5 cm
Plasma volume (cross section)	1.2×10^6 cm^3 (circular)	2.5×10^6 cm^3 (elliptical)
Design Features		
Wall material	304L stainless steel	304L stainless steel
Number of toroidal field coils	18	18
Performance		
Maximum magnetic field at centerline (B_o)	1.8T	1.8T
Maximum volt-seconds	0.9	0.9
Maximum plasma current, I_{max}	200 kA	200 kA
Injectors		
number	0	2
energy		40 keV
Neutral beam power into the plasma		1.0 MW
pulse duration		>100 ms
Current pulse duration	>200 ms	>200 ms

1.1 TOKAMAK CONFINEMENT

The essentials of magnetic confinement in the tokamak[1] are diagrammed in Fig. 1-2. The plasma is contained in a toroidal vacuum vessel in which a strong toroidal magnetic field B_T (of order 10 to 100 kG in contemporary devices) is produced by means of an external coil set. Thus, the tokamak is of the class of closed magnetic confinement systems, and does not share the problem of end losses found in open systems, such as mirrors. Closed magnetic field lines necessarily result in gradients in the field strength leading to particle loss by the $\mathbf{B} \times \nabla B$ drift, however, so two other field components, the poloidal (B_p) and vertical (B_V) fields, are required for plasma confinement and stability. In a tokamak, the former is realized from a current (I_p, of order 10 kA to 1 MA) induced in the plasma itself, acting as the secondary of a large air- or iron-core transformer (an iron core is indicated in Fig. 1-2), driven by sets of external, toroidal, primary windings. To overcome the tendency of the current carrying loop to expand due to the "hoop force" and to plasma pressure, a vertical field is applied, also by means of external toroidal windings.

This field configuration constitutes the basic ingredient for favorable single-particle confinement. Plasma confinement, however, is ultimately governed by collective phenomena such as stability and transport. Greatly simplified, the former limits how much plasma energy can be confined at a given toroidal field strength, and the latter determines how much power it takes to sustain a given plasma

ORNL-DWG 69-12574RA

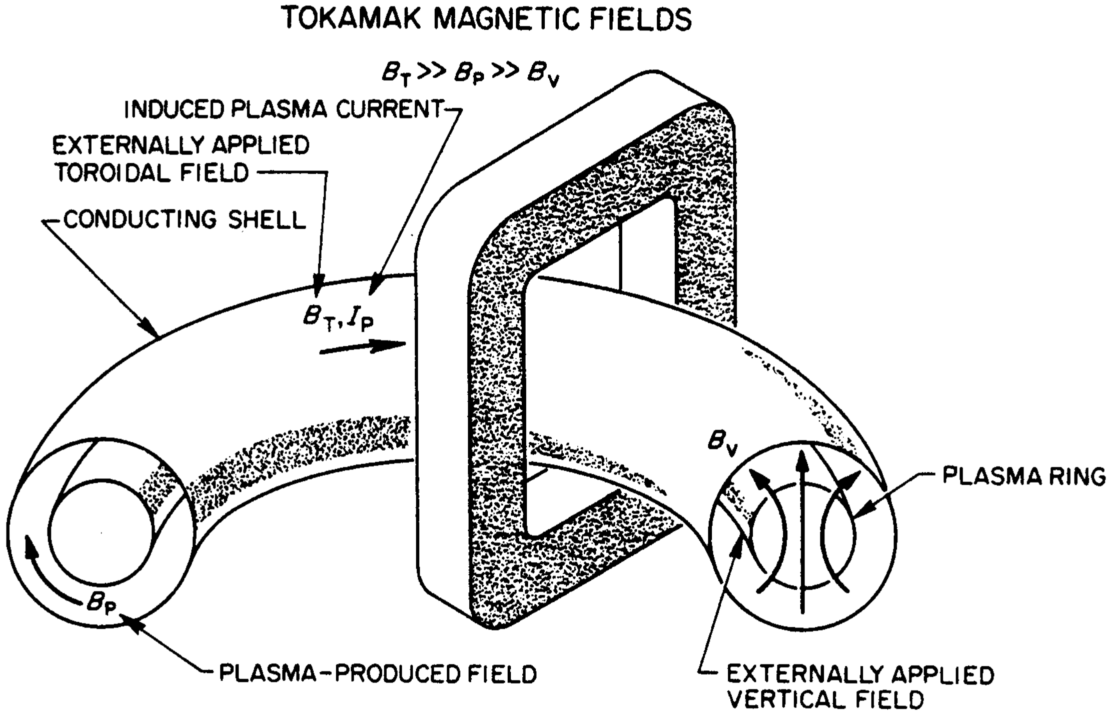

Figure 1-2. Tokamak confinement field components

energy content. Taking this point of view, it is found that transport, that is loss of particles and energy across field lines by Coulomb collisions and anomalous processes, is minimized by maximizing the plasma current. However, for given device dimensions and toroidal field, the plasma current can only be raised to the point where a stability limit is encountered; the limit, which is expressed in terms of the "safety factor" $q(a) = \frac{2\pi a^2 B_T}{\mu_o R_o I_p} > q_{min} \sim 2\text{-}4$, where R_o and a are the major and minor radii of the toroid, may be raised by increasing the toroidal magnetic field (circular plasma cross section is assumed, but the concepts can be generalized to non-circular configurations also). The figure of merit which indicates the efficiency of magnetic confinement is the plasma beta, where $\beta = \frac{p}{B^2/2\mu_o}$ is the ratio of confined plasma pressure to magnetic energy density. In view of the advantages inherent in reducing required field strength and device size while maintaining good confinement in a reactor, it is obviously desirable to try to minimize q and maximize beta. All tokamak programs address themselves to these issues to some degree. Fig. 1-3[5] indicates the empirical "Alcator scaling" of tokamak confinement time, $\tau_E \propto \bar{n}_e a^2$, where $\bar{n}_e$ is the line averaged electron density, and τ_E is the maximum gross energy confinement time for the different machines found in the published literature at the time of the survey.

Impurities also play an important role in limiting plasma confinement and in reducing the effectiveness of most heating methods. The ISX program was undertaken partly to investigate this

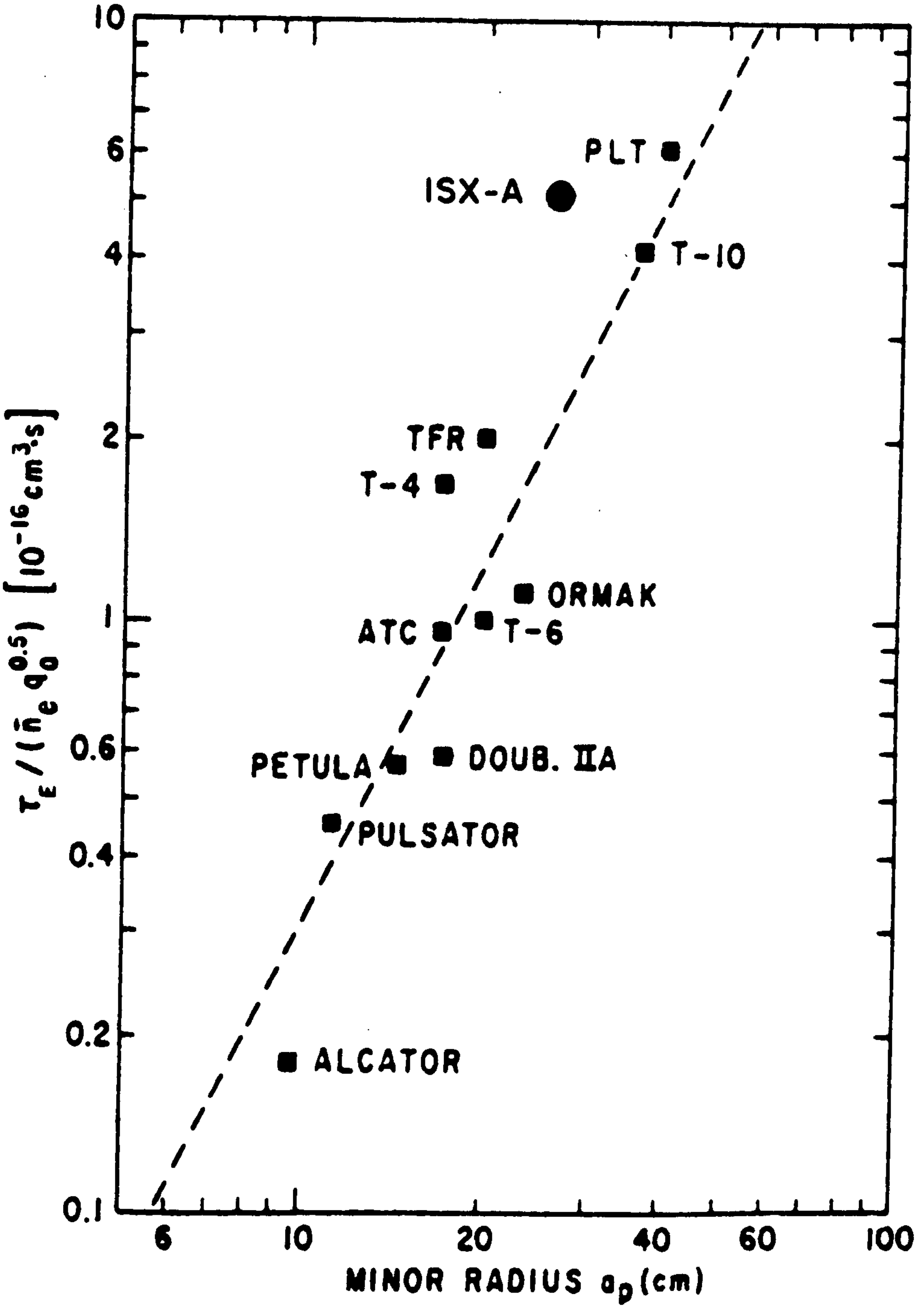

Figure 1-3. Empirical tokamak confinement scaling. (Source: Jassby, Cohn, and Parker, Nucl. Fusion 16 (1976) 1045

area. In its first phase, the ISX-A tokamak was operated with no auxiliary heating to supplement the ohmic heating provided by the plasma current alone.[6] In order to allow controlled impurity experiments and studies of plasma-wall and plasma-limiter interactions, the device was designed to minimize the exposure of the plasma to materials other than stainless steel, from which the vessel was fabricated. Because it was found in ORMAK,[7] TFR,[8] and other tokamaks that high-Z materials such as tungsten and molybdenum were particularly detrimental to confinement, these were avoided in the construction of ISX.[9] To provide the flexibility to reconfigure the experiment if necessary, ISX was built with demountable, water-cooled copper toroidal field coils. This resulted in a machine with comparatively moderate toroidal field strength (< 18 kG), but this is not such a disadvantage in light of the remarks made above.

The bulk of the experimental studies on ISX-A were carried out over a period of less than four months in 1977 and 1978. Confinement studies[10] showed that machine cleanliness could result in more favorable operating conditions, namely higher density, higher confinement time, and lower Z_{eff} than had been experienced in ORMAK, which with similar size and twice the toroidal field, had high values of Z_{eff} and tungsten limiters. One indication of the improvement in confinement is the fact that the fraction of power lost by radiation in ISX-A was 25-40%, compared with 50-80% in ORMAK. Aspects of these confinement studies will be discussed later in this report.

The results obtained from ISX-A established the viability of operating a tokamak successfully with low values of toroidal field. However, the power obtainable from ohmic heating alone is not enough to reach levels of plasma energy content sufficient to test the stability limits of the device. This fact led to the next, and current, phase of the ISX program, the ISX-B tokamak, and leads also to the general topic of plasma heating.

1.2 PLASMA HEATING IN TOKAMAKS

In the preceeding section we discussed confinement, which concerns the two Lawson parameters, density and energy confinement time. Obviously, high plasma temperature is also required for fusion, and therefore any confinement scheme must provide, or allow for, some means of heating the plasma. We alluded to the intrinsic ohmic heating obtained in a tokamak due to the toroidal current and finite resistivity of the plasma. This is insufficient to reach fusion temperatures, however, especially due to the decreasing dependence of the resistivity on temperature. In an ignited tokamak, one might expect the plasma energy to be sustained by the recaptured energy of alpha particles resulting from fusion reactions. However, some means of heating the plasma is needed for sub-ignition experimental tokamaks, and for reaching ignition temperatures in a reactor.

The most successful heating method to date, as established by experiments on ORMAK,[11] the Adiabatic Toroidal Compressor (ATC),[12] the Fontenay-aux-Roses Tokamak (TFR),[8] T-11,[13] and other devices, is neutral beam injection. In this scheme, depicted in Fig. 1-4, tens of amperes of hydrogenic ions are accelerated to energies of tens of kilo-electron-volts. These ions are neutralized in a cold gas cell and then drift a short distance into the plasma, where they penetrate, unaffected by the magnetic field, until they are ionized deep within the discharge. The resulting fast ions transfer their energy to the target plasma by classical Coulomb collisions, leading to significant heating of both the electrons and ions.[14] Early experiments were conducted at power levels representing only a perturbation on the ohmic heating power. Later experiments on ORMAK and, more recently, on the Princeton Large Torus (PLT)[15] and ISX-B, have demonstrated the viability of operating in regimes where the ion, electron, and total plasma power balances are beam-dominated; in PLT, ion temperatures in excess of 6 keV were obtained using 2.4 MW of neutral beam heating. Thus we have a successful means of externally supplying the bulk of the power to the plasma, so that we can essentially choose the current from confinement and stability considerations only. This is due in large part to the progress made in neutral beam development at ORNL,[16] Berkeley, and elsewhere.

The ISX-B tokamak incorporates two injectors with a total ultimate injected power capability of 3.0 MW. The ISX-A vacuum vessel has been replaced by one of thicker wall construction and capable of containing plasmas with vertical elongation of up to 1.9. The poloidal field system (the windings which produce the plasma current, vertical field, and additionally, radial and shaping fields)

ORNL-DWG 74-3070

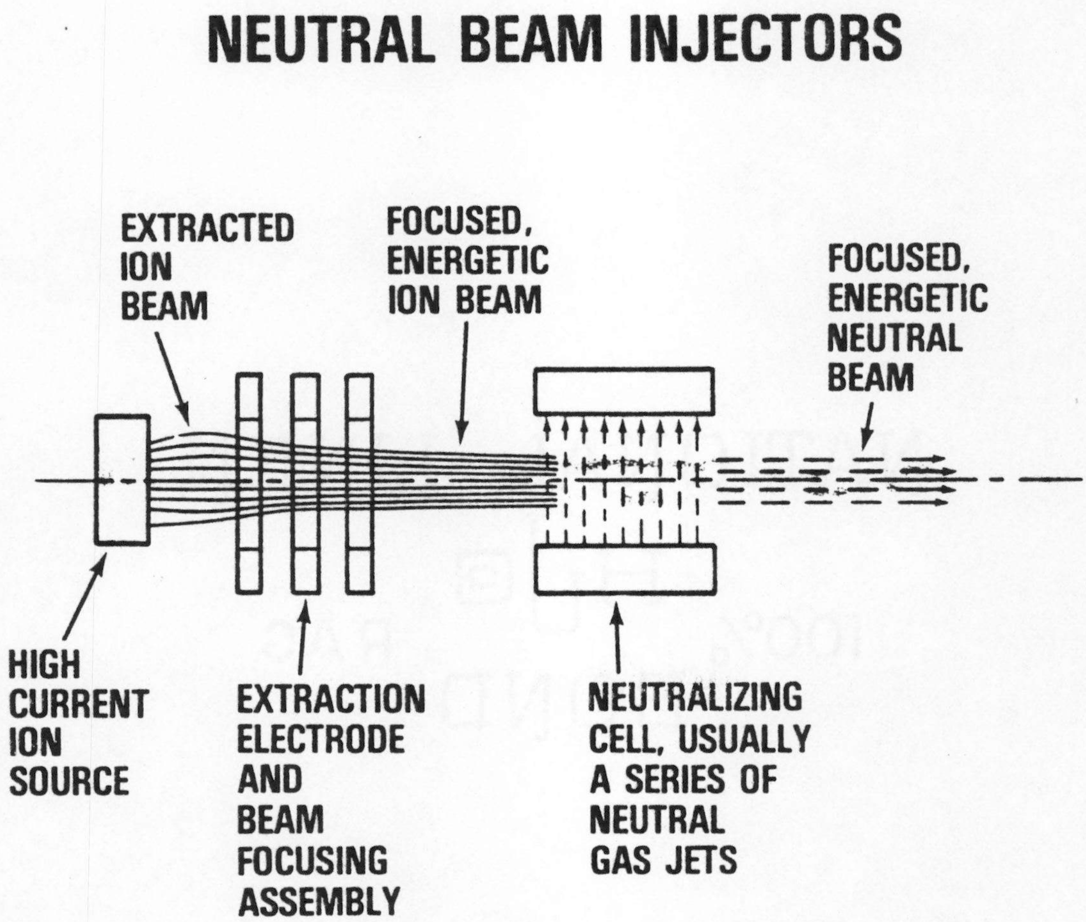

Figure 1-4. Schematic of neutral beam injector.

has also been replaced in the hope of providing shape control and faster response to excursions in plasma pressure and position.[17] Experiments to probe the stability limits in circular, elliptical, and D-shaped plasmas have begun, and some of the results are described in a later chapter. Beta limits of ~2% are predicted for circular cross sections and as high as 10% for non-circular cross sections.[4] At this writing beta values of 2% have been obtained with 1.0 MW injection into circular plasmas, but it is as yet unclear whether any real stability limits have been encountered.

Another important plasma heating method is RF heating,[18] which uses any of a wide variety of waves and modes to couple RF power from external sources, via antennas and various other structures, to the plasma. One form of RF heating that has become more promising since the advent of the gyroklystron in the U.S.S.R., and recently in the U.S., is electron cyclotron heating.[19] Encouraging results have been obtained in the Soviet Union, and an ECH program is now under way on ISX-B, also. Another promising RF method is ion cyclotron heating, which has had considerable success within the past year in major experiments on TFR[20] and PLT.

1.3 PLASMA FUELING IN TOKAMAKS

Plasma fueling is required in contemporary tokamaks in order to build densities up to desired levels and, in steady state, to balance particle losses.[21] To date, fairly simple techniques have proven adequate; the most common of these is "gas puffing" in which hydrogen gas is fed into the edge of an established plasma at a controlled rate. This method was successfully employed on the Alcator tokamak several years ago and is now in use in virtually all tokamak experiments, including ISX. However, the fueling problem will become more serious as machines with long pulse lengths and magnetic divertors begin to operate.

One advanced fueling technique which is under investigation in ISX-B utilizes frozen hydrogen pellets accelerated to high velocities ($\sim 10^5$ cm-s^{-1}) and injected into the plasma. The pellet ablates as it penetrates the plasma, and given sufficient size and velocity, has been found to fuel the interior of the discharge. In the first experiments of this type, carried out on ORMAK,[22] pellets were successfully injected, but, due to their small size (<0.21 mm dia.) and velocity ($\sim 10^4$ cm-s^{-1}), did not penetrate more than a few centimeters nor did they produce any measurable density increase. Recent experiments on ISX-A and -B, utilizing larger (≤ 1 mm dia.) and faster ($\sim 10^5$ cm-s^{-1}) pellets have had positive results, namely complete ablation and a several-fold increase in the plasma density. In the final chapter, we consider some of these studies.

1.4 TOKAMAK DIAGNOSTICS

From the preceding sections, we can identify a minimum set of parameters which must be measured, or at least inferred, in tokamak plasma physics experiments. To determine the plasma energy content requires measurements of the plasma density and of both the electron and ion temperatures. The plasma beta can then be determined, essentially, from this and the toroidal magnetic field. One can also calculate the energy confinement time if one knows the input power to the plasma. For ohmic heating, this is just the product of the plasma current and the toroidal loop voltage. The power from neutral beams can be estimated from the beam energy, the extracted ion current, and a calibration of the neutralized fraction reaching the plasma.[23] However, to gain understanding beyond mere measurements of these parameters, it is essential to also have diagnostics which investigate the various mechanisms governing stability, confinement, heating, and fueling. Such information may be obtained, for example, from hydromagnetic mode signals, radiation from impurities, hydrogenic atoms, and bremsstrahlung, and neutral and neutron emission intensities. Moreover, the high temperature plasmas produced in tokamaks are often difficult to diagnose unambiguously. Many measurements yield only volume- or chord-averaged quantities, and often the quantity of interest is obscured by other contributions to a given signal. Thus, benefits may be derived both from new diagnostics which supplement or corroborate existing measurements, and from improvements in standard techniques aimed at providing more detailed measurements or removing ambiguities.

In this report, we consider a standard diagnostic for measuring ion behavior in tokamak (and other) plasmas, charge exchange neutral analysis.[24] This technique takes advantage of a loss mechanism, namely the loss of ion energy to neutrals resulting from charge exchange reactions within the discharge. Improvements made in plasma confinement, density, and size naturally tend to reduce this loss, potentially reducing its usefulness as a diagnostic as well. Also, a serious complication arises in neutral beam heated plasmas. However, because this technique has been successful in past experience and because it does afford the most direct and detailed insight into ion behavior of any diagnostic, refinements were made to extend its applicability by overcoming these difficulties. These refinements included an improved neutral particle analyzer and more sophisticated methods for interpreting the data obtained, and have been applied in a wide range of plasma physics experiments in ISX.

1.5 OUTLINE OF THESIS

In the next chapter, we provide a more detailed treatment of charge exchange diagnostics and the problems alluded to above. An overview and summary, both of the diagnostic refinements and of the contributions to ISX plasma physics experiments which were made, are also given in Chapter 2. In Chapter 3, we present a detailed description of the design, testing, and implementation of the new analyzer, and in Chapter 4, develop the analytical tools used to interpret the data. Chapters 5, 6, and 7 contain results of experiments in ISX-A and -B in which the ion behavior was an important issue. These experiments illustrate contributions in each of the areas mentioned in this brief introduction: confinement, heating, and fueling.

CHAPTER 2

PROBLEMS AND APPLICATIONS OF CHARGE EXCHANGE ANALYSIS

Energetic neutral atoms are emitted from tokamak plasmas as a result of charge exchange reactions between plasma ions and unionized hydrogen atoms in the discharge. The resonant charge exchange reaction

$$H^o(E_1) + H^+(E_2) \rightarrow H^+(E_1) + H^o(E_2) \qquad 2.1$$

represents an energy loss on the average since the reactant ion has energy E_2 generally greater than the neutral's energy E_1 and, once neutralized, is also more likely to escape than the less energetic neutral. Assuming the resulting neutral to be unconfined, a net amount $E_2 - E_1$ of plasma energy is lost in the exchange. While this process is undesirable from the standpoint of plasma confinement, we are able to take advantage of it for diagnostic purposes; the energetic charge exchange neutrals produced represent, in a known way, the ions in the plasma.[24,25] By detecting and energy analyzing the neutrals, one can infer rather directly the ion distribution function and hence the ion temperature.

---

*For convenience, we shall use the abbreviation "CX" to refer to the charge exchange neutral diagnostic, and "charge exchange" to refer to the loss process or where needed for clarity.

In this chapter we review both the advantages and limitations of charge exchange (CX) analysis as a plasma diagnostic.* One of the objectives of this research was to develop means of overcoming some of the limitations, thereby extending the usefulness of CX diagnostics. This led to more detailed and sophisticated data analysis techniques based on those used on ORMAK[26] and PULSATOR[27], and led also to a neutral analyzer of improved capabilities also based on previously employed methods.[28] We summarize these and the tokamak physics issues which were addressed experimentally on ISX. This will give the reader an overview of the major topics to be covered in more detail in succeeding chapters.

2.1 ADVANTAGES OF CHARGE EXCHANGE DIAGNOSTICS

The principal advantage of the CX diagnostic technique is that it affords an almost direct measurement of the plasma ion distribution, from which ion behavior, the ion temperature in particular, can be determined. Since little energy or momentum are exchanged in the charge transfer and since the resonant hydrogen charge exchange cross sections are well known,[24,29] it is legitimate to interpret the detected neutral flux in terms of plasma ion behavior. Other ion diagnostics are less direct, as they depend on the neutrons resulting from DD fusion reactions,[24] on Doppler-shifted photons from radiating impurity ions,[15] or, in a still-unperfected technique, on far infrared photons scattered by the Debye shielding clouds surrounding the ions.[30] Usually the fluxes of escaping neutrals are adequate (10^7 to 10^{13} cm^{-2}-s^{-1}-eV^{-1}-s^{-1}) to make measurements on a time scale (2-10 ms) shorter than those of most tokamak experiments (e.g. $\tau_E \cong$ 10-30 ms, $t_{exp} \cong$ 150-250 ms), such that an effectively continuous measurement may be made.[31]

Since a measure of the ion distribution function itself is obtained, non-thermal effects, such as those associated with neutral beam heating, can be directly observed and used to assess the validity of any ion temperature determination. Other measurements, particularly absolute neutron flux detection, must presuppose a Maxwellian distribution in relating the data to an ion temperature. Finally, basic charge exchange measurements are non-perturbative and may be made with relatively simple apparatus; the escaping neutrals are re-ionized in a cold gas cell, analyzed using an ion spectrometer employing electric and/or magnetic fields, and detected by means of detectors such as channel electron multipliers. Since the technique is basically one which takes advantage of an extant loss mechanism, it desirable to make use of it, both to infer the magnitude of the loss itself and for the diagnostic information which is available as well.

2.2 PROBLEMS OF CHARGE EXCHANGE DIAGNOSTICS

For the reasons given in the preceding section, charge exchange neutral detection and analysis has become the principal ion diagnostic for tokamak experiments. However, as these devices extend their parameters into regimes of higher density and temperature, some difficulties in making charge exchange measurements are encountered. Two of these problem areas were addressed in this work; the problems, and the possible and chosen solutions to them, are explained in this section.

The first is specific to neutral beam-heated plasmas, in which the slowing-down beam ions produce a non-thermal, anisotropic ion distribution.[32] The bulk plasma ions may still be Maxwellian, however, and it is necessary to measure their temperature, and desirable to determine the fast ion distribution as well, in order to evaluate the effectiveness of neutral beam ion heating. The diagnostic problem, in this case, is to resolve the two ion populations. The second problem is that of measuring the core of plasmas which, by virtue of their size and density, are "thick" to neutral particles, leading to exclusion of incoming target neutrals and attenuation of outgoing charge exchange neutrals.

2.2.1 CX Spectral Distortion by Injection Fast Ions

In many tokamak plasma experiments, two or more distinct classes of ions exist. For example, in pellet fueling, the target ions and pellet-injected ions may be distinguished. Another important case, already mentioned, is that of neutral beam heated plasmas, in which one can distinguish the thermal and fast ion populations. An example of the diagnostic problem presented by this mixed distribution is given in Fig. 2-1, which depicts a charge exchange neutral spectrum measured perpendicular to the toroidal magnetic field on ORMAK under moderate neutral beam heating. The tail of the thermal distribution is obscured by the perpendicular fast ion spectrum.

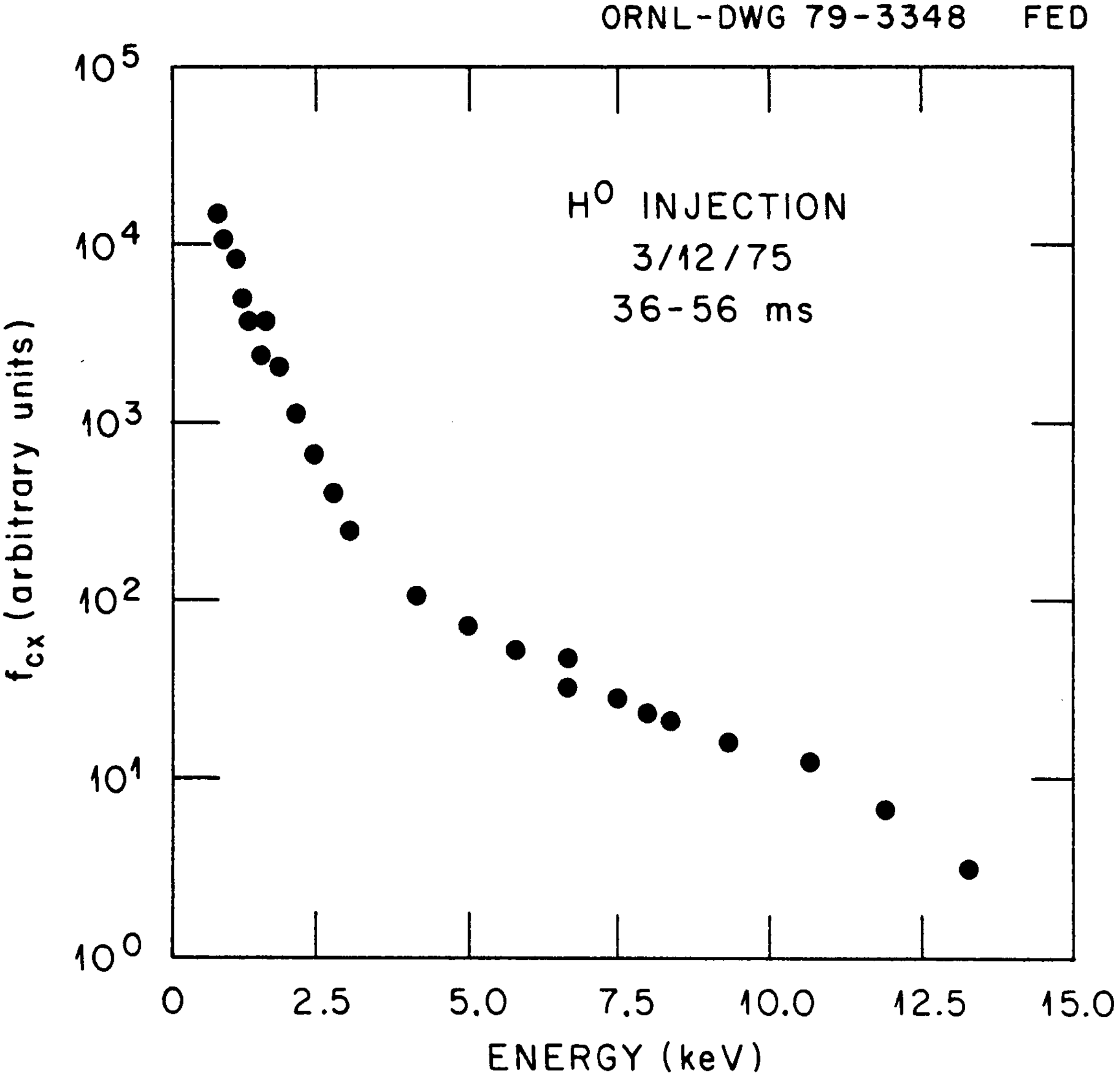

Figure 2-1. Perpendicular charge exchange spectrum measured on ORMAK. An electrostatic analyzer was used; hydrogen beams were injected into a into hydrogen plasma so the thermal and fast ion components are both seen in the spectrum.

The most successful means of solving this problem is to mass identify the bulk and beam ions by, for example, injecting a hydrogen neutral beam into a deuterium plasma.[13] One then uses a spectrometer incorporating both magnetic and electric fields, in one of several possible configurations, to analyze neutrals by both mass and energy and thereby permit measurements of both ion distributions.

An analyzer with this feature was developed, built, and calibrated for use on ISX.[31] It is capable of detecting and analyzing neutrals in seven energy channels simultaneously, spanning an energy range of about 11 to 1. By changing field settings between tokamak discharges, one can build up charge exchange spectra for hydrogen and deuterium at energies ranging from about 0.5 to 50 keV. The instrument itself will be described in greater detail in the following chapter.

2.2.2 Plasma Thickness and Profile Effects

In typical viewing geometries for tokamak CX diagnostics the viewed neutrals are those which originate near a chord through the plasma and whose velocities are directed toward the analyzer entrance aperture, within some small solid angle. At best, then, only a chord-integrated measurement is obtained. Worse, the local birth rate of charge exchange neutrals is proportional to the product of the ion and neutral atom densities, and typical profiles are such that, while the ion density and temperature tend to peak near the center, the neutral density is maximum at the edge and two to four orders of magnitude less at the center. This is due to the fact that the primary neutral sources in most tokamak discharges, namely cold gas fed externally and gas evolved from surfaces such as vessel walls and limiters are, obviously, outside the plasma. A small fraction of these neutrals are able to cascade into the plasma core, but this fraction decreases, roughly exponentially, with plasma density. The result is that, while it is the plasma core which is of greatest interest, measured charge exchange spectra are strongly dominated by contributions from the outer layers. As this difficulty worsens with increasing density and machine size, it potentially limits the usefulness of CX as a diagnostic technique.[25]

One method of overcoming the difficulty is simply to emphasize the asymptotic tail, i.e. $E \gg T_i(0)$, in analyzing the emitted neutral spectrum. Ions of such high energy must originate predominately in the hottest regions of the plasma, despite the relative scarcity of target neutrals there. Consequently, the neutral distribution, corrected for energy-dependent production rates and detection efficiencies, is expected to approximate that of the central ion distribution, namely a Maxwellian, and this is, in fact, often observed to be the case. There are disadvantages, however, in relying exclusively on the suprathermal tail for ion temperature measurements. Obviously, the signal strength will be relatively weak at such energies, making it more difficult to obtain useful data. More importantly, there is uncertainty as to how well the suprathermal ions represent the bulk plasma. For an ideal Maxwellian distribution there is no difficulty; but distortions of the thermal ion tail are not uncommon, as they are often observed in both RF- and neutral beam- heated plasmas. In such cases, temperatures inferred from the slope of the asymptotic spectrum may differ from values which are representative of the bulk.

A second method employs a diagnostic neutral "doping" beam to locally enhance the production of charge exchange neutrals (energy E) at a point along the viewing chord by an amount approximately equal to $n_b \sigma_{cx}(E_b) E_b^{1/2} / n_o \sigma_{cx}(E) E^{1/2}$, where n_b and E_b are the beam density and energy, n_o the naturally occuring neutral density, and σ_{cx} the charge exchange cross section.[25] By modulating such a beam during a tokamak discharge it is possible to isolate the beam-induced contribution to the detected flux which, in turn, originates from the small volume defined by the intersection of the beam trajectory and the viewing chord. This is an extremely attractive technique, because it gives a definitive local measurement of the ion distribution itself, requiring a minimum of assumptions to interpret the data. The drawback, of course, is that even the simplest neutral beam system is rather complicated and expensive to build and operate. Moreover, in common with passive charge exchange measurements, one is still faced with the problem of transmitting the "target" neutrals to the center of dense plasmas. This difficulty is alleviated considerably by having a collimated, energetic source, but not completely overcome; at high density, most of the beam may be attenuated by the time it reaches the center and so very intense neutral beams are required to produce significant flux enhancement.

Despite such problems, a diagnostic beam is the most satisfactory means of achieving a spatially resolved neutral diagnostic, has been used on PLT and other machines, and will soon be incorporated on ISX-B as well.

In the absence of a diagnostic beam, one must make available passive measurements suffice. In doing so, it is possible to take advantage of information available from other diagnostics and known plasma behavior, specifically, measured density and density profiles and neutral particle transport mechanisms. With this in hand, one can calculate the expected charge exchange flux consistent with a given central ion distribution and local neutral density. The calculated flux is then compared with data and the central ion temperature and ion temperature profile are iteratively corrected to produce a best fit between the measured and calculated spectrum.[26] This emission modeling procedure is the one adopted in the present work to infer ion temperatures in the ISX tokamak at densities up 7 × 10^{13} cm^{-3}, line averaged. It will be described in detail in Chapter 4, but we mention here how the major uncertainties in this method were addressed.

Since the local charge exchange reaction rate is proportional to the neutral density, for which no independent measurements exist, we must rely on neutral transport codes to at least calculate its radial dependence. Existing one-dimensional codes are primarily used for this purpose; however, there is evidence for strong toroidal asymmetries in the neutral density, which these models do not consider. To assess the effects, on both the charge exchange measurements and plasma losses, of localized neutral sources such as gas valves, limiters, and neutral beams, a cylindrical, two-dimensional, Monte Carlo neutral density code was developed. As a result of this calculation, the consistency between the absolute measurements of neutral density and the values inferred from power balance calculations was improved.

Only single chord CX measurements have been possible to date on ISX, so no experimental ion temperature profile information is obtained. Therefore, it is necessary to invoke a profile shape factor by assumption, and we thus arrive at results which are consistent with the assumed shape. The profile sensitivity can then be checked by trying different shapes, and this gives an indication of the uncertainty in the obtained result.

2.3 ION CONFINEMENT, HEATING, AND FUELING EXPERIMENTS ON ISX

The present mass-energy neutral analyzer was first used on ISX-A in December, 1977. Since that time it has been the primary ion temperature diagnostic for all experiments performed on ISX-A and ISX-B. The modeling analysis procedure has been incorporated as well. The results obtained have contributed in a major way to many of the plasma physics studies undertaken in the program. In Chapters 5, 6, and 7 we present results in three such areas, where the CX measurements were of particular importance to the interpretation of the experiments. We summarize them in this section.

2.3.1 Ion Confinement Studies in ISX-A

Ion confinement has been studied both in ohmic- and beam-heated plasmas in ISX. Because the device is characterized, for its size, by low toroidal field, and hence low plasma current, it addresses the problems of confinement in high beta tokamaks. Moreover, it is a relatively clean device, and an empirical consequence of this is the ability to operate over a wide range of plasma parameters, especially density.

A unique feature of experiments in ISX-A, in which the density was varied while keeping plasma current and toroidal field constant, is the fact that the ion temperature was observed to peak at an intermediate value of density, rather than increasing monotonically as had been observed in ORMAK and other tokamaks.[10] Power balance calculations which use the measured density and electron temperature, classical electron-ion power transfer, and a neoclassical ion heat conduction model give the same ion temperature values as were measured. This agreement provides solid evidence for neoclassical ion confinement in tokamaks. The decrease in ion temperature with increasing density is explained in terms of the increasing role of ion losses in the power balance and signifies a transition between electron loss- and ion loss-dominated plasma energy confinement. The important consequence of this is a corresponding peaking of the bulk energy confinement time with density, reflecting the ion behavior. The conclusion, at least for ohmically heated tokamaks, is that the so called "Alcator scaling", $\tau_E \propto \bar{n}_e$, is invalid in the high density, low current regime, where plasma energy is lost predominantly through the ion channel.*

2.3.2 Neutral Beam Heating and High Beta Studies in ISX-B

One of the main goals of the ISX-B program is the experimental determination of beta limits in tokamak plasmas.[4] To accomplish this, two 40 keV neutral beam injectors are used to heat a plasma of moderate size ($a = 27$ cm, $R_0 = 93$ cm) confined at low toroidal magnetic field ($B_0 < 1.8$ T). The intrinsic ohmic heating power of this device is only 100-200 kW, while the two beams are ultimately capable of up to 3 MW. To date, up to 1.0 MW of injected neutral beam power has been used; at these levels, the plasma power balance is clearly beam-dominated, and there is some evidence for strong influence on the particle balance as well. The consequence is a rather sizable fast ion population in the plasma and mass-resolved charge exchange diagnostics are essential to study the ion behavior. Therefore, in most experiments, hydrogen beams and deuterium plasmas have been used.

In beam-dominated plasmas in ISX-B, ion temperature variations with both beam power and density have been investigated by the author. In the power balance calculations for these studies, experimentally measured densities and electron temperatures are again

*The ion temperature measurements were made by the author and corraborated by neutron flux measurements made by J. T. Mihalczo. The general conclusions were based upon data and calculations provided by many members of the ISX Group.

used*. Beam power contributions to both ions and electrons are calculated using any of a number of codes which model the classical beam trapping and slowing-down processes. At high densities, neoclassical heat conduction again gives good agreement with the data. At lower densities, the ion power balance is presumed to be strongly influenced by charge exchange losses. These are not measured with sufficient accuracy by the CX analyzer, evidently due to the existence of toroidal asymmetries in the neutral density, to conclusively specify the heat conduction coefficient. These measured neutral densities are at least an order of magnitude lower than those determined by simply invoking neoclassical confinement in the power balance calculations. However, the CX analyzer is far enough away from gas sources in the machine that the local neutral density it measures is likely to be much less than the toroidally averaged value seen by the plasma and fast ions. The two dimensional neutrals code calculations bear this out, showing that most of the neutrals are localized around their sources. Thus, it seems probable that neoclassical ion confinement is applicable in this low density regime, as well.

---

*Provided by the ISX Thomson Scattering Group and others.

Aside from ion temperature measurements, other beam-related phenomena have been observed. At low plasma densities, a non-Maxwellian tail on the thermal spectrum is seen. Because of the mass identification, it is clear that the tail is not composed of fast ions themselves, but of bulk ions which are excited to suprathermal energies by some interaction with the beam. Also, we have made detailed measurements of the perpendicular fast ion neutral spectrum itself. The temporal evolution of the three beam components, at full-, half-, and one-third injection energy, are clearly identifiable. Better insight on the fast ion population, however, may be gained with a tangential analyzer. At this writing the present analyzer has been re-oriented in order to make such measurements.

2.3.3 Hydrogen Pellet Fueling Studies in ISX-B

In pellet fueling experiments on ISX-B, solid hydrogen pellets are ablated in deuterium plasmas heated either ohmically or by hydrogen neutral beams. In the former case, the pellet ions which are deposited in the plasma are mass-distinguishable from the background ions and can be clearly observed. This result clearly demonstrates the fueling effect of these pellets. In the injected case, three ion classes are present: beam, bulk, and pellet. Measurements of the hydrogen neutral spectrum at both fast ion and thermal energies indicate a strong interaction between beam and pellet; evidently there is either a rapid loss or slowing down of fast ions by the pellet which leads to faster or more complete ablation of the pellet, compared to ohmic heating cases.

CHAPTER 3

MASS-ENERGY NEUTRAL ANALYZER

In order to solve the problem of making mixed ion measurements in ISX, a mass-energy neutral spectrometer was designed, fabricated, and tested by the author. We describe it in this chapter; however, before doing so, we review some of the criteria applied in designing such diagnostics for tokamak plasmas.

3.1 DIAGNOSTIC DESIGN CRITERIA

3.1.1 Ion Mass and Energy Selection Techniques

Given a collimated beam of singly charged positive ions, as are stripped CX neutrals streaming from the stripping cell, there are several means of determining its mass-energy composition.[24] Each ion is completely characterized, for this purpose, by any two of its mass, velocity, momentum, and energy, so two selectors are needed to perform the required analysis. Three selection schemes which have been used are represented in nomographic form in Fig. 3-1. Direct mass selection may be accomplished by means of a linear RF quadrupole analyzer but this is inconvenient for light ions of tokamak energies because long lengths, high RF frequencies, and precise control of field strengths and mechanical dimensions are required.[33] Time-of-flight analysis is a possible means of velocity selection,

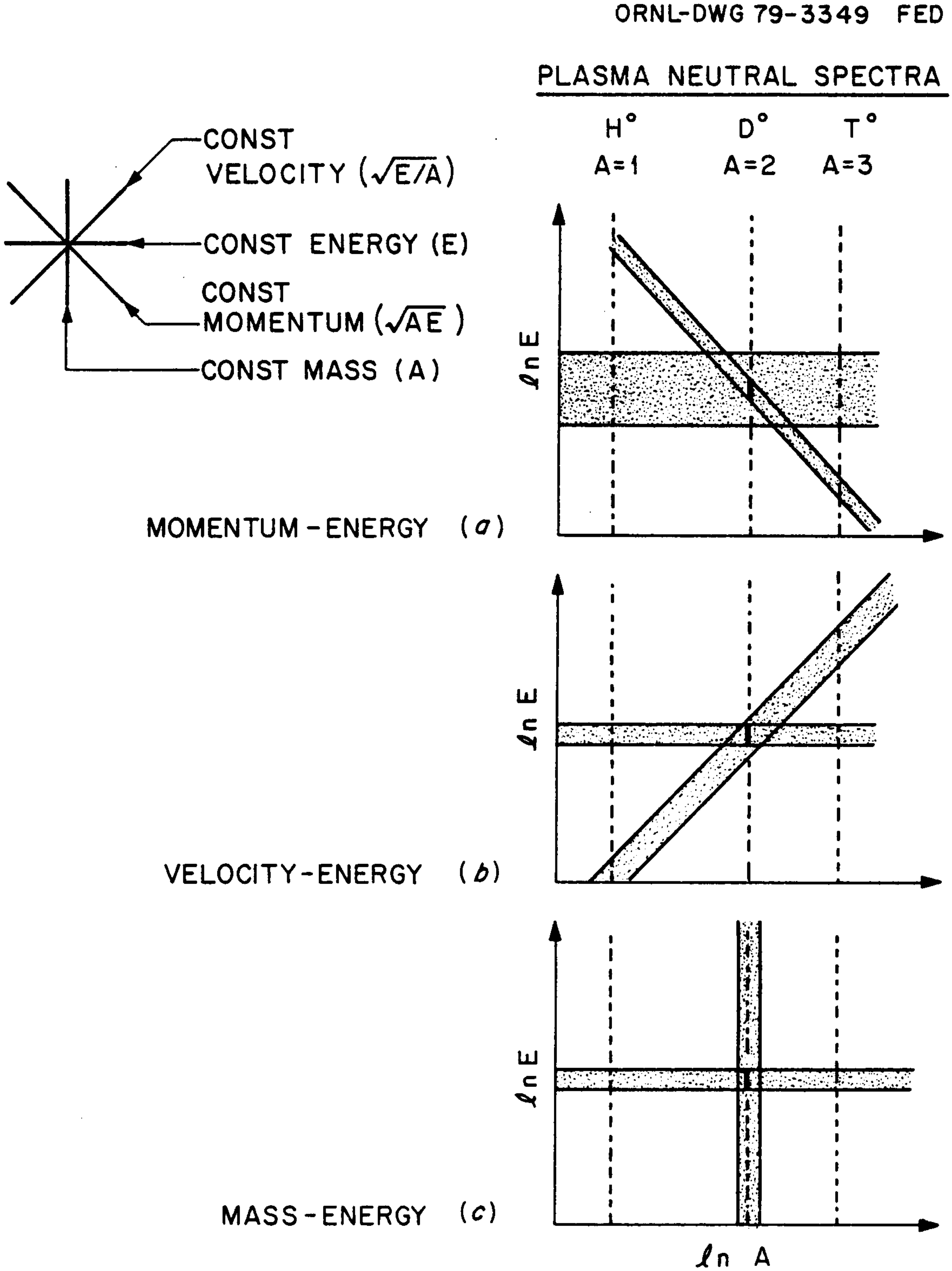

Figure 3-1. Nomograph illustrating different mass-energy selection techniques. Examples in which one selector is an energy analyzer and the other a momentum (a), velocity (b), or direct mass (c) selector are shown. One selection band must be narrow enough to obtain the desired energy resolution; the other need only distinguish between widely-spaced mass species.

widely used in nuclear physics research, but for tokamaks, it too requires long flight paths. Furthermore, it must be combined with a second selector, of energy or momentum, which complicates the basic technique to the point of impracticability.

The simplest methods for this purpose are those which employ electro- and magnetostatic fields. For a beam of singly charged ions of given initial direction, the trajectories depend on the ratios of ion energy to electric field, and ion momentum to magnetic field. Thus, a purely electrostatic field acts as an energy analyzer and a purely magnetostatic field, as a momentum analyzer. The approach taken by the author,[31] as well as other workers,[28,34-37] employs a uniform magnetic field to spread the beam out according to momentum. An array of several apertures defines beamlets, each of prescribed momentum, which are mass analyzed, in effect, by passing them through electrostatic energy filters. This produces a multi-channel, steady-state instrument based on simple and predictable field configurations. It tends, however, to be large and relatively massive because it requires a large iron electromagnet, and this is the principal drawback of this approach. Furthermore, it precludes the possibility of varying the selected energy band during a discharge.

Another technique, presently under investigation at ORNL, is based on a velocity filter, which uses crossed, spatially uniform, electric and magnetic fields to remove from the beam all ions but those with velocities near $\frac{\underset{\sim}{E} \times \underset{\sim}{B}}{B^2}$.[38] Subsequent electrostatic energy analysis is then used to separate the mass species; however only one beamlet for each mass is obtainable in this way. To produce a spectrum, it is necessary to vary the selected velocity and energy so that different energy points are obtained in successive time intervals, instead of simultaneously. This requires about 10-20 ms to obtain 5-10 energies, and the velocity and energy analyzer fields must track, in a non-linear manner, with about 1-2% accuracy. This approach, if successful, is attractive because of a possible savings in size and weight over the momentum analyzer. It has been applied with good results to ORNL's Elmo Bumpy Torus (EBT), a steady-state device.[39]

3.1.2 Mass Analysis

The purpose of the diagnostic is to study the behavior of the hydrogenic ions in the plasma; for all cases of interest in ISX, these are hydrogen and deuterium (and, in the case of a DT reacting facility such as TFTR, tritium). Because these isotopes have a large relative mass separation (2:1), realization of the required mass resolution requirement should not be difficult. In typical experiments, such as those in which H^o beams are injected into a D^+ plasma, the crucial parameter is the rejection ratio, defined as the detected fraction of the rejected species. The tail of the thermal distribution may easily be overwhelmed, by at least an order of magnitude, by the fast ion spectrum. In order to make asymptotic measurements of the thermal spectrum, in the presence of injection, mass rejection of 50-100 to 1 is a reasonable objective.

It is tempting to consider the possibility of detecting impurity neutrals, such as carbon, nitrogen and oxygen. However, the ion densities of these elements are extremely small compared to that of hydrogen and, being multiply charged at detectable energies, their neutral production is negligible. Thus, there is little to be gained in considering mass numbers greater than A = 3 or 4 in the design.

3.1.3 Energy Analysis

The greatest ion energy expected in beam heated tokamaks is that of the primary beam component, plus a few per cent. In ISX-B, this energy is nominally 40 keV, so a design goal of 50 keV was used.

For neutral particle analyzers, the low energy limit is fixed by the characteristics of the stripping medium. For detailed study of the edge neutrals, energies as low as 50 eV or less would be of interest. Cesium vapor stripping cells have been used (e.g. on the EBT experiment[40]) at such energies. However, the more traditional cold gas cells using N_2, H_2, or He have the advantages of simplicity and better stripping at the more important energies above a few kilovolts, even though scattering and reduced efficiency effectively prohibit their use below about 300 eV.[41] In ISX, central ion temperatures less than 200 eV are of little interest and are rarely seen. Furthermore, every effort must be made to avoid potential plasma contaminants from diagnostics. For these reasons, H_2 and D_2 were chosen as stripping gases, despite the fact that N_2 has higher stripping efficiency.[41] It will be seen that efficiencies of the order of approximately 1-10% are obtained with H_2 over most energies of interest.

With few exceptions (for example, a tangential fast ion spectrum) tokamak CX spectra are devoid of fine structure, so extremely high energy resolution is unnecessary. Signal strength is a more serious concern, however, due to the scarcity of neutrals in the plasma core. From this consideration, as wide an energy window as possible would be desirable. However, the window ought to be narrower than the e-folding width of the spectrum, namely the ion temperature, so we require that $\delta E \ll T_i$. Since we wish to inspect the asymptotic tail of the spectrum to improve the spatial localization of the measurement, the resolution requirement becomes

$$\frac{\delta E}{E} < \frac{T_i}{E} = \left(\frac{E}{T_i}\right)^{-1}_{max} \cong 0.1 \qquad 3.1$$

Given the need to detect as far as $10 \times T_i$ out on the tail, a choice of 5% FWHM was made for the present analyzer.

3.1.4 Spectral Coverage

Tokamak discharges in ISX last about 200 ms, with at least 2.5 min. between shots. Thus, as is the case in all tokamak systems, effective use of each discharge must be made. Consequently, one goal in designing a CX analyzer is to be able to make an ion temperature determination, which requires several spectral points, in a single shot. For this instrument a seven channel design was used; five to ten channels are typical. No energy scanning is employed during a discharge; however settings may be changed from shot to shot to build up a more detailed or extensive spectrum, given adequate discharge reproducibility. Data from a single shot can give a reasonable ion temperature measurement for routine operation, but usually at least three similar shots are needed to ensure reliability or to usefully employ some of the more sophisticated analysis techniques.

3.1.5 Reliability

In designing a particle spectrometer for a tokamak diagnostic, it is important to anticipate the adverse aspects of the operating environment. Several of these are the presence of stray magnetic fields, the pulsed nature of the experiment, and the difficulty with which an analyzer can be re-calibrated. We review the relevant considerations in this section.

Error deflections of stripped particles due to stray fields are proportional both to the stray field strength and to the length of the charged particle's trajectory. In order to minimize the importance of these effects, the trajectories should be kept as short as possible, with most of their length in the analyzer fields. External fields may be excluded by means of magnetic shielding, which, in the case of magnetic analyzers, can be conveniently provided by the magnetic circuit. Internal stray fields (e.g. fringing fields of the gap between magnetic pole faces) can have focusing properties which may, in principle, be utilized. These properties were investigated by the author and are discussed in Appendix A; it was found that the difference between a focusing and a defocusing configuration was often slight and focal lengths typically long compared to magnet dimensions. Thus it would require accurate tailoring of these fields to obtain the desired focussing, which in turn would entail needless complexity and size in the design.

Lead shielding may be incorporated to reduce or eliminate hard x-ray contamination of the signal. For maximum effectiveness, the lead should surround the detectors as completely as possible, since hard x-ray "sky shine" can lead to photons incident from all angles. To minimize weight, the lead should be close to the detectors. In the present device a five-sided, 1.9 cm thick lead box was built around the detector array.

The fact that a tokamak shot is a transient phenomenon precludes the opportunity of manually optimizing the analyzer field settings. In the mass-energy analyzer, selection of the desired particles is accomplished by overlapping momentum and energy pass bands, corresponding to Fig. 3-1a. If one of the pass bands is too narrow, small errors in the field settings will cause the bands to overlap on a non-integer ion mass number, resulting in no detected particles. In a steady state experiment, one could easily fine-tune to recover the peak, but this is not practical in tokamak operation. To avoid this difficulty, we take advantage of the large relative mass spacing between the ions of interest, which implies that we can make one of the selection bands relatively wide (20-40%) and still obtain the necessary mass rejection. An error of a few per cent in the other (narrow band) field produces at worst a like error in the inferred energy of the detected particles, but such errors can easily be kept within tolerable limits.

Calibrating a neutral spectrometer involves installing it on a special neutral beam facility and, usually, removing it from service for several weeks. Obviously, it is not practical to do this at very frequent intervals, given the schedule requirements of typical tokamak experimental programs. An in situ ion source can be easily fabricated and used to test all of the analyzer properties except its stripping efficiency.[42] A monoenergetic thermal-emission lithium ion source is used to re-check analyzer field settings periodically and to test detectors for, for example, counting losses and channel to channel variations. Because ^6Li and ^7Li both occur in significant natural abundance (about 6% and 93%, respectively), the mass selection characteristics may be tested with this source as well. A diagram of the source and its power supply configuration appears in Fig 3-2, and details of its behavior are given in reference (42).

3.2 ANALYZER DESCRIPTION

The analyzer designed and built for use on ISX* is shown in Fig.

---

*A specific acknowledgement is due Dr. J. P. Girard of the Service du Confinement des Plasmas, Centre d'Etudes Nucleaires, Fontenay-aux-Roses, France, who developed an instrument upon which the author's design was based. The very detailed information provided by Dr. Girard was an invaluable starting point for the present work.

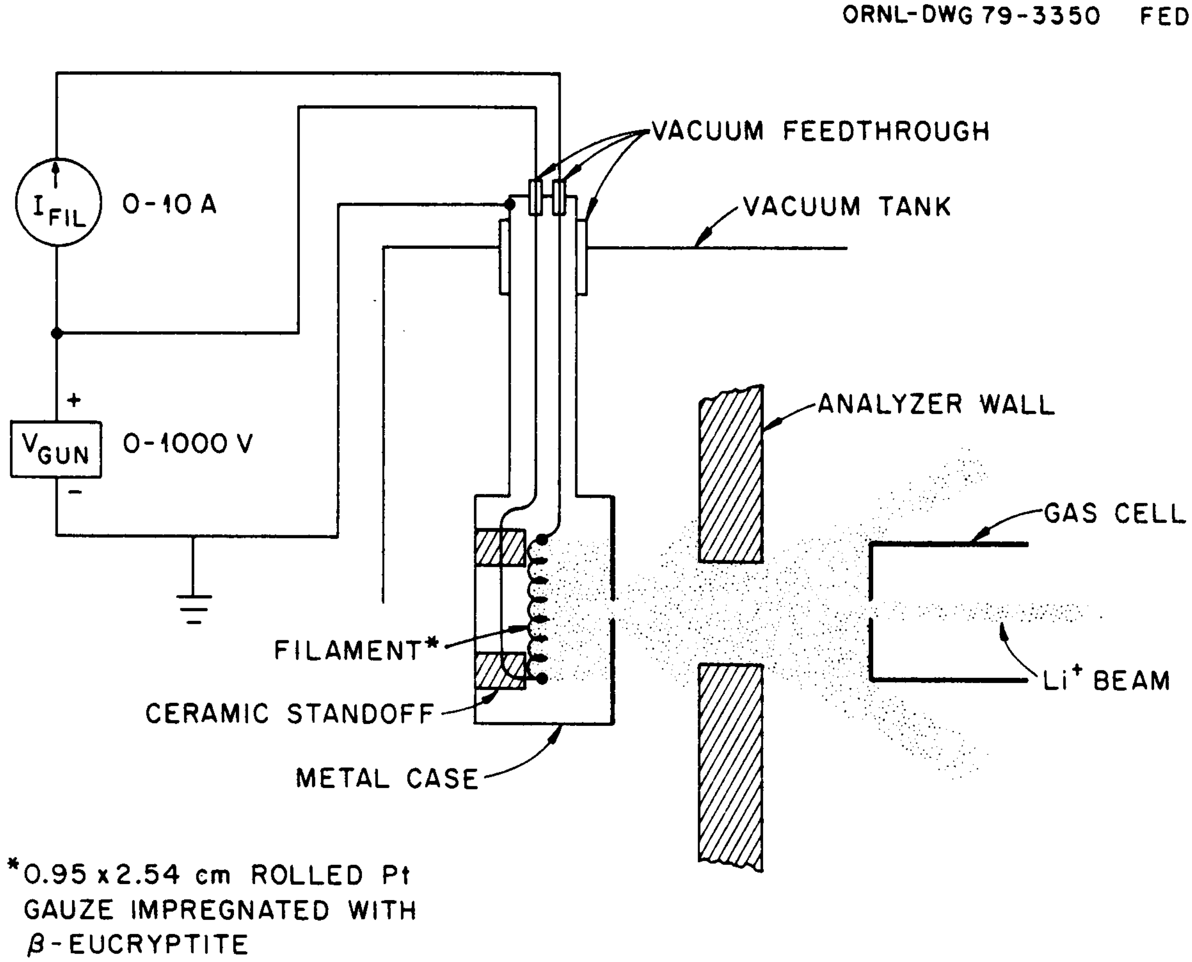

Figure 3-2. Thermal lithium source used to produce test beam of monoenergetic ions.

3-3. It consists of a 5.1 cm long gas stripping cell followed by a seven-slit 180 degree magnetic momentum analyzer. The slits define momentum beamlets which are in general bienergetic, assuming both D and H are present. The desired species is selected by the low resolution, cylindrical plate, electrostatic energy filters. The ions are detected in detector modules containing channel electron multipliers (channeltrons) operated in an event counting mode.[43] Dimensions and other details of a typical channel are given in Fig. 3-4 and the accompanying Table 3-1. The analyzer is contained in a 1.9 cm thick iron box which acts both as the flux return yoke for the magnet and as a magnetic shield which excludes fringing fields of the tokamak. The outer dimensions of the box are approximately 38x38x23 cm, and the weight is approximately 150 kg. A photograph of the instrument, partially assembled, is shown in Fig. 3-5.

In its present configuration, the iron box is not vacuum tight, but is enclosed in an external vacuum jacket which is pumped by means of a 500 ℓ/s turbomolecular vacuum pump. The stripping gas (H_2 or D_2) is fed into the gas cell by a controlled leak. The cell pressure has been inferred indirectly from the pressure in the external tank, based on a one-time measurement of the flow rate; recently, however, a capacitance manometer has been incorporated to measure the gas cell pressure (about 8-10 torr) directly, and this has proven more satisfactory. Because of hysteresis in the magnetic circuit, it is necessary to measure the gap field itself, rather than relying on the magnet current. This is accomplished with an in situ Hall probe[44]

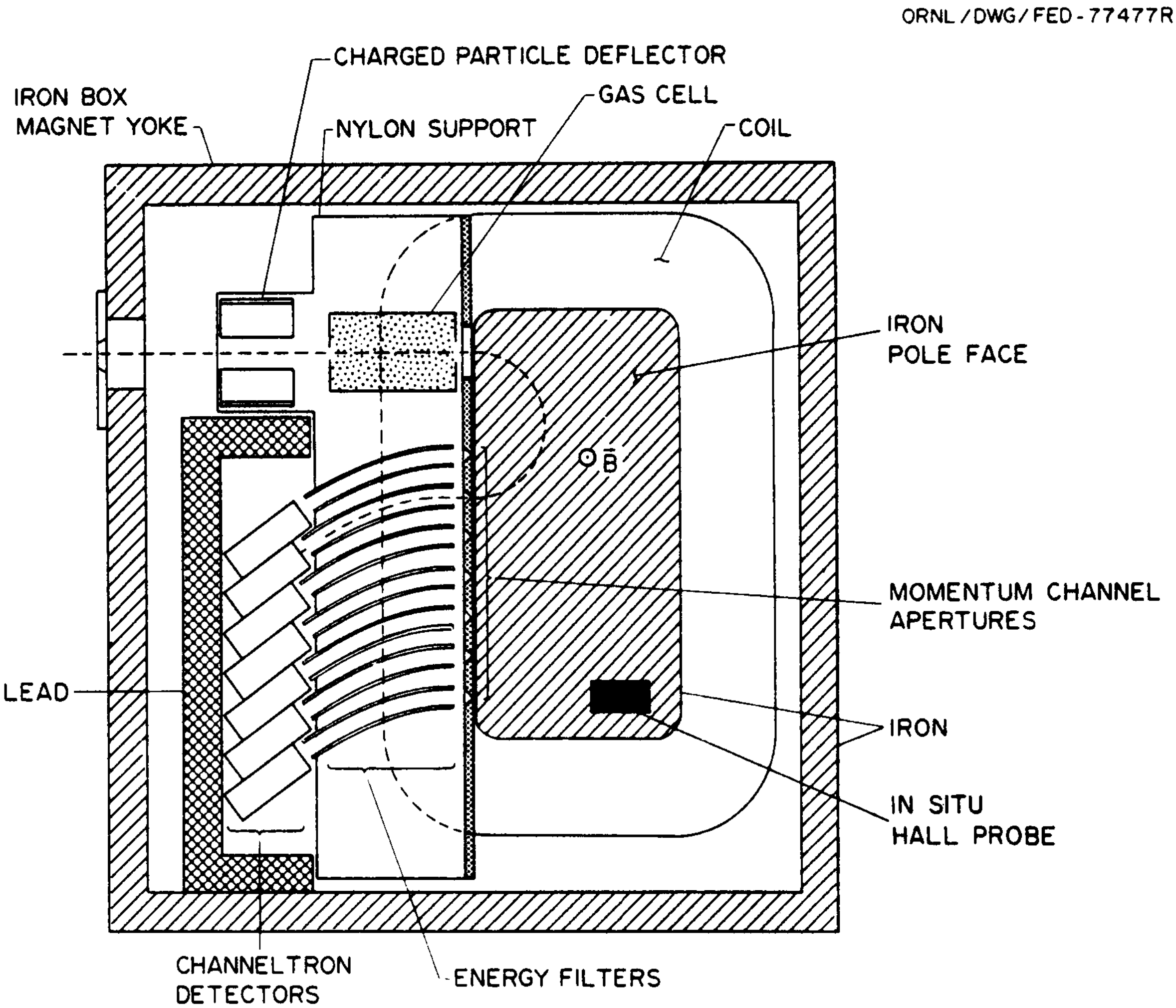

Figure 3-3. Drawing of ISX mass-energy neutral analyzer showing principal components.

ORNL/DWG/FED 78-133 R2

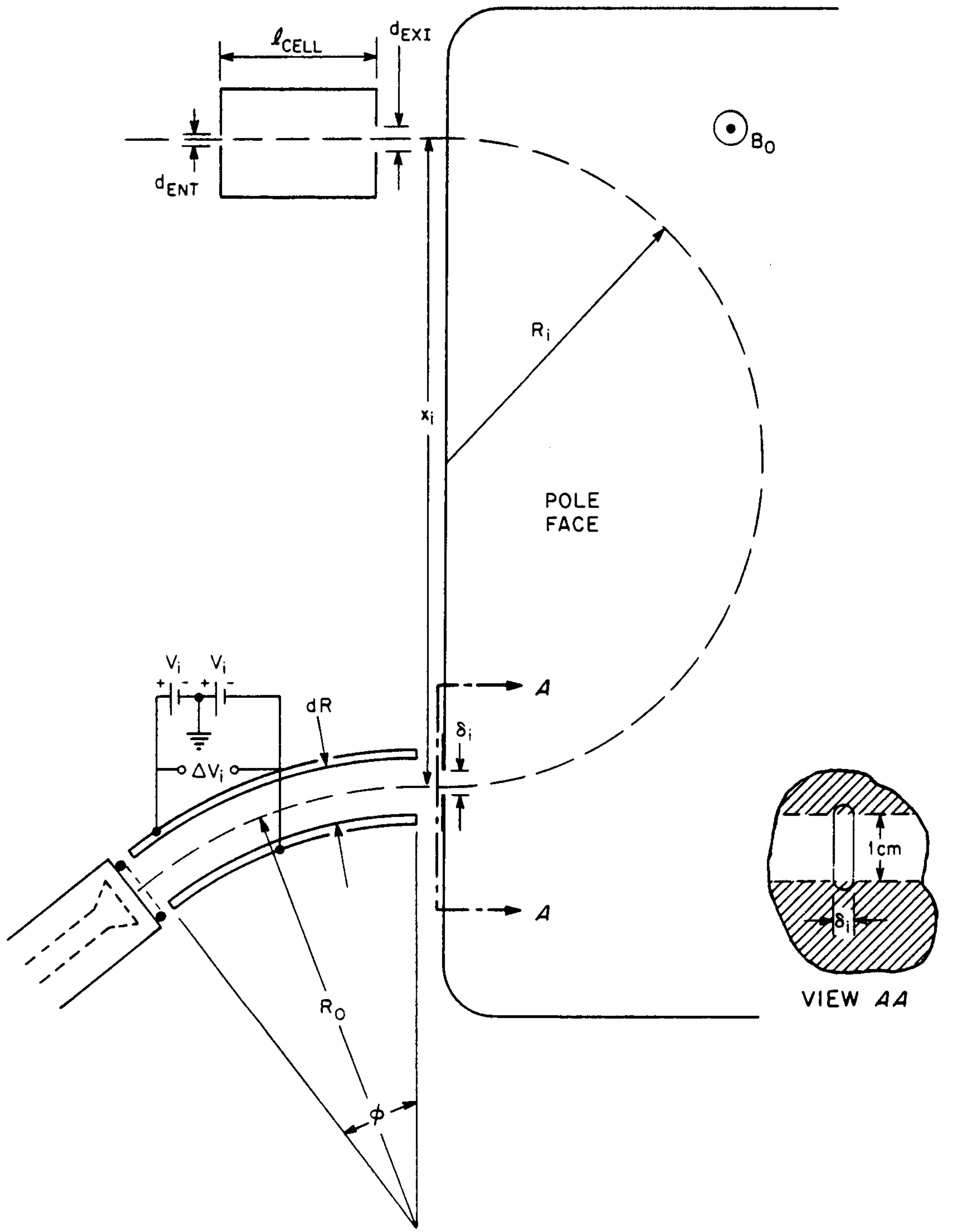

Figure 3-4. Details of a typical channel. Dimensions and other quantities are given in Table 3-1.

TABLE 3-1

MASS-ENERGY ANALYZER PARAMETERS[a]

Specifications

Energy Range	0.3-50.0 keV
Calibrated Range	0.5-10.0 keV
Energy Resolution	5% FWHM
D/H Mass Rejection	100:1
Spectral Coverage	10.6:1; 7 channels

Gas Cell

Stripping Gas	H_2 or D_2
d_{ENT}	1 mm
d_{EXI}	3 mm
ℓ_{CELL}	5.1 mm

Momentum Analyzer

Pole Faces	10.5 cm x 21.0 cm
Gap	1 cm
B_o	0.01 - 0.04 T
Coils	2 in series, 200 turns each
Current	0-10 A

Channel Numbers	1	2	3	4	5	6	7
x_i (cm)	5	7	9	11	13	15	17
δ_i (cm)	0.123	0.173	0.222	0.272	0.321	0.370	0.420

Geometric Formulae:

$$(AE)_7 = 1.20 \times 10^3 \, x_7^2 \, B_o^2$$

$$(AE)_i/(AE)_7 = (x_i/x_7)^2$$

$$\left(\frac{\delta AE_{FW}}{AE}\right)_i = \left(\frac{2\delta_i}{x_i}\right) \cong 0.05$$

Energy Filters

R_o	12 cm
dR	1 cm
ϕ	0.71 rad (40.7_o)
V_i	0-4 kV

Geometric Formulae:

$$E_i = V_i \frac{R_o}{dR} = V_i \times 12.0$$

$$\left(\frac{\delta E_{FW}}{E}\right)_i \cong 2 \frac{dR}{R_o \phi^2} = 0.33$$

[a] Symbols defined in Figure 3-4.

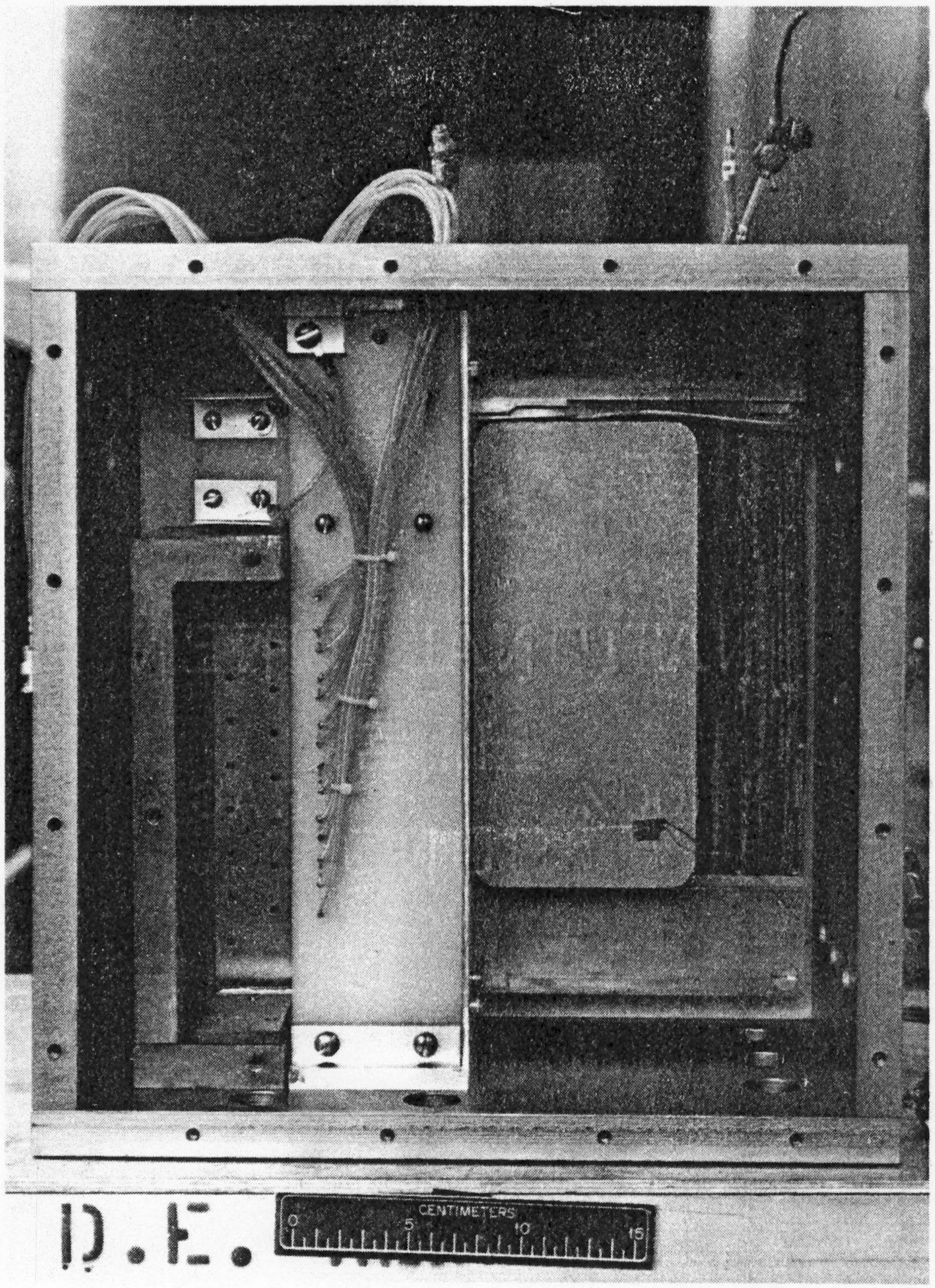

Figure 3-5. Photograph of mass-energy analyzer, partially assembled. The metal detector mounting bracket has been replaced by an extension of the insulating support.

which is affixed to one of the pole faces, as shown in Fig. 3-5, and then calibrated against a commercial gaussmeter. The effective calibration can also be rechecked, using monoenergetic ions from the thermal lithium source.

3.2.1 Magnetic Momentum Analyzer

At first, it might seem that the 180 degree analyzing magnet is unnecessarily large and cumbersome. An alternate approach is that taken by Afrosimov et al.,[28] in which a rather short sector, or wedge-shaped, magnet is used to spread the ion trajectories into a fan. Given a particular detector size (in our case, channeltrons with 1 cm dia. input apertures were to be used), energy resolution is obtained by beam spreading in the nominally field-free region between the magnet and the energy analyzer entrance slit, and defined by the width of the slit itself. To obtain the desired 5% energy window requires a rather large drift distance, compared to the magnet size, in order to spread the high energy ions, which have relatively large radii of curvature in the magnetic field. In this configuration, the trajectories are also sensitive to the detailed focussing properties of the magnet, which are discussed in Appendix A. The concerns here are 1) that focussing in the plane of the trajectory might be accompanied by defocussing in the vertical direction, or vice versa, and 2) that stray, or leakage, fields from the coils and yoke might cause unpredictable steering of the ions as they traverse the drift region.

The 180 degree design avoids these difficulties and provides some additional advantages as well. At a given setting, the more energetic particles have longer trajectories in the analyzer field, a property which compensates for these particles' larger radii of curvature; interestingly, all particles spend the same amount of time in the field. The net displacement of a particle along the edge of the pole face is proportional to its momentum, and the momentum resolution $\delta p/p$ is equal to the slit width divided by the displacement. A particle both enters and leaves the magnet gap normal to the pole face and immediately enters the energy analyzer. The fringing fields thus have no focussing or defocussing effects, to first order. The "bulk" fields focus (in the plane of the trajectory only, as discussed in Appendix A) in this configuration, but the focal length is rather long compared to the close spacing between the momentum and energy analyzers, so the net effect is small. Finally, the design allows the momentum analyzer entrance and exit slits, gas cell, energy filters, and channeltrons to be mounted on a single compact subassembly, as shown in Figs. 3-6 and 3-7, thus facilitating precise positioning and alignment of these critical components. It also permits the nesting of identical energy filters, which is advantageous from the standpoint of fabrication, assembly, and analysis. In summary, the use of a 180 degree magnet is a conservative approach which leads to an analyzer having predictable properties and which is easy to fabricate, despite the drawbacks of large size and weight.

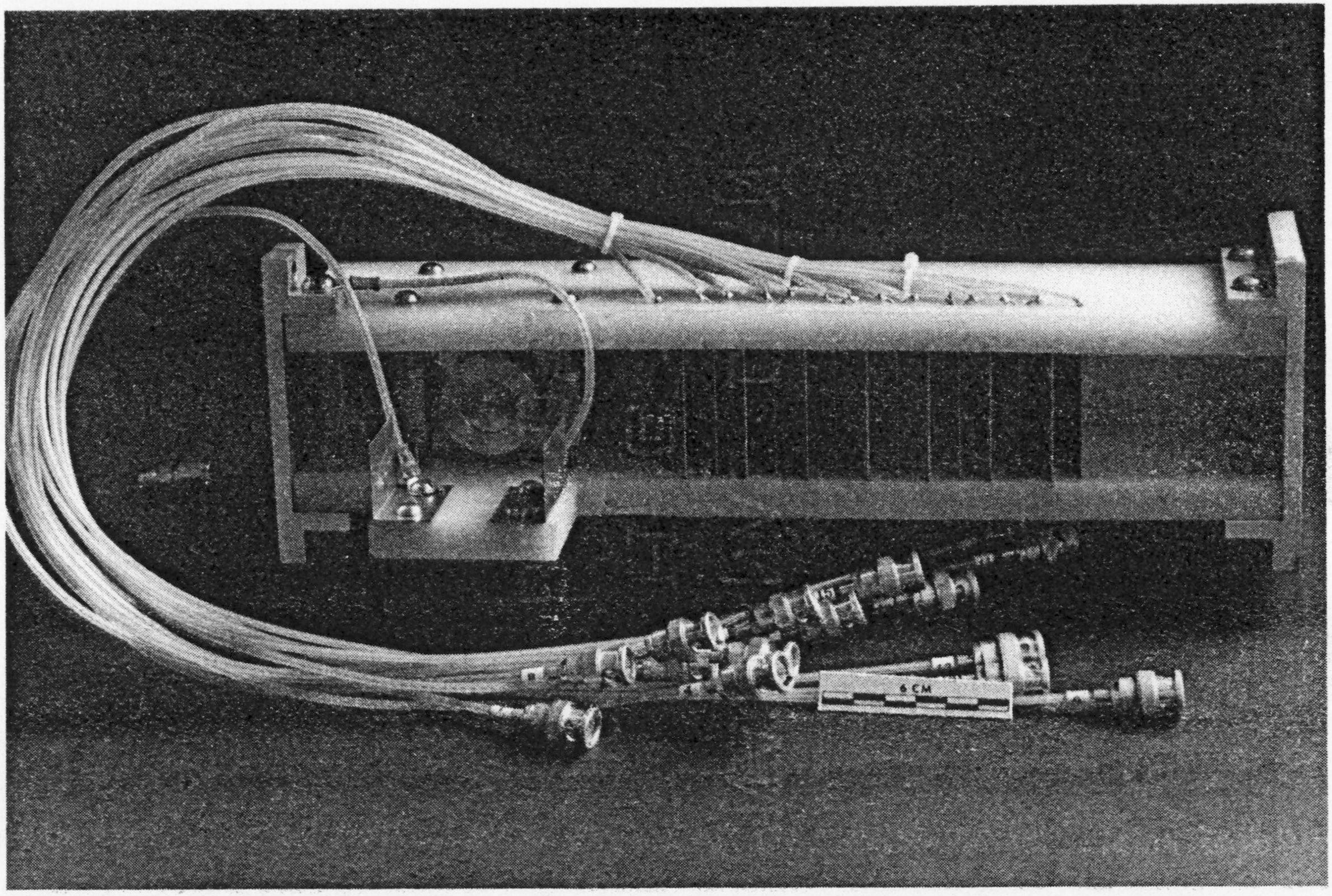

Figure 3-6. Analyzer subassembly showing gas cell, charged particle deflector, energy filters. Detectors have recently been incorporated into this subassembly.

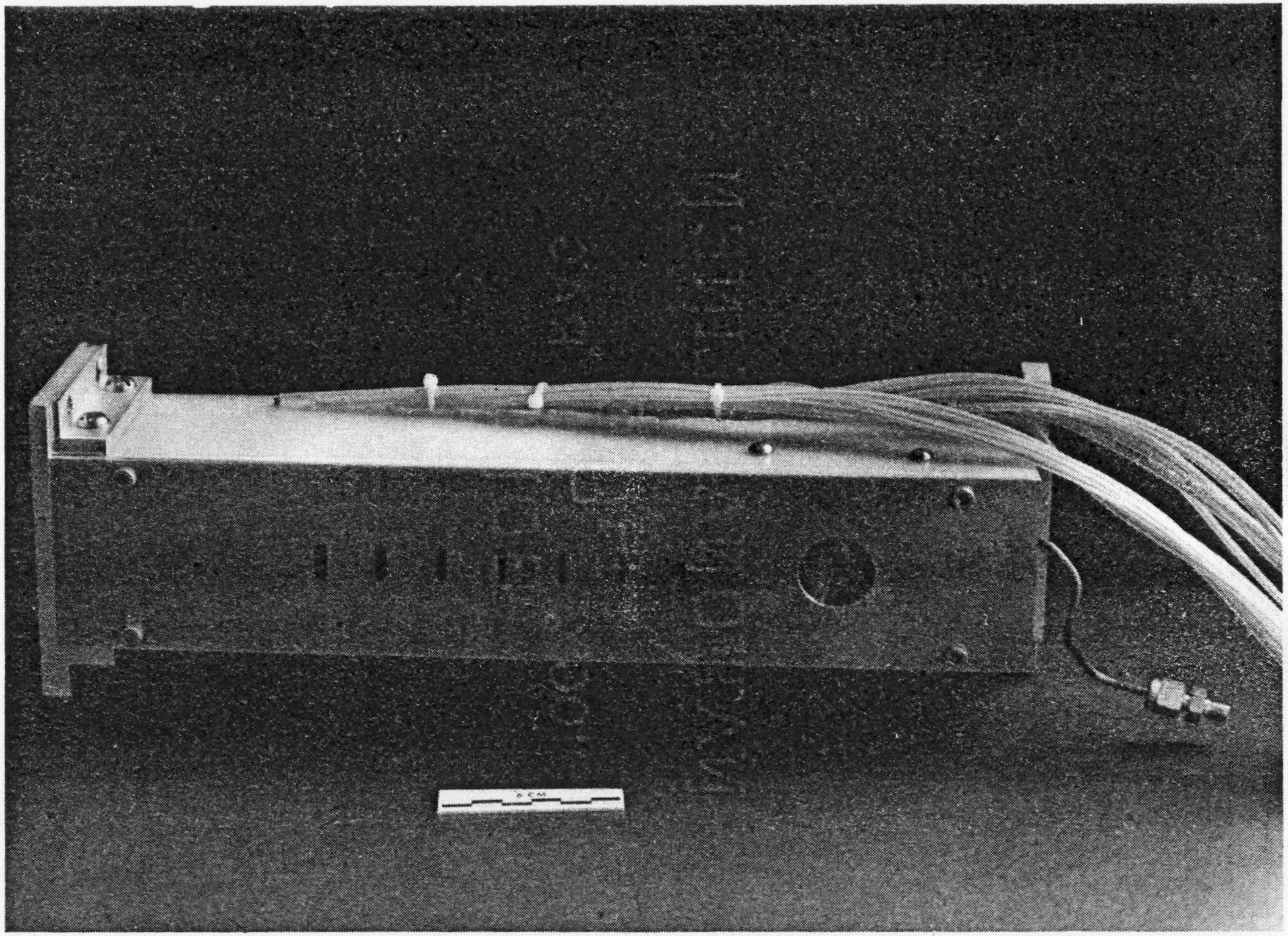

Figure 3-7. Analyzer subassembly showing momentum channel apertures.

3.2.2 Electrostatic Energy Filters

The cylindrical electrostatic analyzers produce a radial electric field which varies as 1/R between the plates, where R is the distance to the common center of curvature of the plates. The zero order trajectory, a circular segment centered between the plates, is followed by particles whose energy is such that the centrifugal outward force balances the centripetal force provided by the electric field. If R_o is the radius of this trajectory, dR the spacing between the plates, and $dR \ll R_o$ then the energy required for the zero order trajectory is given theoretically by

$$E = V\frac{R_o}{dR} \qquad 3.2$$

where E is the energy in eV, and +V and -V are the voltages applied to the the outer and inner plates respectively. The energy resolution, where $\phi<1$, ϕ being the plane angle subtended by the sector, is approximately

$$\frac{\delta E}{E} = 2\frac{dR}{R_o\phi^2} \qquad 3.3$$

The analysis of this type of filter is carried out in Appendix B.

By making $R_0/dR \gg 1$, one can analyze relatively high energy particles with low voltages; in the present system $R_0/dR = 12$. Because only coarse resolution is required, ϕ may be small (~0.7 rad), which facilitates the nesting of the energy filters and channeltron modules, as Fig. 3-3 shows. Because the filters are situated in proximity to the magnet gap and coils, they are immersed in a region of stray magnetic field. This may be seen in Fig. 3-8, which is a plot of the magnetic field in the midplane of the system. Because the field is small, however, it exerts a force on ions in the energy filters approximately parallel to the electric field. Thus this potential problem is only an apparent one because the stray field may be compensated by applying a correction to the (theoretically determined) filter voltages. This effect is also considered in Appendix B; fortunately, it does not alter the fact that the ratios of the seven filter bias voltages are invariant over all energies and masses. This allows the plates to be biased using a pair of high voltage (4 kV) power supplies and fixed external resistive divider networks.

3.2.3 Detector Modules and Counting Electronics

The analyzer employs discrete, funnel-type channeltrons[43] for ion detection. They are encased in small aluminum boxes, shown in Fig. 3-9, resulting in a module which affords (1) a convenient and standardized mechanical mount for the detectors, and (2) shielding against electromagnetic interference from neighboring detectors (crosstalk) or any other high frequency signals which may be present.

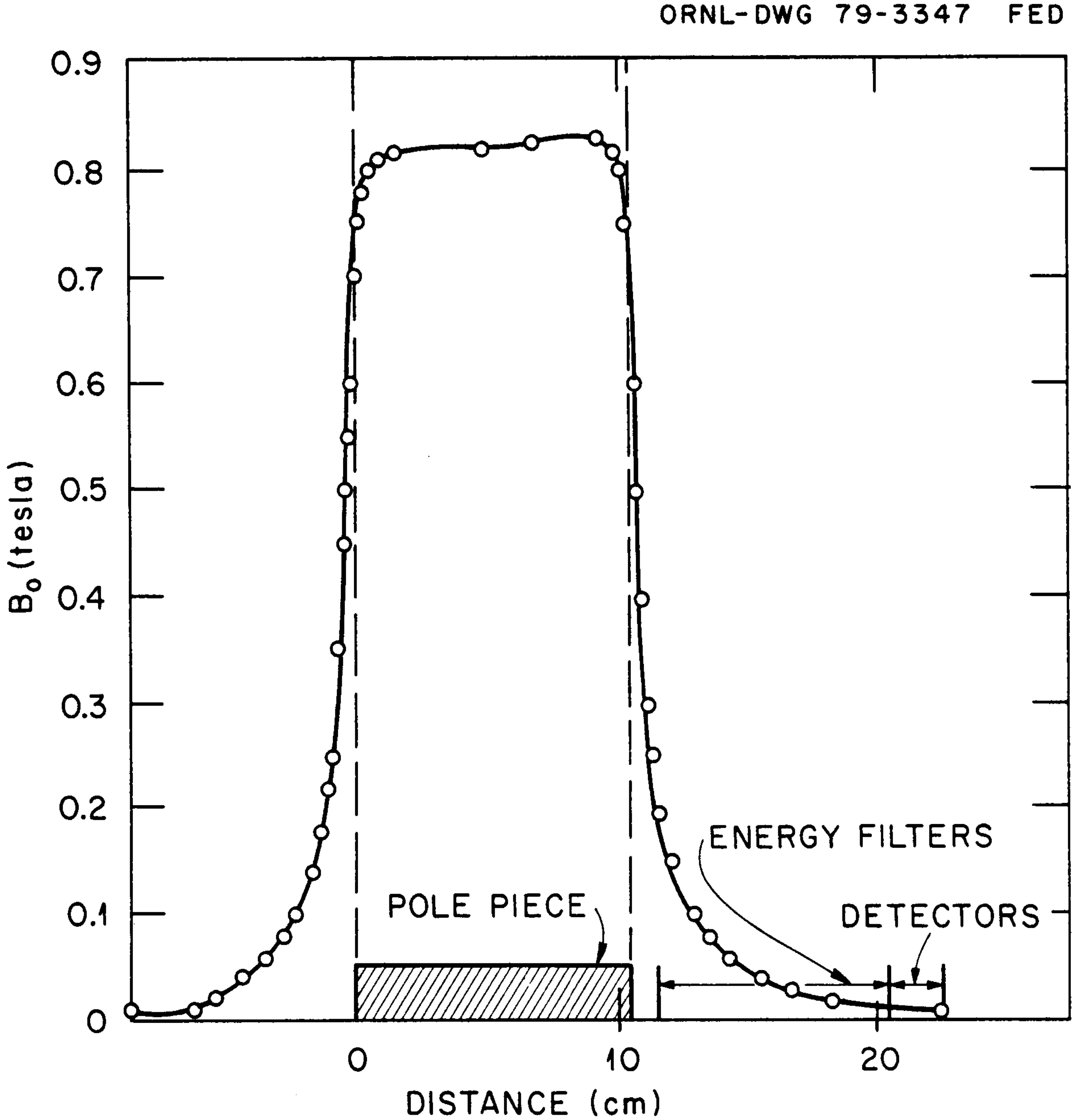

Figure 3-8. Magnetic field strength along analyzer axis. Field was measured in the midplane of analyzer; direction is normal to midplane.

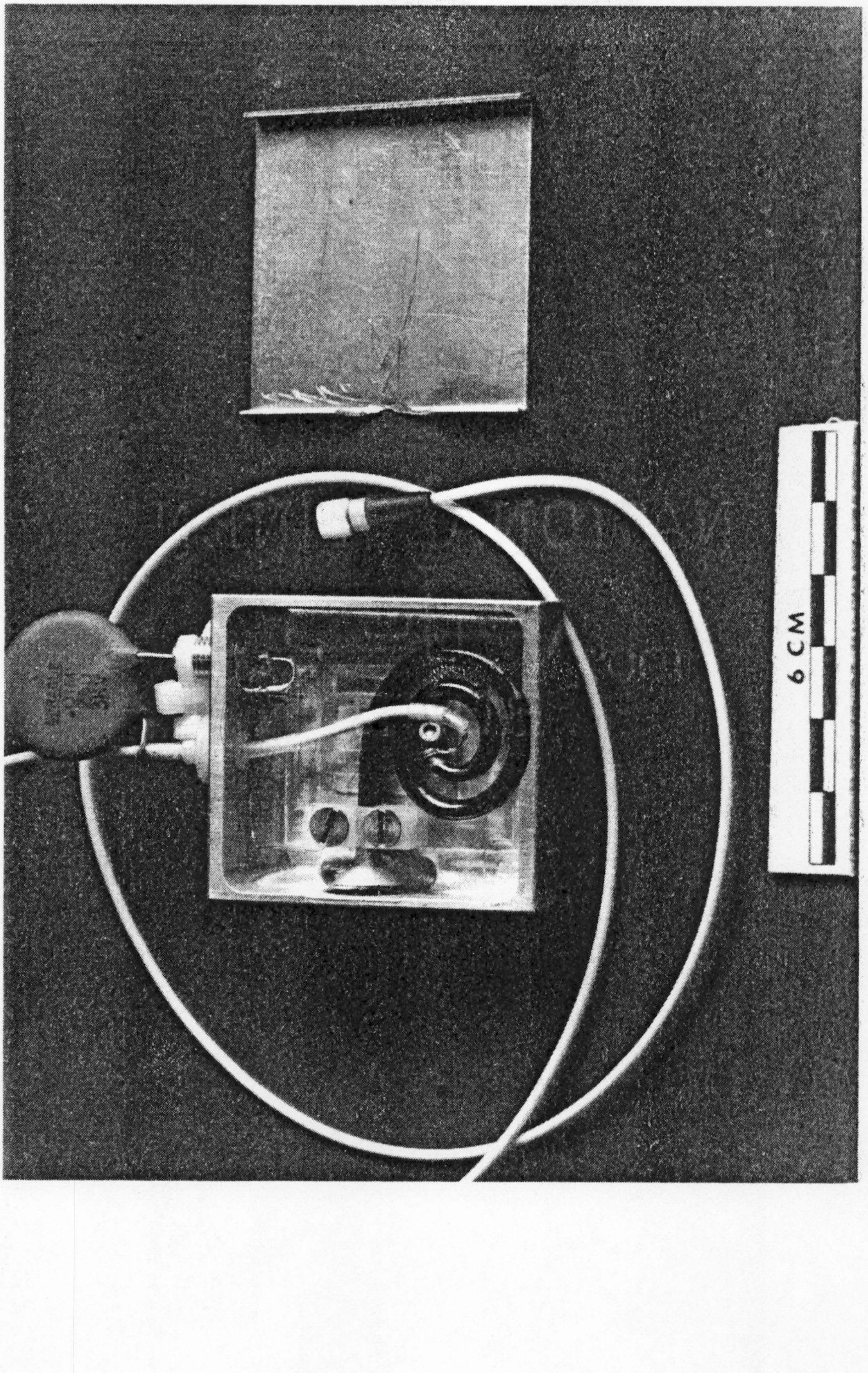

Figure 3-9. Channeltron detector and mount.

Because channeltrons are widely used in many applications, including other neutral particle analyzers, we confine the present discussion to a few problems, particular to the mass-energy analyzer configuration, which were encountered.

Channel electron multipliers, or channeltrons, are attractive because they are rugged, simple, offer electron gain in excess of 10^8, and are operable in a particle counting mode. The latter is desirable over analog techniques because detected neutral fluxes from tokamaks are small and because particle counting techniques are insensitive to gain variations and other noise in the electronics. With the detector input, or cathode, biased at $V_b \cong -3.0$ kV and the output, or anode, at ground potential (through a 50 ohm load resistor), all ions are accelerated through V_b electron volts after being analyzed and before being detected. At energies of 3 keV and above, the detection efficiency for light ions striking the detector surface is practically unity. In this configuration each incident ion normally produces a current pulse of order 1 mA in amplitude and 20 ns in duration at the detector output. External amplifiers, filters, discriminators, and scalers are then used to process and count pulses. At count rates in excess of $\sim 2 \times 10^4$ s^{-1} the detector gain and, hence, the average output pulse amplitude, decrease rapidly with count rate, due to the high resistivity of the electron multiplying surface. By only counting events, this effect is made tolerable up to the point where a significant fraction of the pulse heights fall below the detection threshold of the counting electronics. Therefore, one tries to set the threshold as low as possible; in practice the lower limit was imposed by steady-state noise in the preamplifier. By employing low-noise preamplifiers and pulse shaping amplifiers to optimize the signal-to-noise ratio, the useful count rate was extended to at least $3 \times 10^5\ s^{-1}$ with less than 10% counting losses, which has proven to be adequate for ISX applications. A block diagram of a typical counting channel is shown in Fig. 3-10.

In designing the analyzer, the basic dimensions (slit spacing, pole face area, plate spacing and curvature) were determined basically by the size of the detector and by the number of channels. To minimize the overall size it is necessary to make the detector module as small as possible. Unfortunately, micro-arcing between the detector input, biased at ~3 kV, and the inner surface of a close-fitting grounded box resulted in intolerable levels of background count rate. This problem was solved by electrically connecting the box to the detector cathode, instead of to ground, with conductor and shield of the output cable both insulated from the box. Apparently arcing, if any, which might occur between the (grounded) anode and the box, is benign because the arc currents are not amplified as they are when associated with the cathode. We note that this solution is compatible with the analyzer design since the energy filters and detector modules are mounted on an insulating (G-10) support, anyway. It is still necessary to provide a high frequency connection between the output cable shield and the box to eliminate

ORNL-DWG 79-3346 FED

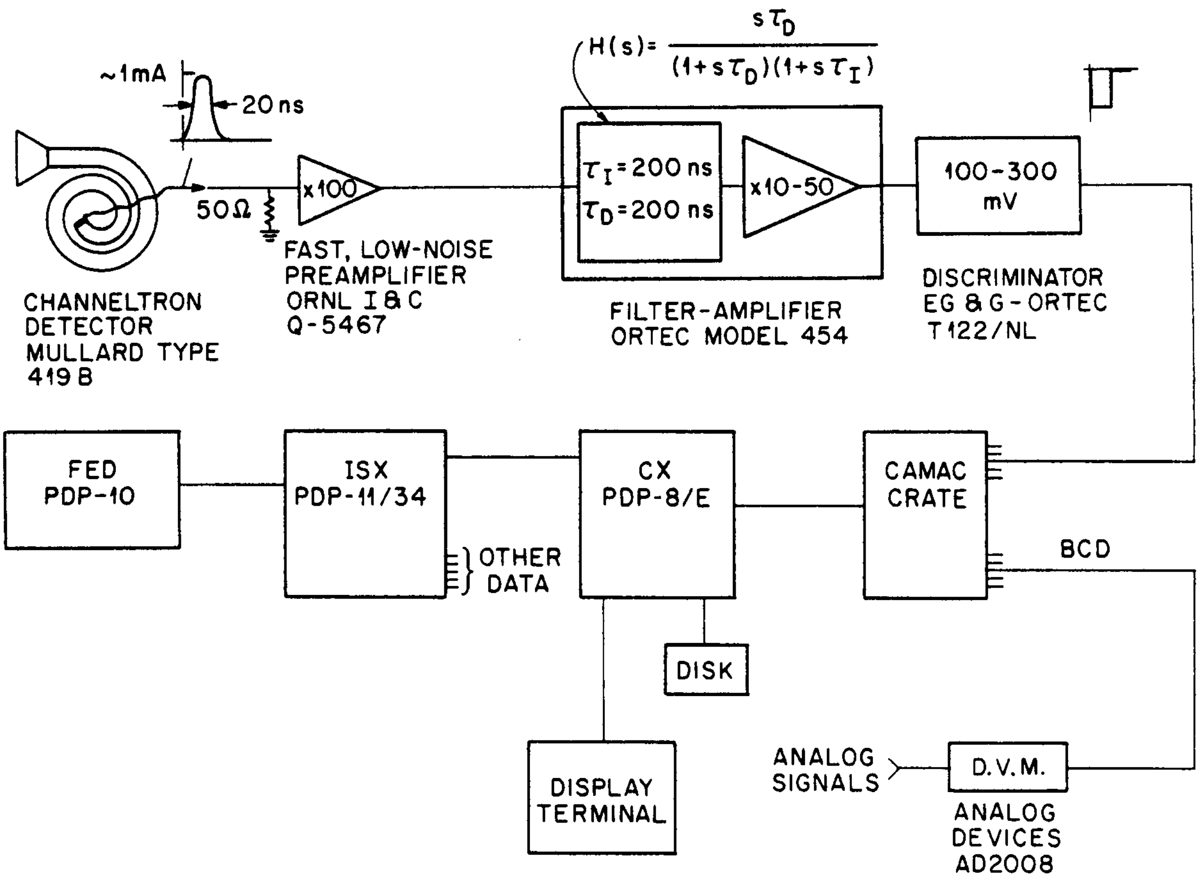

Figure 3-10. Analyzer counting electronics and data acquisition system.

interchannel crosstalk, and this is accomplished with the 0.01 μF capacitor seen in Fig. 3-9.

Given the close spacing between channels and the arrangement of the (biased) detector modules with respect to the energy filters, some modification of the idealized particle optics might be anticipated in the analyzer itself. This was investigated using the lithium ion source discussed previously by adjusting the magnetic field and filter voltages to direct the monoenergetic beam of ^{7}Li or ^{6}Li ions into each detector. One can determine the energy response window of the filters by monitoring the count rate as a function of filter voltage. (Since filter response depends on E/V, this measurement can be related quite easily to the normal application, where the voltage is fixed and a spectrum is to be filtered.) Experimentally, it was found that two important design improvements, described below, were necessary.

First, the detector modules had to be as close as possible to the end of the filter plates. This is probably necessary to minimize the exposure of particles to fields from adjacent channels. Secondly, a high transmission (~90%) grid in front of the module input aperture was needed. This technique was proposed by Ray and Barnett[45] as a means of producing a more uniform field pattern, and therefore detector response, such that particles are accelerated onto the funnel surface of the channeltron rather than down the "throat". Their bias configuration was different, however, and they did not have an enclosing box, so it is not obvious that the same explanation should apply in the present case. The need for these two features was simply an empirical fact, based on test results, which are presented in Fig. 3-11.

3.3 ANALYZER CALIBRATION

Before being implemented on the ISX-A tokamak in late 1977, the mass-energy analyzer was calibrated using a beam of hydrogen neutral atoms in the energy range 0.5 keV $< E <$ 10.0 keV. The purpose of this calibration was to verify the mass-energy analysis characteristics for stripped ions and to measure the overall detection efficiency for neutrals. The former were compared with predictions based on the analyzer's dimensions and electrical configuration, and with measurements made using the built-in lithium ion source. The detection efficiency should be determined mainly by stripping and recapture rates in the gas cell, and therefore agree, at least approximately, with values calculated from published cross sections for these processes. All of these comparisons were made, with satisfactory results, thus providing a high degree of confidence in the instrument's performance.

The apparatus and procedure used in this calibration are similar to those for the electrostatic analyzers used on ORMAK, and are described in more detail elsewhere.[41]* A diagram of that system

---

*The facilities for this calibration were provided by the Atomic Physics Group of the ORNL Physics Division, under the auspices of C. F. Barnett and J. A. Ray. Their assistance, and that of L. A. Massengill, in performing this part of the work is gratefully acknowledged.

ORNL-DWG 79-3545 FED

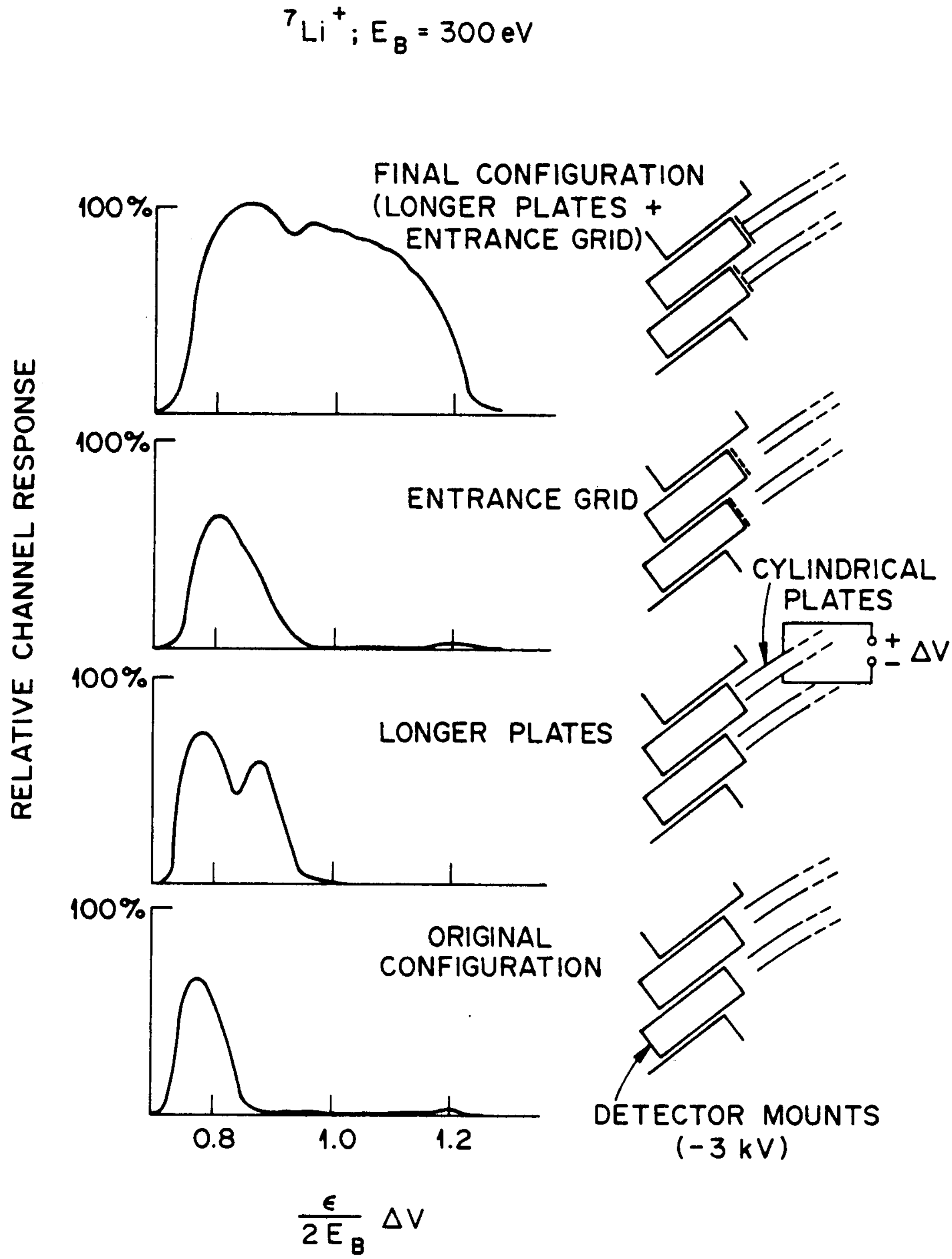

Figure 3-11. Channel response for different configurations of the cylindrical analyzer/detector interface. Cylindrical plates must extend as near as possible to detector and a grid must be placed in front of detector aperture in order to make use of full detector input aperture width.

is shown in Fig. 3-12, where the "parabolic analyzer" is replaced by the mass-energy analyzer. The "momentum analyzer" in the figure refers simply to a bending magnet used to remove fractional energy beam components resulting from molecular dissociation. The purified beam can then propagate to the test analyzer either as ions or, if transmitted through gas in the neutralizing cell, as a beam of neutral atoms.

3.3.1 Momentum Analyzer Calibration

The momentum analyzer calibration is expressible by the ratios μ_i, defined as $\mu_i = \frac{(AE)_i}{B_o^2}$, where $(AE)_i$ is the mass-energy product, in amu-eV, of ions (assumed to be singly charged) which are passed by the i-th momentum channel. B_o is nominally the analyzer gap field, in Tesla, but is actually the output signal from the in situ Hall probe. The μ_i were measured by varying B_o to optimize, in each channel, the detection of an incident H^+ (A = 1) beam at various energies. The data for channel 7 are presented in Fig. 3-13, from which μ_7 was calculated to be 2.93×10^5 amu-eV-T^{-2}. By comparison, we calculate this quantity to be 3.47×10^5 from the dimensions and formulas given in Table 3-1. The discrepancy is almost completely explained in terms of a calibration error in the Hall probe circuit, which was subsequently corrected, along with the μ_i values.

The ratios μ_i/μ_7 are solely functions of the relative positions of the exit slits, a fact which was verified experimentally. The calculated and measured ratios are given in Table 3-2. Similarly, the resolution $[\frac{\delta(AE)_{FWHM}}{(AE)}]_i$ of each channel is a function of the geometry,

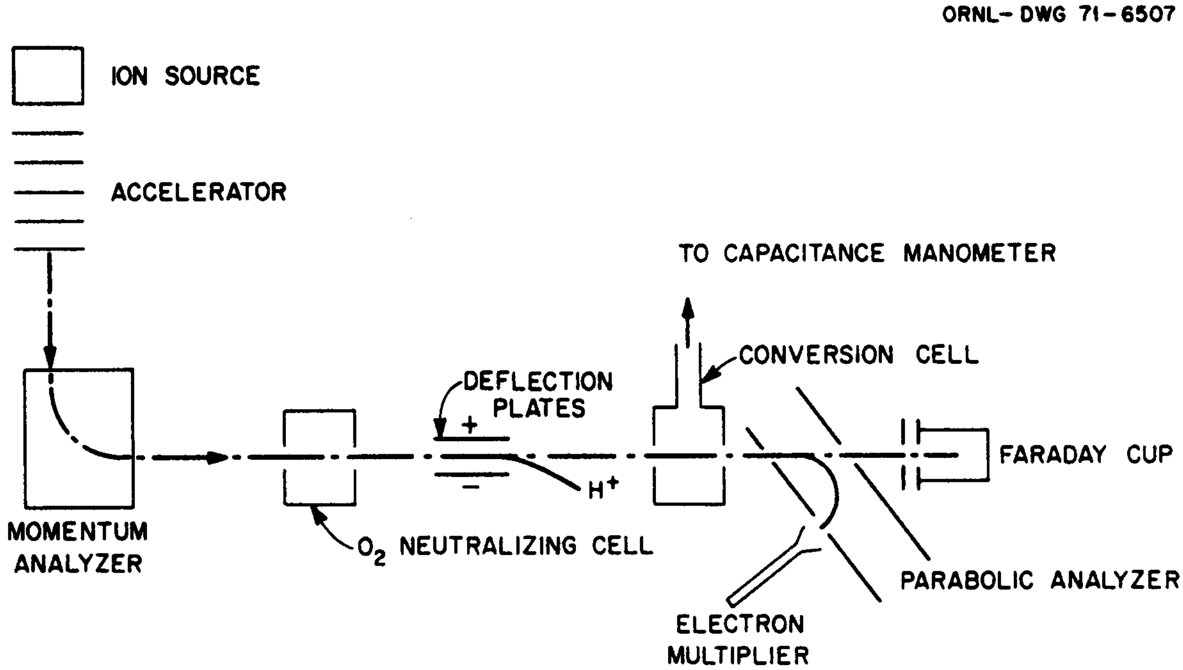

Figure 3-12. Analyzer calibration setup similar to that used for present analyzer. (Source: Ray and Barnett, IEEE Trans. Nucl. Sci. NS17, 1 (1970) 44.)

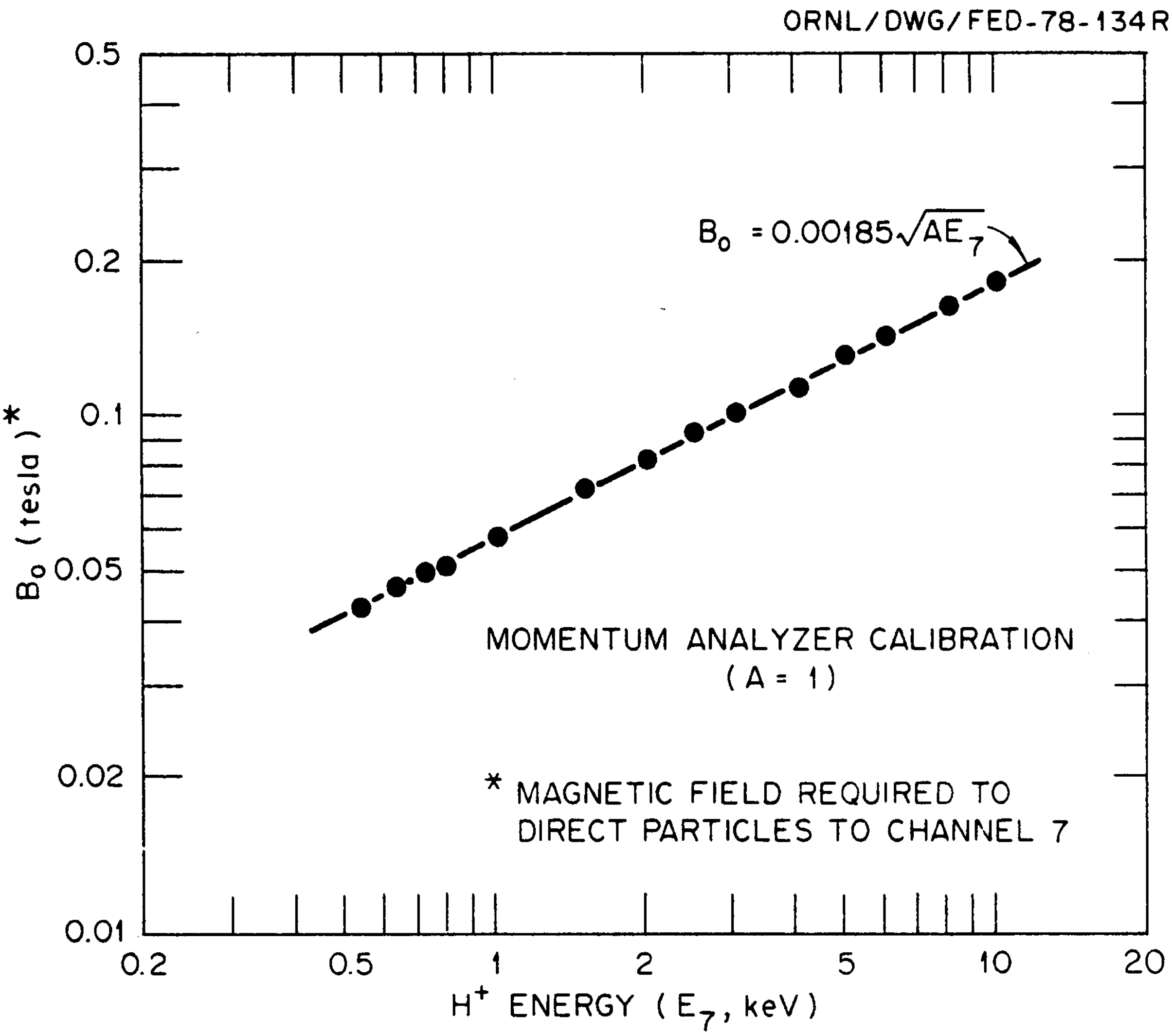

Figure 3-13. Momentum analyzer calibration. B_0= const. × $\sqrt{AE_7}$); constant is slightly in error due to miscalibration of in situ hall probe, later corrected.

TABLE 3-2

MASS-ENERGY CALIBRATION DATA

$\mu_7 = 3.84 \times 10^5$ (measured); 3.47×10^5 (calculated) amu-eV-T^{-2}

Channel (i)	$\frac{\mu_i}{\mu_7} = \frac{(AE)_i}{(AE)_7}$		$\varepsilon_i = \frac{E_i}{V_i}$	
	measured	calculated	measured	calculated
1	.081	.087	8.70	12.0
2	.167	.170	9.26	12.0
3	.278	.280	10.00	12.0
4	.423	.419	10.00	12.0
5	.580	.585	10.80	12.0
6	.780	.779	11.00	12.0
7	1.000	1.000	11.40	12.0

namely the ratio of the slit width to the displacement. It was measured in a slightly indirect manner, by fixing the energy of a H^+ beam, as above, and varying B_o to find the peak and half-peak count rates. Since $(AE)_i$ is proportional to B_o^2, and the slit width is small, the relation

$$\left(\frac{\delta AE}{AE}\right)_{B_o} \cong 2\times \left(\frac{\delta B_o}{B_o}\right)_{AE} \qquad 3.4$$

may be used to calculate the desired quantity from the measurements. The analyzer was designed with different slit widths in each channel, such that the resolution is a constant (5%) and this was verified as well.

3.3.2 Energy Filter Calibration

The i-th momentum slit passes protons (A = 1) at energy E_i = $(AE)_i = \mu_i B_o^2$, and ions of mass A at energy E_i/A. The energy filters effectively perform the mass analysis by selecting the desired energy component of the momentum beamlet. Their calibration is expressible by the ratio $\varepsilon_i = E/V_i$, where E is the median energy, in eV, of singly charged ions passed by the i-th filter, and $+V_i$ and $-V_i$ are, respectively, the outside and inside cylindrical plate bias voltages. The ratios ε_i, as well as the resolutions $(\delta E_{FWHM}/E)_i$, were determined by adjusting B_o to direct the H^+ beam to the i-th channel and then recording the count rate as V_i was varied. The ε_i measured in this manner are tabulated in Table 3-2; they differ from the theoretical value of 12.0 due to the fringing magnetic field, as explained in the previous section. A universal response curve for the filters is obtained by plotting the measured count rates, normalized to their peak value, as a function of $(E/\varepsilon V)$, as is done in Fig. 3-14. The figure shows that the FWHM of the response curve is about 25% of the median energy, in fair agreement with the value of 33% predicted. The response curve is also seen to be down by more than two orders of magnitude at half and twice the median energy, corresponding respectively to rejected deuterons or protons, depending on which is the selected species. This implies a mass rejection ratio greater than 100 to 1, as desired. We note that mass rejection may be checked during normal tokamak operation by setting the filters to accept masses between A = 1 and 2, when both H and D are present. Results of such a test made during ISX-B operation are given in Table 3-3, confirming the good mass rejection.

3.3.3 Detection Efficiency Calibration

The net detection efficiency $\eta_i(E)$ is defined to be the ratio of detected ions in the i-th channel to the number of neutrals at energy E entering the gas cell, when B_o and V_i are adjusted to maximize the detected flux. The incident neutrals were measured both by turning off the gas cell feed and by zeroing the magnetic field so as to make the analyzer transparent, causing both stripped and unstripped particles to strike the target of the Faraday cup. The secondary electron ejection coefficient was measured, and found to be in agreement with that reported in reference (41); thus the neutral flux

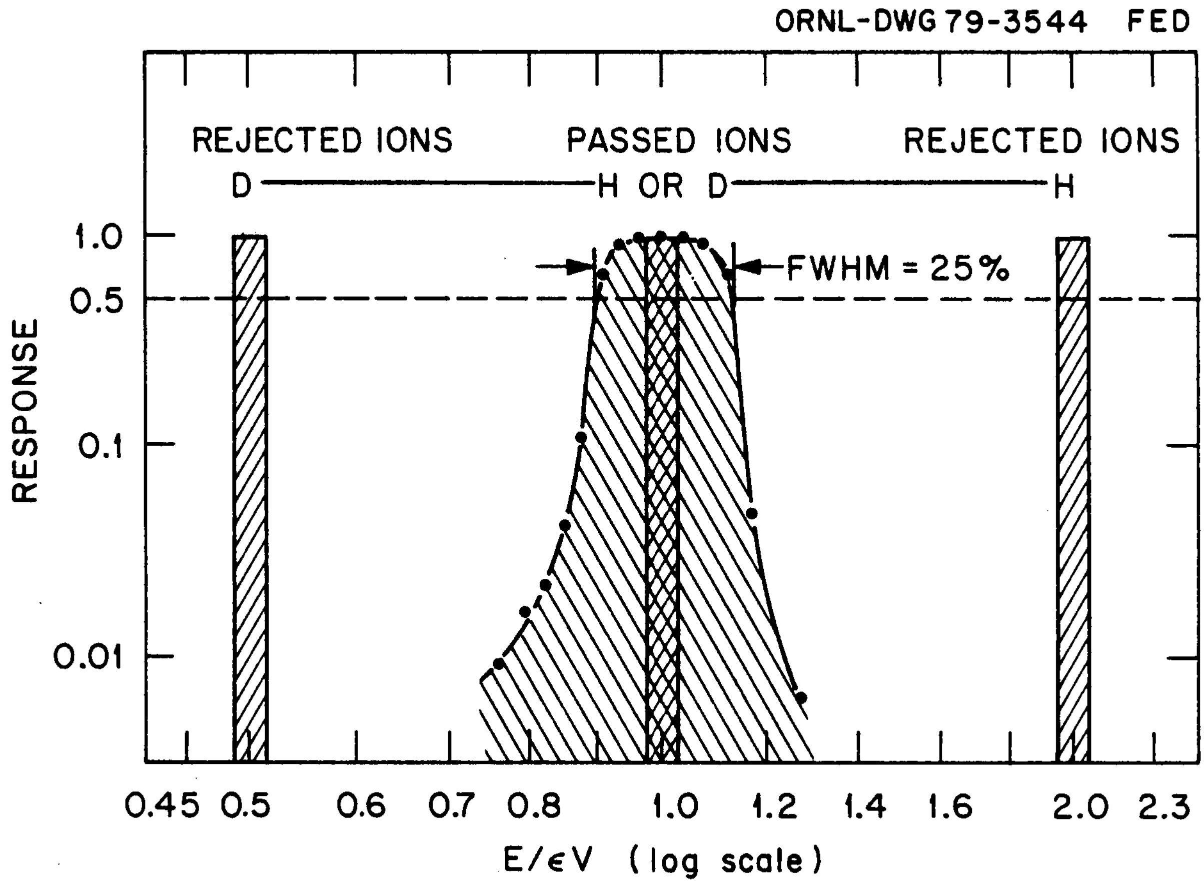

Figure 3-14. Energy filter calibration. When analyzer is set to detect deuterons, protons occur at twice the deuteron energy. Energy dispersion is narrow enough to reject them by a factor greater than 100, but wide enough to allow for up to 10 per cent errors in field settings, which might result from, e.g. drift in the Hall probe.

TABLE 3-3

OPERATIONAL MASS REJECTION TEST

Counts recorded in 10 ms during neutral beam injection on ISX-B

B_o = .2224 T
AE_7 = 19 amu-keV

SHOT	V_{DIV}^{a}	A^{b}	CHANNEL =	2	3	4	6	7
			AE =	3.2	5.3	8.0	15.0	19.0 amu-keV
11949	865	2.0		1140	640	255	14	6
11950	1015	1.7		480	22	18	2	3
11955	1080	1.6		40	30	11	2	2
11953	1150	1.5		13	14	9	4	2
11954	1235	1.4		9	17	10	6	3
11957	1730	1.0		600	550	510	230	140

[a] External Divider Voltage

[b] Mass Setting From B_o, V_{DIV}

can be reliably inferred by measuring the secondary electron current. The cell was operated with H_2 at a constant flow rate of 0.040 atm-cc/s, which corresponds to a cell pressure of 8.7 mtorr, using data given in reference (41) and formulas for the gas conductance out of the cell.[46] H^o detection efficiency for a typical channel is plotted as a function of energy in Fig. 3-15, which also shows values calculated from the cross sections σ_{01} and σ_{10} for H^o on H_2.[47,48] The other channels had net efficiency curves similar to, and generally within 10% of, that of channel 3. Efficiencies for D_2 stripping gas were checked in order to verify that they were the same as for H_2 provided the same cell pressure was maintained. No calibration for incident D^o was performed, but previous work has shown that the efficiency for D^o at energy E is that of H^o at energy E/2, being essentially a function of the velocity.[41]

3.4 IMPLEMENTATION ON ISX

For all the experiments which will be described in this report, the mass-energy analyzer was used as a fixed-chord quasi-perpendicular neutral diagnostic. While spatial scanning would have been highly desirable in terms of profile measurements, it was precluded by the configuration of the analyzer vacuum tank, which had been designed for another application. The term "quasi-perpendicular" refers to the fact that the analyzer was oriented at an angle of 84 degrees with respect to the magnetic axis of the plasma, for reasons which will be explained below. In the near future, a new scanning analyzer will be substituted as the perpendicular diagnostic, and the present

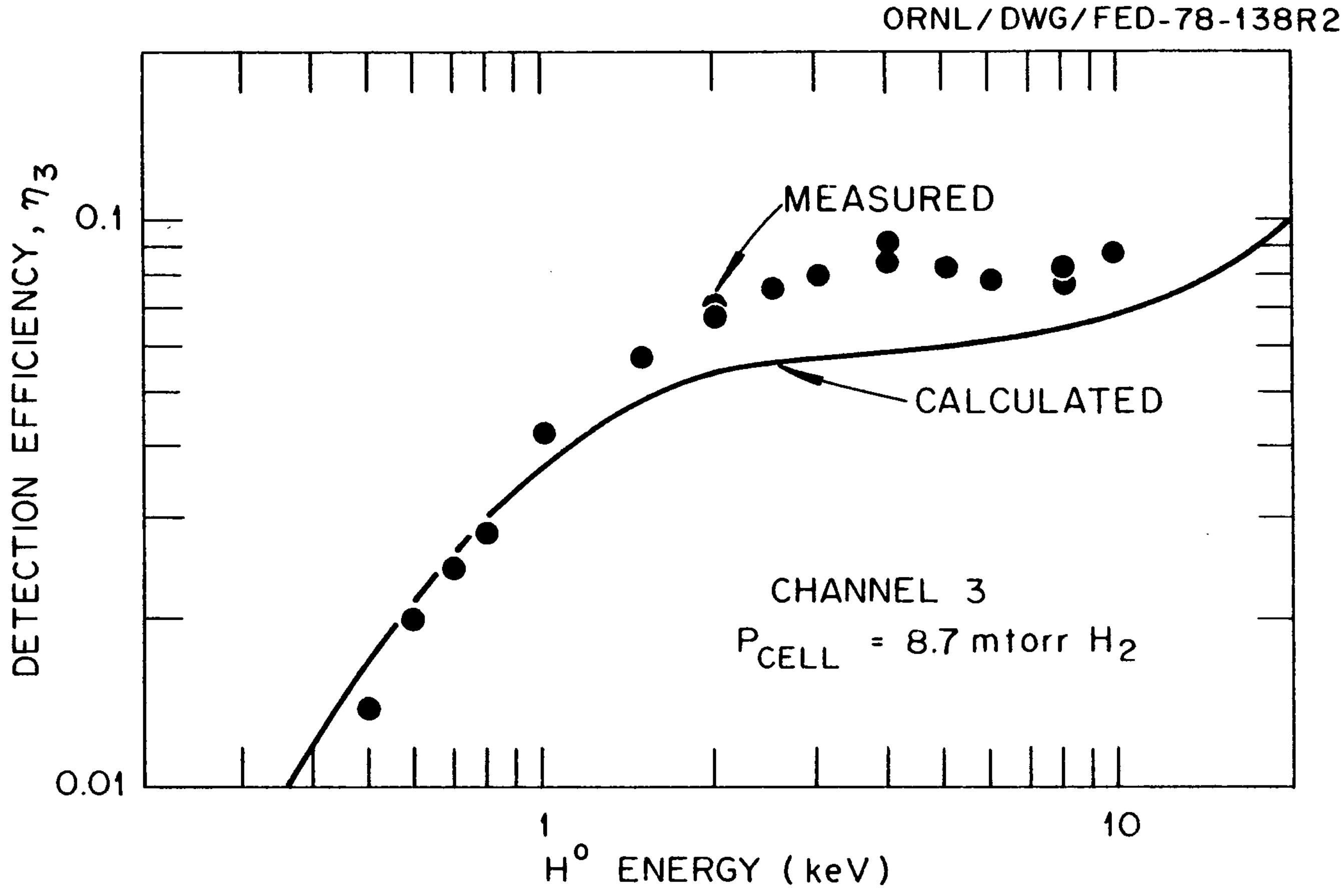

Figure 3-15. Net analyzer detection efficiency for channel 3. Discrepancy between calculated and measured efficiencies (20 % max.) is within experimental errors both in present calibration and in published cross sections used in the calculation.

mass-energy analyzer reconfigured as a scanning tangential (to the toroidal magnetic field) analyzer, in order to better study the details of fast ion spectra and toroidal rotation of the bulk plasma.

3.4.1 Viewing Geometry

The location and orientation of the analyzer with respect to the ISX-A tokamak (The configuration on ISX-B is identical except for slight differences in the dimensions.) is illustrated in Fig. 3-16. The viewing aperture dimensions shown in the figure define a viewed spatial solid angle of 8.0×10^{-5} sr; the column diameter, and hence the spatial resolution, at the plasma center is about 1.4 cm.

Being essentially a perpendicular analyzer for most purposes, the instrument views trapped plasma ions, that is, those with "banana" trajectories. However, the small inclination from perpendicular avoids a subclass of the trapped ions, namely those whose velocities are nearly perpendicular to the field such that they are trapped in the weak local ripples resulting from the discrete toroidal field coil set. These particles are subject to uncompensated vertical $\underset{\sim}{B} \times \underset{\sim}{\nabla} B$ drifts and are toroidally localized unless they scatter within a ripple bounce time. Conceivably, they can constitute an unrepresentative class of ions because of these singular transport properties.[49]

In ISX, the intrinsic vacuum ripple δ is about 0.01% at the center and, at worst, 0.6% near the outside edge. The boundary angle for ripple trapping is given, from elementary guiding center theory, as:

ORNL-DWG 79-2220 FED

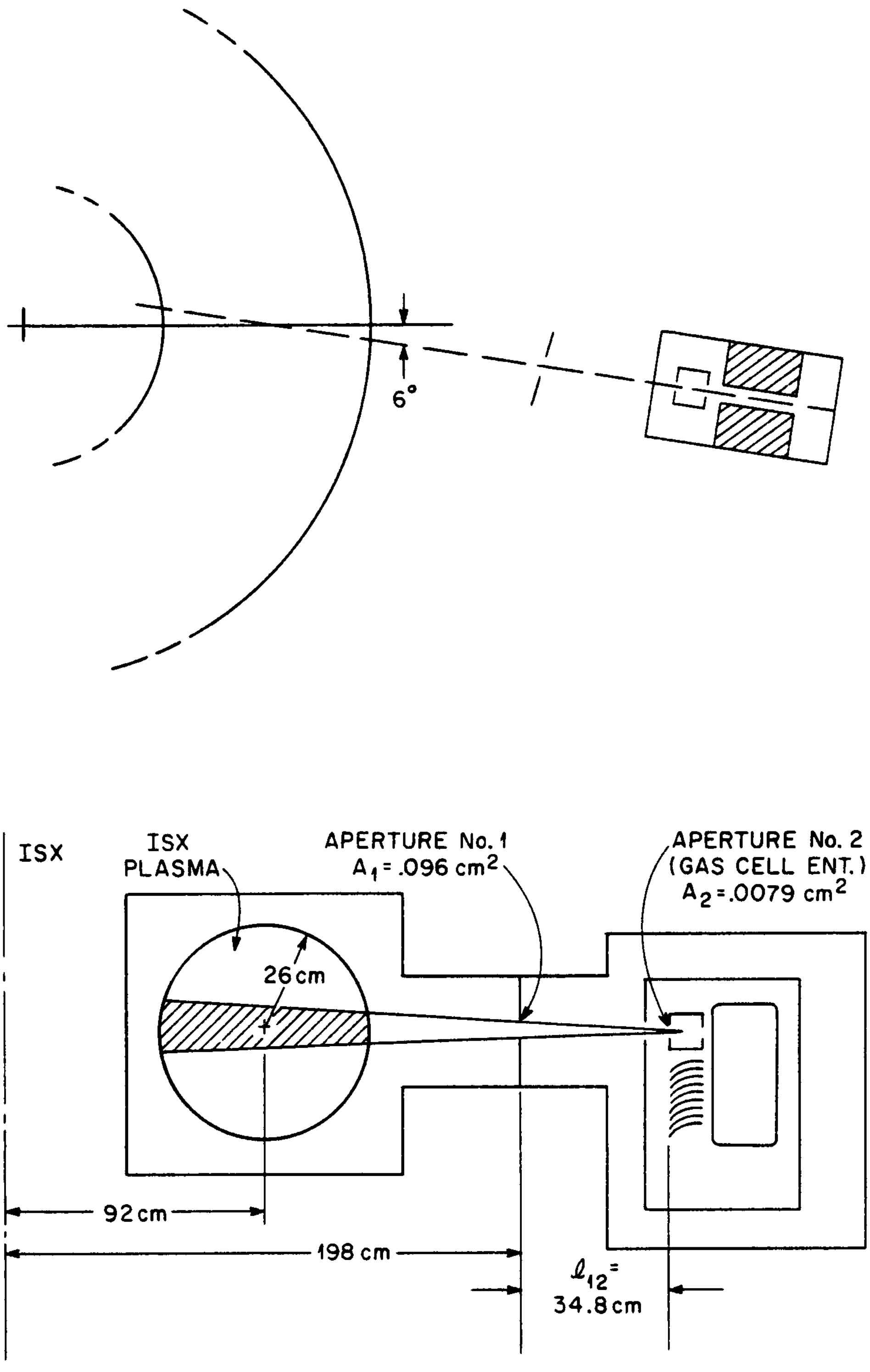

Figure 3-16. CX analyzer viewing geometry for ISX-A. Six degree inclination is to avoid possible ripple effects. ISX-B geometry is nearly the same except ℓ_{12}=46.2 cm.

$$\tan(\theta_{trap}) = \frac{v_{\parallel}}{v_{\perp}} \cong \sqrt{2\delta} \qquad 3.5$$

From this, θ_{trap} is calculated to be less than 6 degrees over the whole plasma, so the choice of 84 degrees (with respect to the toroidal field) for the viewing angle avoids this region everywhere. In fact, at typical ISX densities (2-10 × 10^{13} cm^{-3}) it was calculated that ions with energies less than ~10 keV are unlikely to execute even a single bounce in the ripple before being scattered out of the ripple-trapped orbit. We conclude, therefore, that the problem of intrinsic ripple trapping would be a minor one in ISX. The analyzer was oriented slightly off perpendicular simply because effects such as up-down asymmetries possibly attributable to ripple have been seen on other tokamaks. In the near future, horizontal scanning will be incorporated in the ISX perpendicular analyzer in order to investigate this and other ripple-related effects.

3.4.2 Data Acquisition

A Digital Equipment Corp. PDP 8/E processor is used, in conjunction with CAMAC electronics, to accumulate the data, automatically record settings of the magnet field (B_o) and energy filter voltages (+V,-V), and perform on-line analysis.* Data are

*The data acquisition system has been developed and maintained by D. R. Overbey.

subsequently transferred to disk files on the Fusion Energy Division PDP-10, where they are archived, together with other data from the experiment, and are available for more extensive off-line analysis. The block diagram, Fig. 3-10, also shows these elements of the system.

Each tokamak shot, lasting up to 250 ms, is divided into time intervals, usually of 1 to 2 ms, during which pulses from the seven analyzer channels are counted simultaneously in CAMAC scalers. After each interval the number of counts registered in each channel is stored in a memory location which corresponds to that interval and that channel. The scalers are then cleared and restarted for the next interval. Immediately after the shot, the data are thus contained in a (number of channels) × (number of intervals)-word array in memory. The analyzer field settings are read, within about 1 second, through digital voltmeters and a CAMAC interface, and this information is added to the data array also. Other parameters which are recorded are the clock interval, data format information, a pointer specifying one of several calibration parameter tables, the date, time of day, and ISX shot number. The product is a disk file which contains not only the experimental data, but virtually all of the auxiliary information needed to interpret them. These capabilities make it feasible to analyze, repeatedly if necessary, a data base consisting, at this writing, of nearly 2×10^4 shots, and which increases at the rate of nearly 10^2 per operating day.

On-line analysis is aimed at enabling the experimenter to monitor his data and at providing preliminary results based on individual shots. An example of this analysis is provided in Fig. 3-17, which displays the number of counts measured in 10 ms intervals throughout a shot, as well as the ion temperatures calculated from these data. Final results, however, are based on off-line analysis of series of shots. The methods used there will be described in the following chapter.

SHOT NO. 16850 10/ 1/79 17: 0 AMU= 2.0 E7= 6065.9 EV
E0=0.1778 T; VPLUS,VMINUS= 547.0 -547.0 V MOD NO. 16
EMIN.EMAX= 500. 5000.

CHANNEL	1	2	3	4	5	6	7	
ETA	0.003	0.014	0.033	0.052	0.065	0.074	0.078	
IGNORE?	1	0	0	0	0	0	0	
ENERGY	493.	1011.	1683.	2563.	3518.	4699.	6066.	
0.0- 10.0	0	1	2	1	1	2	3	1202.
10.0- 20.0	0	11	2	0	0	0	0	213.
20.0- 30.0	0	48	13	6	1	0	1	376.
30.0- 40.0	0	89	29	3	0	0	0	266.
40.0- 50.0	0	53	20	0	2	0	0	406.
50.0- 60.0	1	54	25	2	0	1	1	506.
60.0- 70.0	1	83	40	11	7	1	1	484.
70.0- 80.0	9	108	40	20	3	0	0	391.
80.0- 90.0	16	108	80	38	6	4	3	524.
90.0-100.0	34	211	156	100	28	13	10	595.
100.0-110.0	50	270	264	146	76	27	2	641.
110.0-120.0	66	323	323	207	100	37	8	656.
120.0-130.0	79	325	374	259	101	38	23	650.
130.0-140.0	96	402	458	312	143	65	20	674.
140.0-150.0	72	501	517	314	154	56	15	652.
150.0-160.0	81	474	526	364	182	47	14	644.
160.0-170.0	78	452	452	325	141	46	12	644.
170.0-180.0	52	489	496	290	147	53	11	549.
180.0-190.0	21	366	277	195	82	60	32	696.
190.0-200.0	0	54	13	1	0	0	0	242.
200.0-210.0	0	86	20	3	0	0	0	262.
210.0-220.0	0	2	0	0	1	0	0	668.
220.0-230.0	0	1	1	1	0	4	3	2050.
230.0-240.0	0	1	0	0	0	0	0	2.

SHOT NO. 16850 10/ 1/79 17: 0 AMU= 2.0 E7= 6065.9 EV

1; 493.2 EV; 0.33E-02
2; 1010.6 EV; 0.14E-01
3; 1683.3 EV; 0.33E-01
4; 2563.5 EV; 0.52E-01
5; 3518.2 EV; 0.65E-01
6; 4699.3 EV; 0.74E-01
7; 6065.9 EV; 0.78E-01

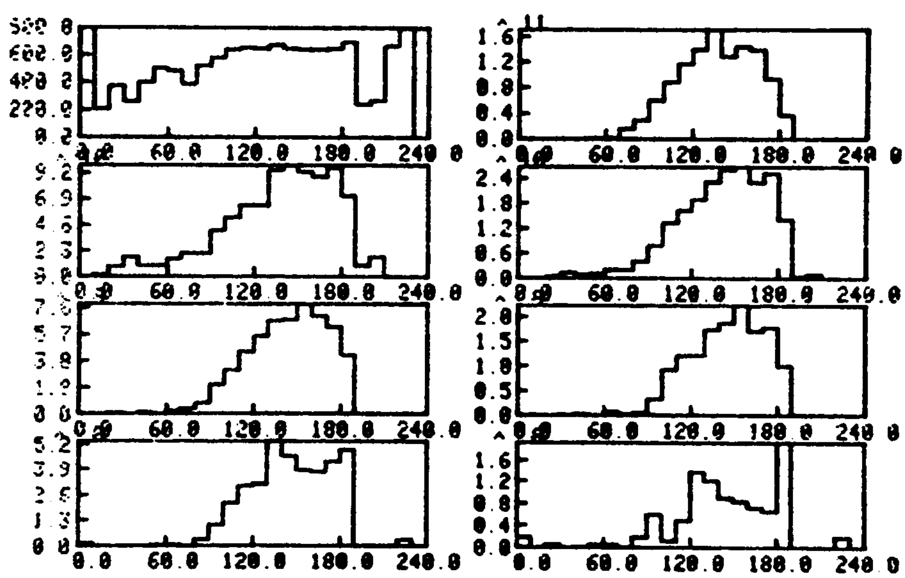

Figure 3-17. Sample on-line data analysis. Table (a) and plots(b) show counts registered in 10 ms time intervals throughout the shot, and uncorrected ion temperatures calculated therefrom. For convenience, Channel 1 display is actually the measured neutron count rate. Neutral beam heating beginning at 70 ms is evident from both the CX and the neutron data.

CHAPTER 4

INTERPRETATION OF CHARGE EXCHANGE DATA

The essential parameter to be obtained from tokamak CX analysis is the ion temperature T_i, which is derived mainly from the shape of the spectrum. Because the magnitude of the CX flux is proportional to the residual neutral atom density, one also would expect to be able to measure the latter if the absolute magnitude of the flux were known. (However, we shall see that such results must be interpreted with caution.) The traditional analysis technique for CX data is to plot the logarithm of the measured fluxes versus energy, then determine the slope and intercept of a straight line which best fits the data; the central temperature is taken to be the negative reciprocal of the slope and the neutral density is computed from the intercept, using the ion density and temperature.[25] However, this method neglects important effects arising from the chord-integrated nature of the measurement: non-uniform plasma and neutral density profiles, and attenuation of escaping CX neutrals. The most serious problem is the tendency for the neutrals to be concentrated near the edge of typical tokamak discharges. This effect, which makes the measured spectra be less representative of the center, becomes increasingly important with increasing density and machine size.

In this chapter, we describe a plasma model fit (MF) data interpretation method which was extended from methods developed for analyzing ORMAK CX data,[26] and which takes the profiles, including the neutral profile, and related effects into account. It is also capable of handling data from multi-chord measurements in a comprehensive fashion, when such becomes available. Densities as high as 7-9 × 10^{13} cm^{-3} (line averaged) have been obtained in ISX, and it is even found that the method makes a significant improvement at moderate densities (2-3 × 10^{13}). We also show quantitatively how it reduces to the more conventional "asymptotic slope" (AS) approach referred to above.

Particular attention is given to the role of neutrals and their spatial distribution in the plasma. This is crucial not only to the interpretation of CX data, but also to the calculation of ion energy losses due to charge exchange, and of plasma formation rates due to ionization of the neutrals. Because CX measurements are toroidally localized, it is necessary to determine the neutral profile shape function in the minor cross section at the location of the analyzer, and desirable to try to relate the local neutral density to the toroidally averaged values seen by the plasma. Almost no measurements of plasma neutrals other than the limited information provided by the charge exchange analyzer itself, and by visible light, which reflects mainly the behavior of the edge neutrals, are available. One therefore relies extensively on calculations; fortunately, these appear to be reasonably accurate. Here we describe a special purpose, two dimensional, neutral density calculation which addresses the problem of toroidally asymmetric neutral sources (gas feeds, limiter, neutral beams) and toroidally localized measurements, in a cylindrical approximation to the torus.

This issue is of unique importance to CX interpretation, because most other neutral-related phenomena, mentioned above, depend only on toroidally averaged concentrations. The conclusion, however, is that while we may depend on more efficient 1D neutrals codes to calculate the local (minor) radial shape function in modeling the CX flux, we cannot reliably extrapolate from the local densities so inferred to determine global averages. The calculations suggest that local measurements underestimate the average neutral density by factors of ten or more; however, the toroidal asymmetries have little impact on CX ion temperature determinations.

4.1 CALCULATION OF NEUTRAL FLUX DENSITY FROM DATA

The CX data are recorded as counts in various time intervals and at several energies, for each mass species. In order to factor out the properties of the analyzer and viewing apertures, we calculate from these data a more meaningful quantity, the neutral flux density $\Phi(E)$, defined as the number of neutrals emitted through the vessel aperture along the viewing chord, per unit area, unit solid angle, unit energy, and unit time. The most practical units to use in this case are particles/cm^2/sr/eV/s. For the i-th channel, the flux density is calculated from the number of counts N_i registered in a time interval δt by the formula given in Equation 4.1.

$$\Phi_i = \Phi(E_i) = \frac{N_i}{\eta_i \dfrac{A_1 A_2}{\ell_{12}^2} (\delta E)_i \delta t} \qquad 4.1$$

Here E_i, (δE_i), and $\eta_i(E_i)$ are the energy, energy dispersion, and detection efficiency, respectively, of the i-th channel, which are obtained from the analyzer field settings and the calibration data. The geometrical quantities A_1, A_2, and ℓ_{12} are defined in Fig. 3-16. Although the data are accumulated and stored in 1 or 2 ms "microintervals", it is common, in data analysis, to sum counts over several consecutive microintervals, and also over two or more nominally identical shots taken with the same analyzer settings. Thus δt is the total combined time taken to accumulate the N_i counts. In principle a seven-point flux spectrum for one mass species may be obtained from a single shot. But since most ISX experiments involve series of about 6–30 identical shots, it is usual practice to construct detailed composite spectra of up to 50 points by detecting different sets of seven energies in different shots, in such experiments.

Next we consider some of the sources of experimental error in measuring the flux densities. The most obvious is that due to counting statistics, whose contribution to the variance of N, σ_N^2, is N itself. This corresponds to a contribution to the variance of Φ, σ_Φ^2, of Φ^2/N. Other sources of error are shot-to-shot irreproducibility and inaccuracies in the various calibration parameters. We estimate the combined total of such errors to be of order 10 per cent, thereby making a contribution $(0.1 \times \Phi)^2 = \Phi^2/100$

to the variance of Φ; thus the total variance in Φ and $\ell n\Phi$ due to random experimental errors are expressed by Equations 4.2 and 4.3.

$$\sigma_{\Phi}^2 = \Phi^2(\frac{1}{N} + \frac{1}{100}) \quad 4.2$$

$$\sigma_{\ell n\Phi}^2 \cong (\frac{1}{N} + \frac{1}{100}) \quad 4.3$$

where the latter is subject to the assumption that N>>1.

It should be noted, in connection with this discussion of errors, that the above types of errors, including statistical errors, make insignificant (<5%, typically in ISX) contributions to the uncertainties in inferred plasma parameters. This is because the ion temperature are logarithmically insensitive to variations in the data points, and because the analyses are based on spectra of at least five, and often more, points. This reduces the sensitivity of the inferred parameters to any one data point. Stated another way, the random errors in a large number of data points tend to cancel one another. It will later be seen that imperfections in the neutral emission modeling are a more important source of error.

4.2 CALCULATION OF FLUX DENSITY SPECTRA FROM PLASMA PARAMETERS

We now suppose that we have obtained, from either a single shot or a composite of several shots, a neutral flux density spectrum $\Phi_i = \Phi(E_i)$ at N energies $E_1,\ldots E_i,\ldots E_N$. We then require an analytic expression for $\Phi(E)$ which contains a parametric dependence on the ion temperature and neutral density, including their respective profiles. We then solve for the desired parameters by fitting the analytic spectrum to the measured spectrum. Let the calculated flux be expressed by $\Phi(E_i;P_1 \ldots P_k \ldots P_M)$ where, for generality, we have assumed M (<N) arbitrary parameters P_k. We solve for the P_k by minimizing the sum of the weighted squared errors, given by Equation 4.4, with respect to each.

$$\varepsilon^2 = \sum_i W_i [\ell n\Phi_i - \ell n\Phi(E_i;P_k)]^2 \qquad 4.4$$

The weighting functions W_i which are used are the $(\sigma^2_{\ell n\Phi})^{-1}$ This generalized form is applicable to cases where multi-chord spectra are available by simply regarding the chord specification as an argument of Φ, on the same footing, mathematically, as E, and allowing one or more of the parameters P_k to characterize the T_i profile.

We now proceed to derive the analytic form for Φ to be used in Eq. 4.4. Neutrals of a given velocity $\underset{\sim}{v}$ (cm-s^{-1}) are produced in the plasma primarily by resonant charge exchange between neutral atoms and ions of that velocity. To a lesser extent, neutrals are also produced by ion-impurity charge exchange and by ion-electron recombination. The importance of the former increases with ion energy, the latter with density. Once born, neutrals either escape from the discharge or are reionized by electron impact, by proton (deuteron) impact, or by charge exchange with ions, before they reach the edge. For simplicity, and because it will be adequate for most of the work done on ISX to date, we assume the plasma to be of circular cross section with minor radius a, and poloidally symmetric, so that all profiles are functions of the local minor radius r. We can then write a general equation for the neutral flux distribution function at the edge of the plasma, $\Gamma_o(a,\underset{\sim}{v})$, expressed in Equation 4.5 in units of s^2-cm^{-5}

$$\Gamma_o(a,\underset{\sim}{v}) = n_o(a)\underset{\sim}{v}f_o(a,\underset{\sim}{v}) = \int_{chord} dsR(s,\underset{\sim}{v})n_i(s)f_i(s,\underset{\sim}{v})P(s,\underset{\sim}{v}) \qquad 4.5$$

where

$n_o(a)$ and $f_o(a,\underset{\sim}{v})$ are the edge neutral density (cm^{-3}) and velocity distribution function (s^3-cm^{-3}) respectively.

s is arc length (cm) along a chord which passes through the aperture where Γ_o is being evaluated, and is in the direction of $\underset{\sim}{v}$.

$n_i(s)$ and $f_i(s,\underset{\sim}{v})$ are the local ion density and velocity distribution function, respectively, at the position s on the chord.

$R(s,\underset{\sim}{v})$ is the local neutral birth rate (s^{-1}) per ion.

$P(s,\underset{\sim}{v})$ is the escape probability for neutrals born at s and having velocity v.

In measurements, the energy and mass of the ions and neutrals are those selected by the analyzer. Moreover, the velocity direction $\underset{\sim}{v}/v$ is fixed by the orientation of the viewing column, so the detected flux is simply a function of speed v or, more conveniently, of the energy E. In view of this, we can relate Γ_o to the measured quantity Φ by

$$\Phi = \frac{1}{2} E^{0.5} \left(\frac{K}{A}\right)^{1.5} \Gamma_o \qquad 4.6$$

in which energy is expressed in eV, A is the selected ion mass in amu, and K is defined such that $v = \sqrt{KE/A}$, so $K = 1.93 \times 10^{12}$ $cm^2\text{-}s^{-2}\text{-}eV^{-1}$.

Next we write expressions for the quantities appearing in the integrand of Eq. 4.5. These quantities retain their above dimensions, but we now substitute the energy argument for velocity. For the neutral production rate, we have

$$R(s,E) = n_o(s)\sigma_{cx}(E)\left(\frac{KE}{A}\right)^{0.5} + n_e(s)\alpha_r[T_e(s)] \qquad 4.7a$$

where the first term is due to charge exchange and the second, anticipating the possibility of sufficiently dense plasmas, to recombination.[50] Assuming the ion temperature to be locally Maxwellian, we obtain

$$f_i(s,E) = \left(\frac{A}{\pi K T_i(s)}\right)^{1.5} \exp[-E/T_i(s)] \qquad 4.7b$$

and finally the attenuation, or escape probability, can be expressed

$$P(s,E) = \exp\left[- \int_s^{edge} ds' \left(\frac{1}{\lambda_i}\right)\right] \qquad 4.7c$$

where

$$\frac{1}{\lambda_i} = n_i(s')\sigma_{cx}(E) + n_e(s')\left(\frac{A}{KE}\right)^{0.5}\alpha[T_e(s')] + n_i(s')\sigma_{ip}(E) \qquad 4.7d$$

The three terms in the attenuation integral (Eq. 4.7c) arise, respectively, from charge exchange, electron ionization, and proton ionization. They are written in order of their importance at typical thermal energies in ISX. The cross sections (in cm^2) σ_{cx} in Eq. 4.7a and σ_{cx} and σ_{ip} in 4.7d may be evaluated at the energy E, since E is generally much greater than the local neutral or ion temperature. The recombination (α_r) and ionization (α_i) rates (in s^{-1}) are averages over the electron velocity distribution and therefore depend only on the local electron temperature, $T_e(s)$.

Finally we combine Eqs. 4.5, 4.6, and 4.7 to obtain the desired expression for $\Phi(E)$ to be used in minimizing ε^2. For convenience, we express the density and ion temperature profiles as products of their central values and their shape functions; for example $n_o(s) = n_{oo}\tilde{n}_o(s)$, where $n_{oo} \equiv n_o(0)$ and $\tilde{n}_o(0) \equiv 1$, s = 0 being defined as the point on the chord where the minor radius is minimum. The flux equation, expressed in practical units, thus assumes the form

$$\Phi(E) = 1.25 \times 10^5\left(\frac{n_{io}}{A^{0.5}T_{io}^{1.5}}\right)\sigma_{cx}(E)E$$

$$\times \int_{\text{chord}} \frac{\tilde{n}_i(s)}{[\tilde{T}_i(s)]^{1.5}} \left\{ n_{oo}\tilde{n}_o(s) + \frac{n_e(s)\alpha_r[T_e(s)]A^{0.5}}{\sigma_{cx}(E)K^{0.5}E} \right\} P(s,E)\exp[-E/T_i(s)] \qquad 4.8$$

This contains the desired parametric dependence on the central neutral density n_{oo} and ion temperature T_{io}, and also on the T_i profile, $\tilde{T}_i(s)$. Before discussing the solution of Eq. 4.4 using Eq. 4.8, we digress to show how Eq. 4.8 can be approximated to give the central ion temperature directly, using the conventional AS method.

4.3 ASYMPTOTIC SLOPE (AS) ANALYSIS METHOD

The basic assumption of the AS analysis method is that the asymptotic (i.e. $E \gg T_{io}$) neutral spectrum, with appropriate energy-dependent corrections, represents the central ion distribution function. In this section, we examine this assumption quantitatively by evaluating Eq. 4.8 in the asymptotic limit; we find, as was observed on ORMAK,[26] that the central distribution is well-represented only if the asymptotic condition $E \gg T_{io}$ is strongly satisfied. Otherwise, the temperature obtained by this method tends to underestimate the true central temperature to a significant degree.

In the limit $E/T_{io} \to \infty$, the spatial dependence of the integrand in Eq. 4.8 is dominated by that of the exponential, which is maximum, by assumption, at s = 0. Assuming $\tilde{T}_i(s) \sim 1-k(\frac{s}{a})^2$ near s = 0, then

$$\lim_{E/T_{io}\to\infty} \left\{\exp[-E/T_i(s)]\right\} = a\left(\frac{\pi T_{io}}{kE}\right)^{0.5} \exp[-E/T_{io}]\delta(s) \qquad 4.9$$

This expression, upon substitution in Eq. 4.8, leads to an asymptotic expression for $\Phi(E)$, namely

$$\lim_{E/T_{io}\to\infty} \Phi(E) = 2.22 \times 10^5\left(\frac{n_{oo}n_{io}a}{A^{0.5}k^{0.5}T_{io}}\right)\sigma_{cx}(E)E^{0.5}P(0,E)\exp[-E/T_{io}] \qquad 4.10$$

To obtain the temperature, we define the corrected spectrum to be

$$\hat{\Phi}(E) = \frac{\Phi(E)}{\sigma_{cx}(E)E^{0.5}P(0,E)} \qquad 4.11$$

using Eq. 4.7c to calculate P. Finally, we fit a straight line to the logarithm of the measured spectrum, also corrected as above, versus energy. Then T_{io} and n_{oo} are obtained from the slope and intercept of the line, by identification with Eq. 4.10, using formulas 4.12.

$$T_{io} = -\left[\frac{d}{dE}\,\ln\,\hat{\Phi}(E)\right]^{-1} \qquad 4.12a$$

$$n_{oo} = \frac{A^{0.5} k^{0.5} T_{io}}{2.22 \times 10^5 \, n_{io} a} \, \Phi(0) \qquad 4.12b$$

The validity of the asymptotic approximation is based on the Maxwellian exponential's dominating the spatial dependence in the integrand of Eq.4.8. The next strongest dependence, in the asymptotic limit, is that of the neutral density profile n_{oo}, which, as will later be shown, may vary by a factor of 10^2–10^4 or more from the edge to the center, depending mainly upon the density. To estimate the energy above which the exponential dominates, we first express the neutral density profile in a form which roughly simulates those obtained from neutral transport codes[52,53] in Eq. 4.13,

$$\tilde{n}_o(s) = \exp \left\{ \left(\frac{s}{a}\right)^2 \ell n \left[\frac{n_o(a)}{n_o(0)}\right] \right\} \qquad 4.13$$

where it is assumed that the chord passes through the center. For the assumed ion temperature profile, $\tilde{T}_i(s) \sim 1-k\left(\frac{s}{a}\right)^2$, the requirement for asymptotic behavior becomes, approximately,

$$\frac{E}{T_{io}} > \frac{1}{k} \ell n \left[\frac{n_o(a)}{n_o(0)}\right] \sim 5\text{–}7 \qquad 4.14$$

in ISX. Physically, this implies that the neutral profile tends to weight the flux contributions toward the edge of the plasma, and the ion temperature profile toward the center. The asymptotic requirement must be strongly satisfied for the former to overcome the latter. The difficulty is that data far out on the tail of the distribution may be poor in quality or non-existent. In some cases, the Maxwellian distribution may become distorted there, hence the local slope would not represent the temperature. For these reasons, and in order to make use of data over a wider range of energies, we use the MF method described in the next section. However, it is obvious from the preceding discussion that it is still desirable to measure as high in energy as possible, so that the central spectrum is well-represented. The AS method is still useful, moreover, as a straightforward, non-iterative procedure which can be used to make preliminary temperature estimates, for example, in on-line analyses, where computational speed and power are limited.

4.4 MODEL FIT (MF) ANALYSIS METHOD

In order to better account for profile effects and neutral attenuation and to relax, somewhat, the asymptotic requirement on the usable energy range, Eq. 4.8 may itself be used directly as Φ in Eq. 4.4. The electron temperature and density profiles needed to evaluate this may be obtained from laser Thomson scattering measurements. In plasmas where either H or D, but not both, are present, the ion density may be taken to be a constant fraction of the electron density. It is conventional, and sufficiently accurate in the absence of more detailed impurity profiles to calculate this proton or deuteron deficiency using formula 4.15.

$$\frac{n_i}{n_e} = \frac{Z_o - Z_{eff}}{Z_o - 1} \qquad 4.15$$

where Z_{eff}, the average ionic charge for momentum transfer, is determined from the plasma resistance and assumed to be spatially constant, and Z_o, the charge state of the dominant impurity species, is determined spectroscopically. In most experiments done to date on ISX, Z_{eff} has been 2.5 or less, and Z_o ranges from 8 (oxygen) to 26 (iron), so n_i/n_e is generally 0.8 or greater. In mixed plasmas (H and D both present in significant fractions), the above arguments apply if n_i is taken to be the sum of the proton and deuteron densities. No estimates of their ratios in the plasma core are available except to the extent that CX analysis can provide them.

Next we consider the neutral density profile. As has already been seen in connection with the AS procedure, the spatial localization of the CX measurement depends strongly on the shape of this profile. Because of the lack of unambiguous experimental information on the neutral profile near the center of the plasma, we are forced to calculate it by solving the relevant Boltzmann transport equation,[51] Eq. 4.16.

$$\nabla \cdot n_o(\underset{\sim}{r})\underset{\sim}{v}\, f_o(\underset{\sim}{r},\underset{\sim}{v}) + n_o(\underset{\sim}{r}) f_o(\underset{\sim}{r},\underset{\sim}{v}) \{ n_e(\underset{\sim}{r}) \alpha_i [T_e(\underset{\sim}{r})]$$

$$+n_i(\underset{\sim}{r})<(\sigma_{cx} + \sigma_{ip})|\underset{\sim}{v} - \underset{\sim}{v}_i|>\} =$$

$$n_o(\underset{\sim}{r})n_i(\underset{\sim}{r})f_i(\underset{\sim}{r},\underset{\sim}{v})<\sigma_{cx} \quad |\underset{\sim}{v} - \underset{\sim}{v}_o| \quad > + S_o(\underset{\sim}{r},\underset{\sim}{v}) \qquad 4.16$$

Typical source terms which can be included in S_o are:

1) Franck-Condon neutrals resulting from dissociation of molecular hydrogen introduced by gas feed at the vacuum wall.

2) Neutral gas desorbed from the limiter due to recombination of ions and electrons there.

3) Thermal neutrals resulting from charge exchange trapping of injected beam neutrals by plasma ions.

4) Thermal neutrals resulting from bulk recombination of plasma ions and electrons.

5) Wall-reflected neutrals

6) Cold neutrals resulting from pellet ablation

The reliabilty of this calculation is probably quite high, because it is linear, the neutral trajectories are straight lines, and the atomic physics is reasonably simple. Moreover, a number of codes which solve Eq. 4.16, written by independent workers, are in substantial agreement with one another.[52,53] The major uncertainty is undoubtedly how to specify the boundary conditions (e.g. velocity-dependent wall reflections, recycling, effects of operating history and gettering), but the choice turns out to have little effect on the shape of the profile near the center.

Because Eq. 4.16 is linear, one can superpose solutions for each of the separate source terms, except for (5), which is generally included as a boundary condition. In the data analysis, existing one-dimensional codes,[52,53] which solve the equation in either a cylindrical or slab approximation, were used. The component of the neutral density due to edge neutrals is determined only within a multiplicative constant, which is left as a free parameter (effectively, the central neutral density n_{oo}), to be determined by the best fit to the CX data. No such freedom is given the recombination neutrals, however, since the source rate is a well-defined function of the density. In the following section, we describe a two-dimensional, cylindrical Monte Carlo solution to Eq. 4.16 which was developed by the author to check the validity of using 1D models and of neglecting sources, such as 2), 3), and 6), when they are toroidally remote from the CX analyzer.

The remaining inputs to Eq. 4.8 are those quantities which are to be determined: the central ion temperature, central neutral density (or the edge neutral source rate), and the T_i profile shape function. The latter can be modeled by the parametric function $\tilde{T}_i(r) = [1-(\frac{r}{a})^{p_1}]^{p_2}$, and if off-axis CX data were available, p_1 and/or p_2 could be included as fitting parameters. In principle, profile information is contained, through the energy dependence, in single chord data, but not with sufficiently strong dependence to extract it reliably. So in the absence of off-axis chords we are forced to assume a profile shape, and we use the profile parameters to check the sensitivity of the inferred central temperature and neutral density to the assumed profile. Normally, we choose a parabolic ($p_1 = 2$, $p_2 = 1$) as the "nominal" profile, and calculate error bars on T_{io} and n_{oo} by using more peaked ($p_1 = 1.5$) and more broad ($p_1 = 4$) functions for the assumed shape.

4.5 NEUTRAL DENSITY CALCULATIONS

In the previous sections, the sensitivity of the CX data, and analysis thereof, to the neutral density profile has been repeatedly emphasized. It was pointed out that the profile shape function must be somehow known a priori, in order to properly evaluate the relative CX flux contributions from different spatial layers in the plasma. Owing to the linearity of the neutral Boltzmann equation, the magnitude of the profile, in effect the central neutral density, may still be left as a free parameter to be determined by best fit to the measured CX flux.

A consistent result obtained from ISX CX data in this manner is that the inferred neutral densities appear unexpectedly low; central values are in the range 10^6-10^8 cm^{-3} in D^+ plasmas, where values about an order of magnitude greater were expected. The expectations were based on experience in other tokamaks [10^8-10^9 is given as a typical range in reference (25)] and on certain information, albeit inconclusive in itself, which renders the low inferred values suspicious. We discuss this next.

In power balance calculations performed to model both ohmic and neutral beam heating experiments in ISX, the results of which will be given in subsequent chapters, charge exchange and heat conduction are the principal ion energy loss processes. At high densities $n_e \geq 3.5 \times 10^{13}$ cm^{-3}), the former is found to be negligible compared to the latter, based on the neoclassical theory, even if neutral densities ten times greater than the measured values are used. Hence, in this regime, the calculated ion temperature is determined by a balance between power transferred from electrons and beams and heat conduction losses; moreover, the measured temperatures are reproduced if neoclassical coefficients are used for the latter. At low densities, the role of charge exchange is presumably more important, because conduction losses decrease with decreasing density and because neutrals are more likely to penetrate to the hot region of the plasma. Here the transport calculations reproduce the measured ion temperature only by 1) assuming neutral densities to be at least ten times greater than those inferred by CX analysis, or 2) invoking anomalous (i.e. non-neoclassical) ion heat conduction. Since neoclassical ion transport is on rather sound footing, a general conclusion of most ohmic and beam-heated tokamaks, including ISX, the tendency is to at least question the CX-based neutral density estimates.

With these suspicions in mind, we must reconsider the validity of neutral density measurements based on CX flux. We estimate that alignment errors, calibration uncertainties, and inadequate reproducibility of gas cell conditions might conceivably produce an error of × 2 in measured neutral flux, not enough to account for the observed discrepancies. It seems more likely that the resolution is found in the physics of neutral transport itself, which suggests that plasma neutrals are localized about their sources, unlike charged particles, which distribute themselves along field lines. Thus, any measurement of neutral density would yield at best only a local value, which could be much greater or much less, depending upon the proximity to gas sources, than the average values relevant to computation of charge exchange losses. In the case of the ISX-B CX diagnostic, the nearest source is a gas feed valve about 100 cm away. Calculations to be described below, as well as experiments performed an PULSATOR, roughly indicate that this distance is enough to make the measured neutral density lower than the toroidal average by the required amount. This being the case, we might ask whether the neutral profile shape functions calculated using the 1D models give the correct form at the toroidal location of the analyzer, since this is crucial to the neutral emission modeling. This question was investigated, with the gratifying result that, in fact, the profile in the minor cross section appears to be invariant in shape with respect to toroidal position, even though the magnitude may be attenuated rapidly.

A Monte Carlo particle-following code NEUT2D has been developed to calculate the neutral density in a straight cylindrical plasma column, where electron and ion densities and temperatures are functions of radius only, subject to radially dependent, azimuthally symmetric neutral sources in a plane located at z = 0.* In the axially symmetric cylinder, this can be generalized, by convolution, to arbitrary sources of the form $S_0(r,z)$. We assume that the neglect of toroidal curvature is unimportant, since axial e-folding lengths turn out to be much less than the major circumference of the machine. The objective in performing this calculation was not to provide a new neutral transport code for general use, since many exist and the Monte Carlo technique is inefficient for this application. Instead the purpose was to investigate specifically the aforementioned problems associated with interpretation of CX data: toroidal dependence of the neutral density and neutral density profile. The existence of even large toroidal variations is not important for transport and power balance calculations, since the plasma samples the entire major circumference and, its charge exchange losses thus depend upon the toroidally averaged neutral density at each minor radius, which the 1D codes calculate correctly. The Monte Carlo method was chosen for this investigation because it can easily be made to incorporate physical behavior which would otherwise be intractable.

---

*This is a simplified attack on a problem addressed in considerably greater detail (e.g., using 3D toroidal geometry and point sources) by G. G. Kelley a few years ago. The conclusions reported here are essentially the same as Kelley's.[54]

The procedure used is to simply follow the entire life history of each of a large number of particles. During its life, a particle makes contributions to the neutral density in a given volume element in proportion to the amount of time it spends there. Neutrals originate either at the wall of the vessel or in the plasma volume. In the former case, they are assigned a Franck-Condon dissociation energy of 5 eV, and a direction chosen at random according to a cosine distribution about the normal direction. In the latter instance a neutral is assumed to have been born as a result of electron-ion recombination or by charge exchange of a thermal ion with a beam neutral (which itself is of a special class of neutrals not considered in this problem). In either of these, the new neutral has a velocity assigned at random from the local ion (Maxwellian) velocity distribution.

Neutrals follow linear trajectories which are interrupted only by charge exchange, ionization, or wall impact. The first two processes occur at random path intervals according to their respective local mean free paths, computed from the plasma parameters and cross sections. In a charge exchange the neutral, in effect, assumes the velocity of a random member of the local ion distribution and its trajectory continues with the new speed and direction. In the case of ionization, the neutral dies and no further accounting is made. Wall encounters are treated using a crude reflection model: the particle dies with a specified constant probability, and a survivor is reflected with energy between zero and the incident energy, with uniform probability, and direction chosen according to a cosine law. While this model is certainly subject to considerable refinement, it embodies the essential physics necessary to resolve the issues in question.

In order to check the calculation, it was compared with results from one of the existing 1D codes, NEUCG, due to Burrell,[52] which solves the problem in similar geometry, but assumes axially uniform source distributions. Since NEUT2D effectively computes an axial Green's function, the 1D result can be reproduced by a convolution of the 2D result with a uniform source for comparison with Burrell's solution. If the problem is solved in a test cylinder extending from $z = -L$ to $z = +L$ (where L is large enough that end effects are unimportant), this relationship may be expressed by Eq. 4.17.

$$n_{1D}(r) = \frac{1}{2L} \int_{-L}^{L} d\zeta \; n_{2D}(r, z-\zeta) \equiv \frac{1}{2L} \int_{-L}^{L} d\zeta \, n_{2D}(r,\zeta) \qquad 4.17$$

The plasma is represented in these calculations by electron and ion density and temperature profiles which assume peak values at $r = 0$ and diminish parabolically to some small (though non-zero) value at $r = a_p$. The ions and neutrals are taken to be deuterium in all cases. The vessel wall is located at $r = a_w \geq a_p$; if $a_w > a_p$, the profiles retain their edge values between $r = a_p$ and $r = a_w$.

4.5.1 Case I: No Reflection, $a_p = a_w = 27$ cm

This case was considered primarily to make the comparison with NEUCG. Reflection is neglected because NEUCG reflects particles with the Franck-Condon energy rather than with energies related to the incident energy. Similarly, $a_p = a_w$ was used because of the inapplicability of NEUCG to profiles with discontinuities.

The dynamics of the problem may be visualized with the aid of Fig. 4-1, which shows the trajectories of 30 test particles in (r,z) space. The particles are launched at (27.0,0+); symmetry is enforced by specularly reflecting particles which cross the plane $z = 0$, effectively interchanging them with "image" particles assumed to have been launched at $z = 0$. Encounter-free trajectory segments are hyperbolic in this space, charge exchange results in an abrupt change in direction, and death, either by ionization or by wall absorption, is indicated by an asterisk (*).

The physical edge source strength was taken to be 10^{20} s^{-1} for a test cylinder of length $2L = 200$ cm; the equivalent uniform source used in NEUCG is $10^{20}/(2\pi a_w \times 2L) = 2.95 \times 10^{15}$ cm^{-2}-s^{-1}. This corresponds to a total particle feed rate of $\sim 3 \times 10^{20}$ s^{-1} = 5 torr-ℓ/s (molecular) in ISX. Comparing the axially averaged results with those of NEUCG, good agreement is obtained both for $n_e(0) = n_i(0) = 2 \times 10^{13}$ and for 8×10^{13} cm^{-3}. In both cases, $T_i(0)$ was 400 eV and $T_e(0)$ was 1200 eV. These comparisons are shown in Fig. 4-2.

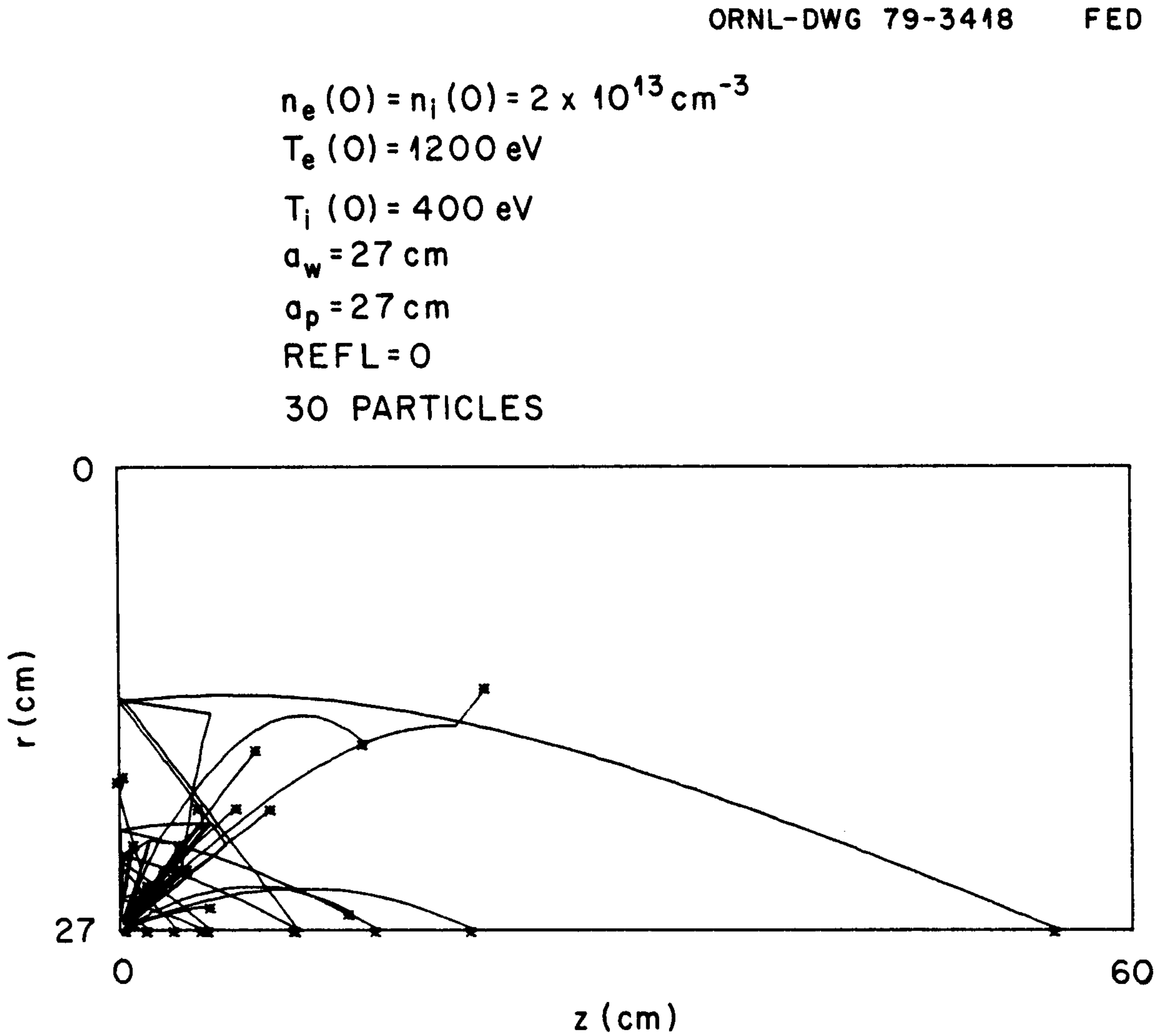

Figure 4-1. Neutral particle trajectories from Monte Carlo neutrals code for a wall source with plasma extending to wall. Uninterrupted paths are hyberbolae; death indicated by an asterisk; charge exchange by a discontinuity. Symmetry about z=0 enforced by reflecting particles which attempt to cross that plane.

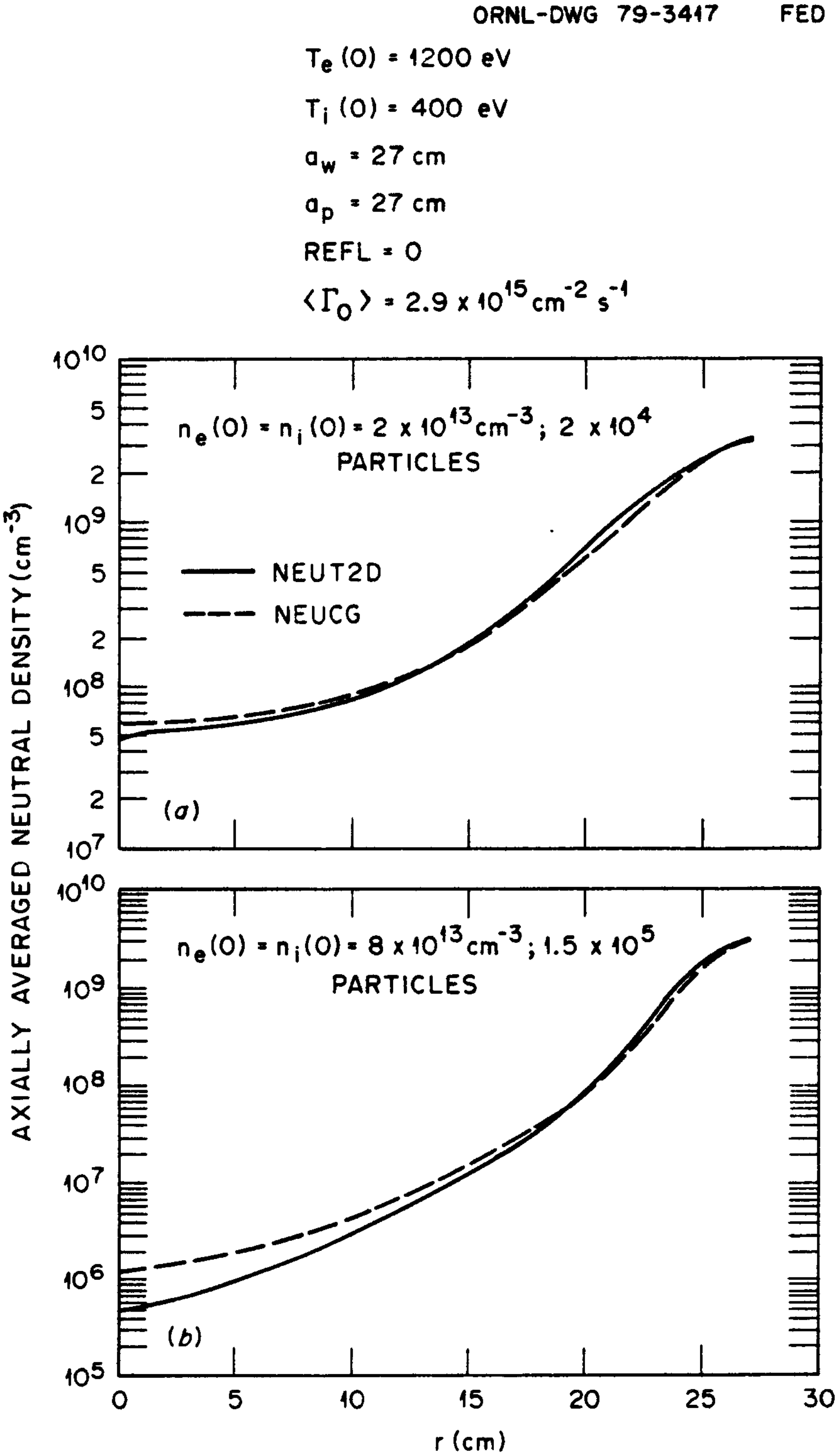

Figure 4-2. Comparison of neutral densities from Monte Carlo code (NEUT2D) and NEUTCG for a wall source. Low (a) and high (b) plasma density cases are compared. NEUT2D results are axially averaged for comparison with 1D results of NEUTCG.

We can also calculate the neutral density due to a volume source, for example, recombination neutrals. For this, a 2D calculation is completely unnecessary, since recombination is by nature a toroidally uniform source; however, we perform such a calculation anyway as another comparison with NEUCG,[55] using the same geometry as described above, with results plotted in Fig. 4-3 for the case $n_e(0) = 8 \times 10^{13}$. Once again the agreement is quite satisfactory.

4.5.2 Case II: 50% Reflection, $a_p = 27$ cm, $a_w = 45$ cm

Having acquired some confidence in the 2D code using Case I, we next consider a somewhat more realistic problem. In ISX, the circular plasma is surrounded by a rectangular cross section stainless steel vessel whose inner dimensions are 69 cm horizontally and 113 cm vertically. Thus the plasma, whose diameter is fixed by limiter bars to be no more than 54 cm, is separated from the wall by at least 7-8 cm. This layer, together with the possibility of wall reflection, increases the average axial displacement of a particle launched from the wall, before it is absorbed by either the plasma or the wall. To see this effect, we again solve the 2D problem with an edge source as in Case I, but taking the wall radius to be 45 cm (the average of the vessel half-height and half-width), leaving an 18 cm plasma-free layer adjacent to the wall, and assigning a wall reflection coefficient of 0.5. Again, we display a few trajectories in Fig 4-4, showing how neutrals can make axial headway in the empty layer, and are thus less clustered about the source.

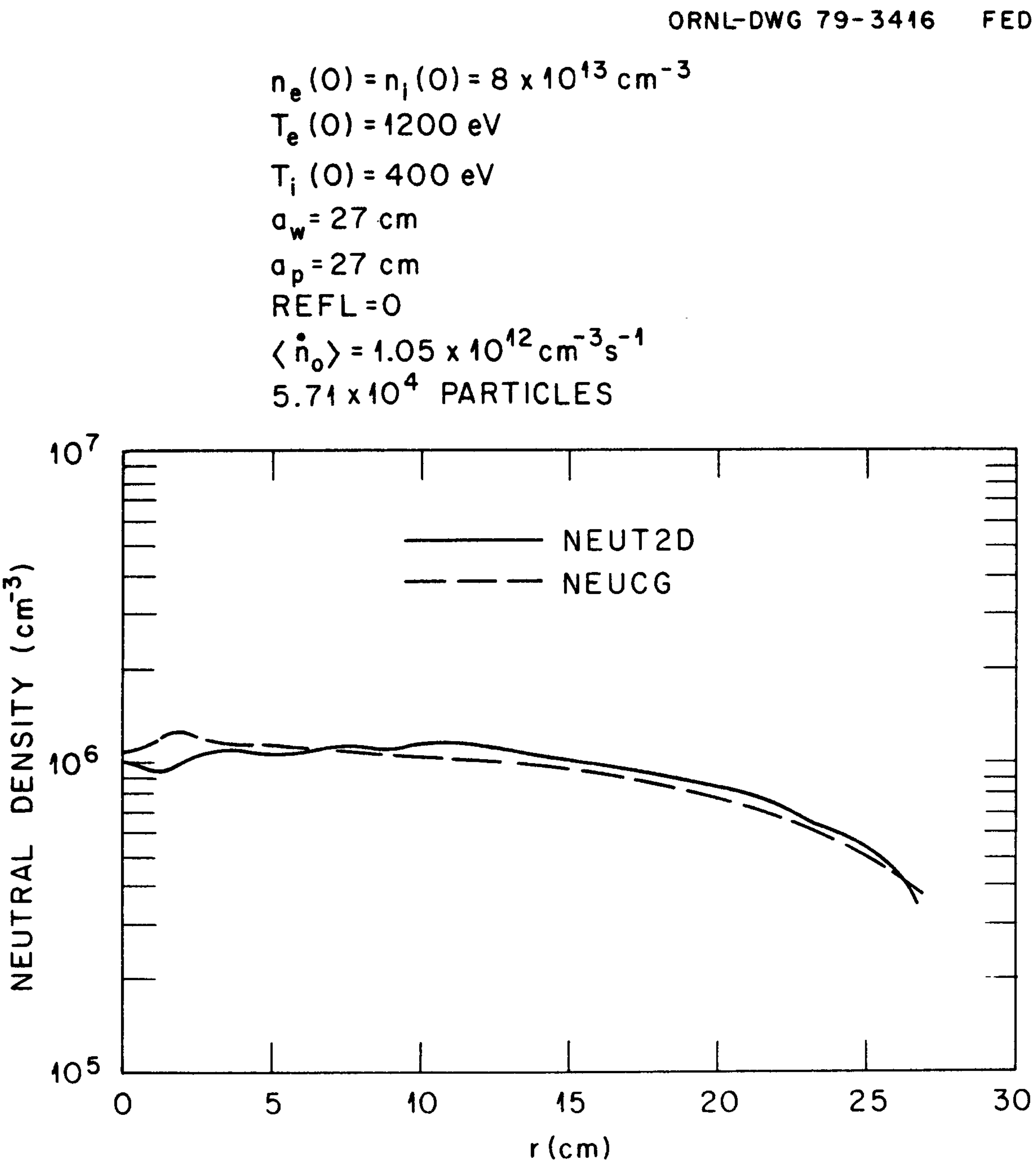

Figure 4-3. Comparison of neutral densities from Monte Carlo code and NEUTCG for volume (recombination) source.

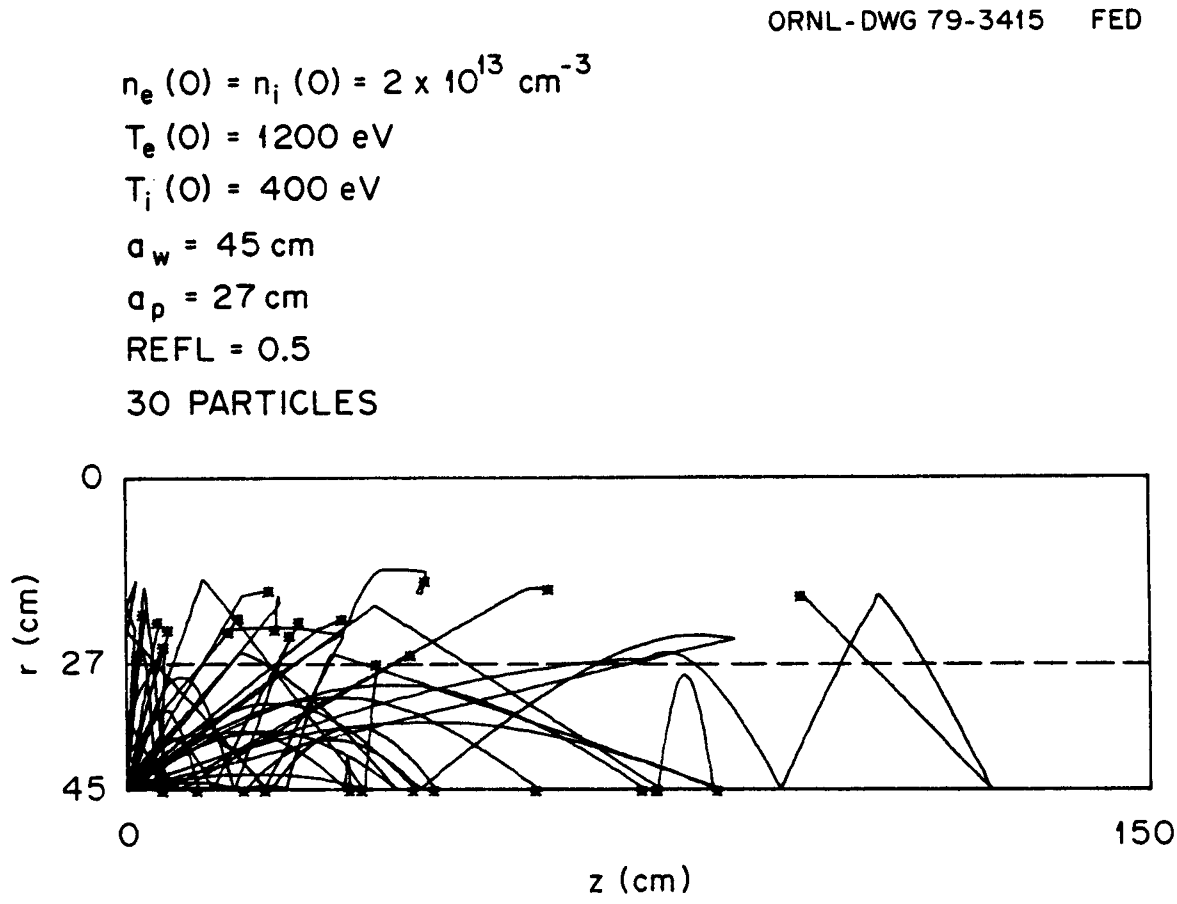

Figure 4-4. Neutral particle trajectories from Monte Carlo neutrals code for a wall source with large empty layer between wall and plasma.

In Figs. 4-5, 4-6, and 4-7, we compare results of these 2D calculations with those of Case I, again for $n_e(0) = 2 \times 10^{13}$ and 8×10^{13}. In Fig. 4-5, we see that the effective 1D $n_o(r)$ profiles are relatively unaffected by the presence of the empty layer and by reflection. However, the axial localization of neutrals is strongly affected by these, as well as by density, as Fig. 4-6 demonstrates; here we display the z dependence of n_o at various radial positions.

Clearly, neutral densities measured tens of centimeters from a gas source are significantly less than either peak or average values, at any radius. The axial localization becomes stronger with increasing density, decreasing reflection, and decreasing empty layer width. However, Fig. 4-7 shows that the radial profile shape factors are fairly invariant with axial position relative to the source. This implies that in analyzing CX data, we can legitimately, and more efficiently, use a 1D code such as NEUCG to calculate the local radial neutral profile.

Another source of neutrals, probably the dominant one, is the limiter. This is due to the recycling of plasma which is intercepted there; for example, if the average plasma density is 5×10^{13} cm^{-3}, the volume of the plasma 2×10^6 cm, the particle confinement time 20 ms, and the recycling coefficient unity, then the resulting neutral source is 5×10^{21} s^{-1}, equivalent to ~100 torr-ℓ/s (molecular). These neutrals are launched at the edge of the plasma, as in Case I, but there can still be an empty layer between wall and plasma, as considered in Case II. We find, however, that despite the empty

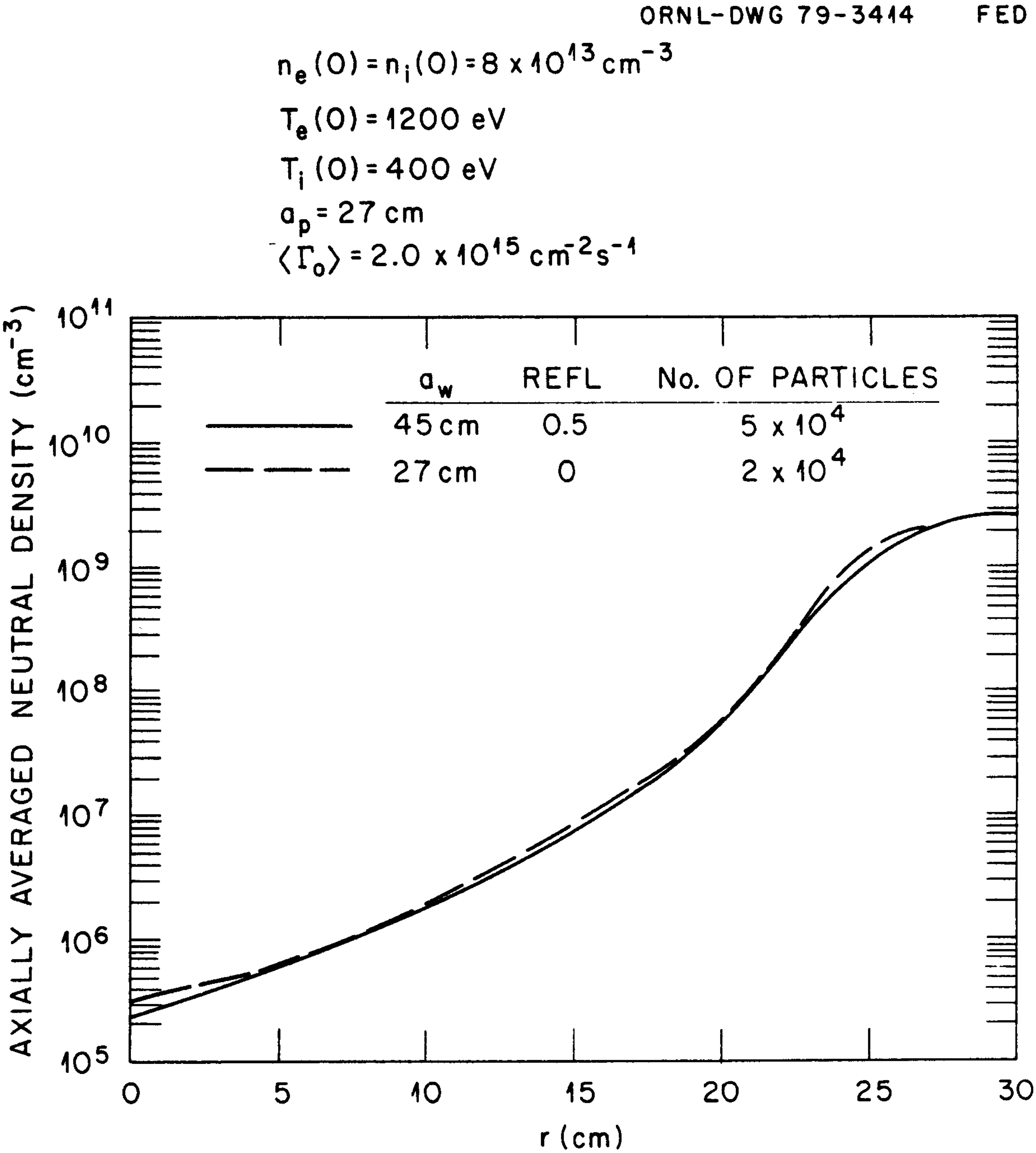

Figure 4-5. Comparison showing independence of axially averaged neutral density on empty layer and reflection.

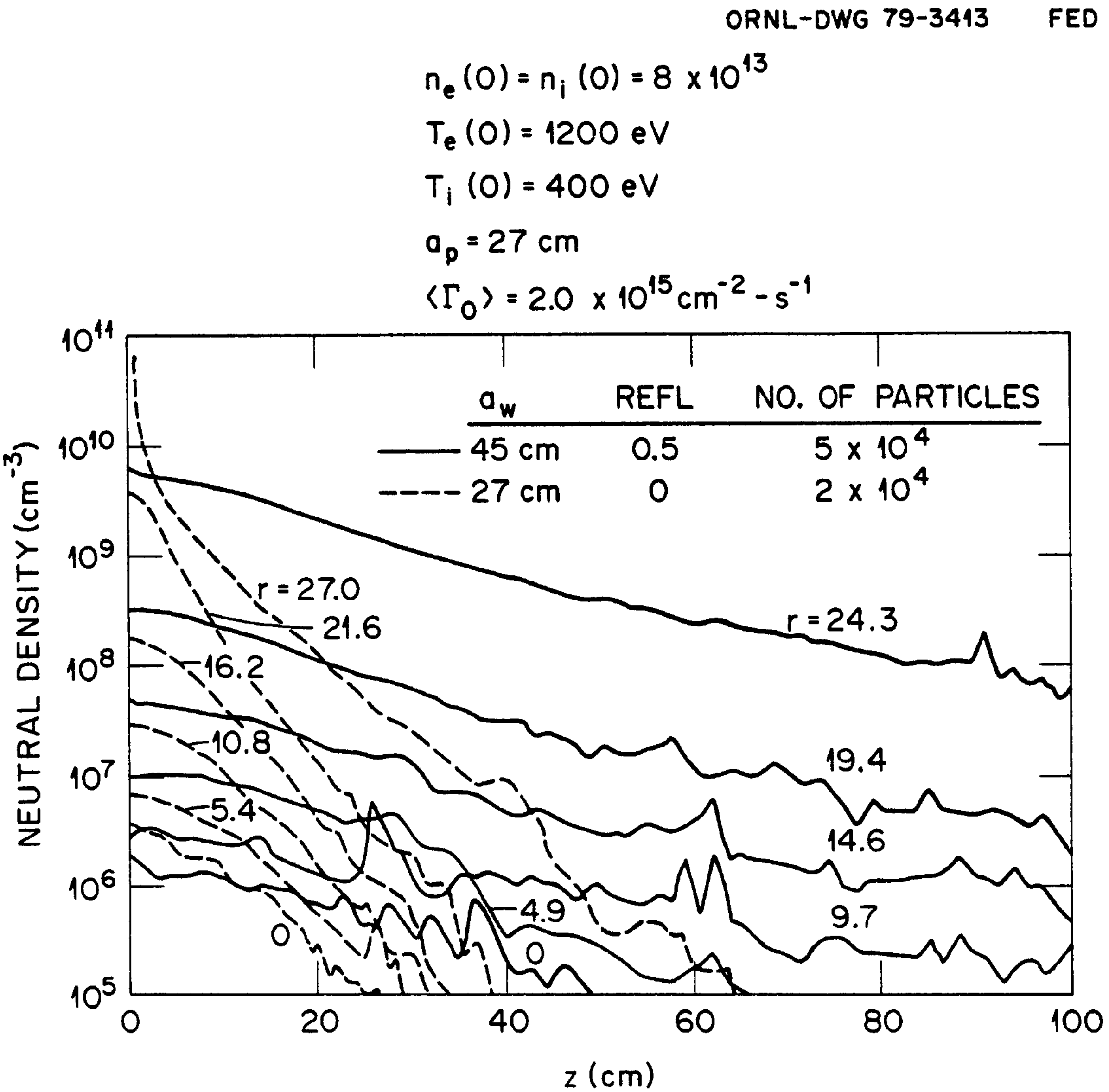

Figure 4-6. Comparison showing dependence of local neutral density on empty layer and reflection. Comparisons are made at several radii.

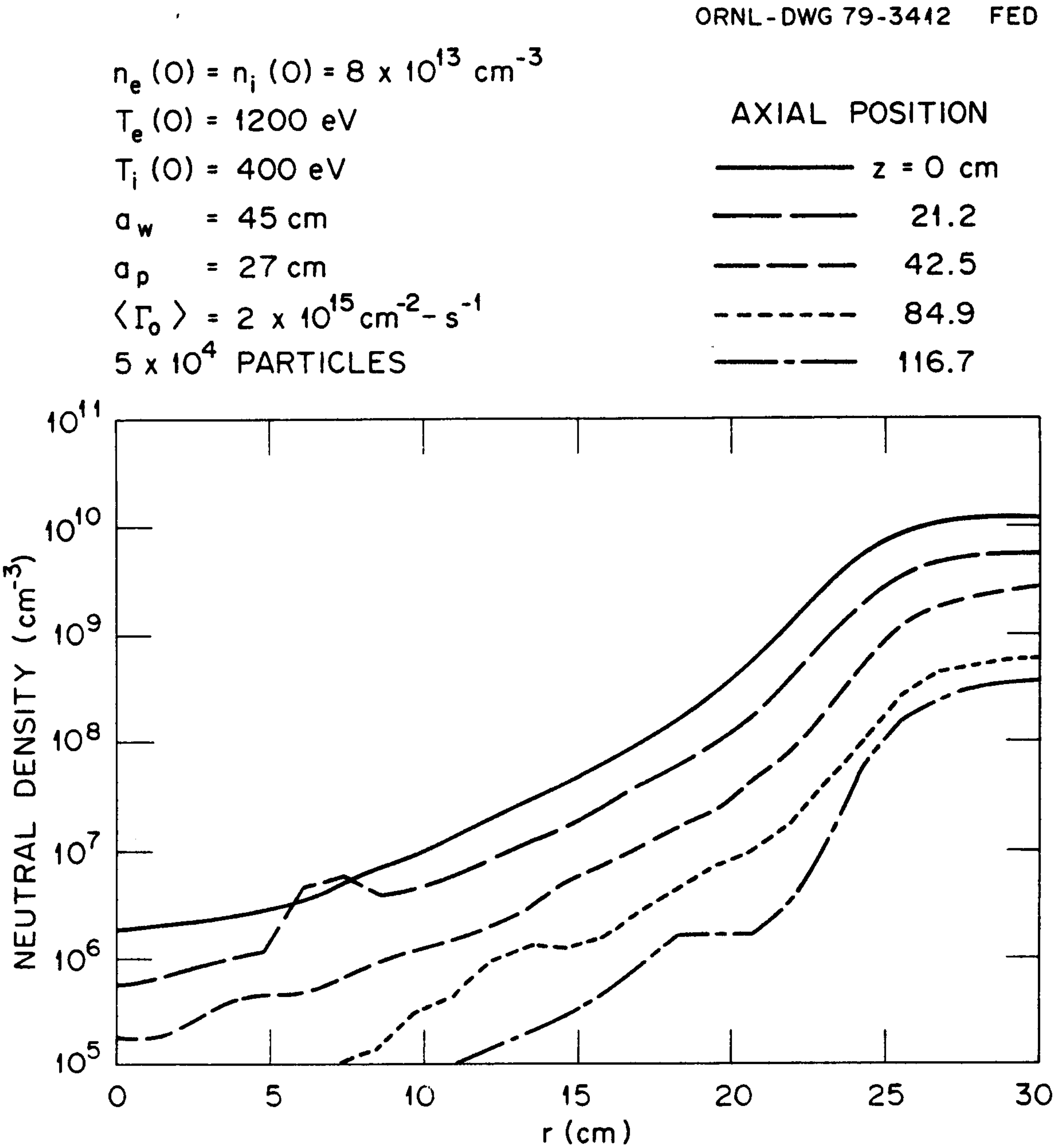

Figure 4-7. Independence of neutral profile shape factor on axial distance from source.

layer, the neutrals are strongly localized, as they were in Case I; this fact is shown in Fig. 4-8. Because the ISX CX system is located toroidally 180 degrees from the limiter, we would expect these neutrals to make no contribution to the measured signal. Nevertheless, they may well make the dominant contribution to the global charge exchange losses.

4.5.3 Conclusions from Neutral Density Calculations

These examples are at best approximate simulations of ISX behavior, because they ignore the details of the rectangular vessel geometry and the poloidal asymmetry inherent in any point source such as a gas valve. For example, the wall is much closer to the plasma on the sides, and farther on the top and bottom, than in the model of Case II. Thus this calculation cannot at this time be used to infer average neutral densities from local measurements. The point to be made is that strong toroidal asymmetries can easily exist.

We conclude from this study that it is incorrect to infer power balance-relevant neutral densities from values measured by CX or any other localized diagnostic. In particular, the ISX-B CX measurements almost surely underestimate the average loss rates by at least an order of magnitude. In light of this, values of 10^6-10^8 cm^{-3} central neutral density measured in ISX are neither unreasonable nor inconsistent with charge exchange losses appropriate to much higher values. Similar conclusions are obtained from calculations and experiments on PLT.[56] Providing edge source neutrals have some axial freedom resulting from an empty layer between wall and plasma,

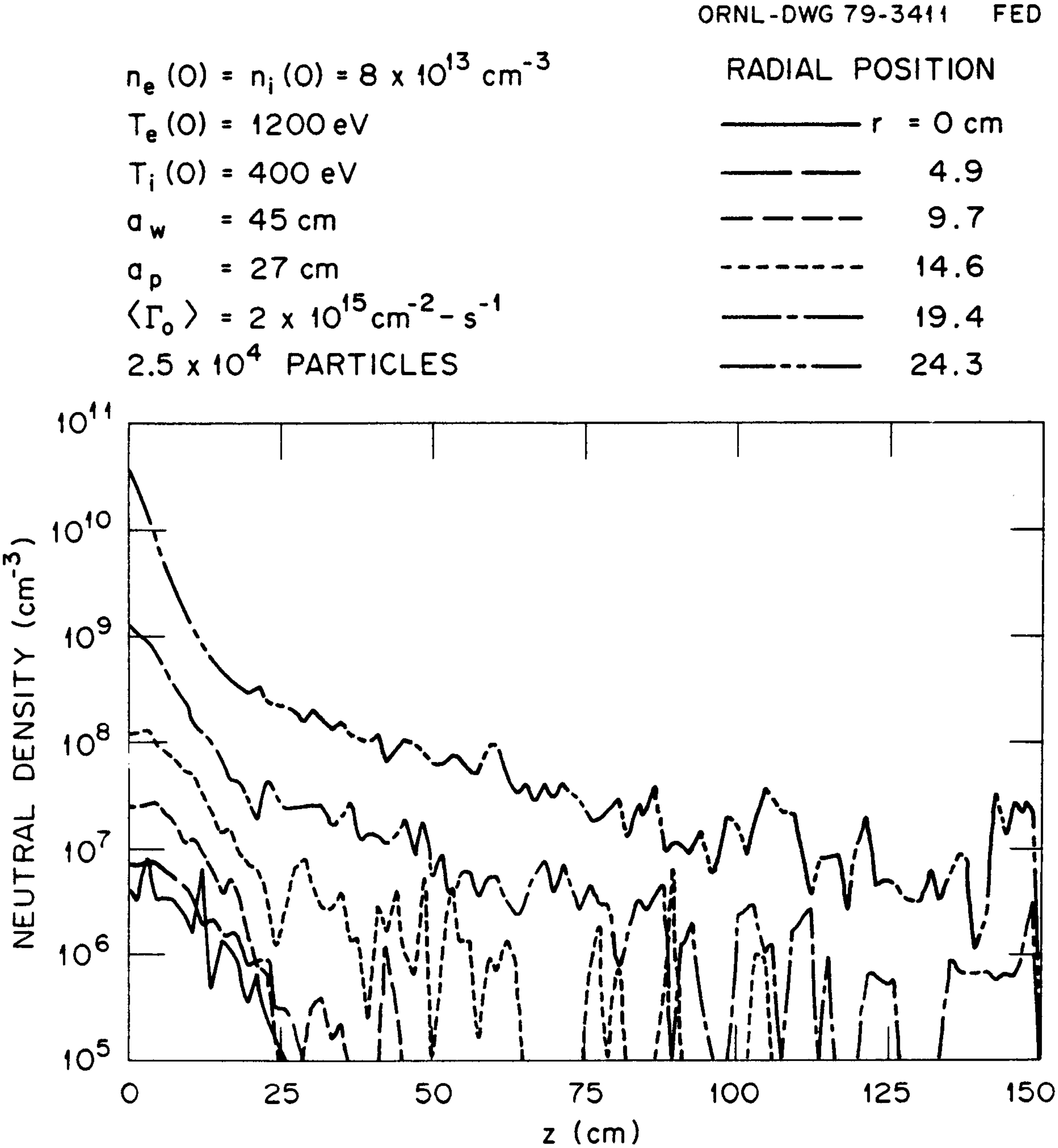

Figure 4-8. Axial neutral density profiles showing strong localization about a limiter-type source. Limiter is located at plasma edge, but there is an empty layer between plasma and wall.

as was considered in Case II, their radial profile shape functions are well described by the 1D code results, while the local magnitude is taken from the measurement itself. Furthermore, recombination should also be included as a source term in to high-density studies, since at the location of the analyzer, its contribution may not be negligible compared to that of edge sources.

CHAPTER 5

PURE PLASMA EXPERIMENTS: ION CONFINEMENT ON ISX-A

In the preceding chapters we have discussed charge exchange neutral analysis as an important ion diagnostic for tokamak plasmas, but one with potential limitations. We desribed a neutral analyzer which was designed and built, and more sophisticated data analysis methods which have been developed, in order to extend the usefulness of CX beyond these limitations. The improvements have been applied successfully in many plasma physics experiments performed on the ISX tokamak during a two-year period.

In this chapter and subsequent chapters we present results from some of these experiments which serve to illustrate the contributions made by these techniques. The primary motivation for this research was to facilitate ion measurements in neutral beam-heated plasmas in ISX-B. At high injection power levels required for high beta studies, the mass-energy analyzer has been found to be indispensable. Accordingly, results from some of these experiments are presented in Chapter 6. ISX-B has also been used to study plasma fueling by solid hydrogen pellet injection. These investigations benefit from the CX analysis, mainly owing to its ability to distinguish between the injected and target ions by mass identification. These data are discussed in Chapter 7.

In the present chapter, we consider energy confinement experiments performed in pure, ohmically heated plasmas in ISX-A. While such experiments did not require mass analysis, they did provide an opportunity to test the analyzer's performance in a conventional mode of operation. On the other hand, because fairly dense plasmas were being studied, the modeling procedure described in Chapter 4 was an essential part of the data interpretation. One of the most significant results was a verification of neoclassical ion energy transport in tokamak plasmas. (The neoclassical transport coefficients embody classical coulomb encounters between particles, accounting for the magnetic field configurations of toroidal confinement systems.) A related finding, uniquely observable in ISX, was a transition, with increasing density, from electron loss-dominated to ion loss-dominated gross energy confinement. Near this transition, ion temperature and bulk energy confinement time are both maximized with respect to density. These effects, which violate monotonically increasing dependences implied by, respectively, Artsimovich's formula[1] and empirical Alcator scaling[5], are nonetheless entirely consistent with the neoclassical theory in detailed ion transport simulations.

5.1 DENSITY SCANS IN ISX-A

The procedure used in ISX-A confinement studies[10] was to make density scans at fixed plasma current and toroidal field.* In a typical discharge, as exemplified by Fig. 5-1, the plasma was

*These experiments were directed by M. Murakami.

ORNL/DWG/FED 78-483 R2

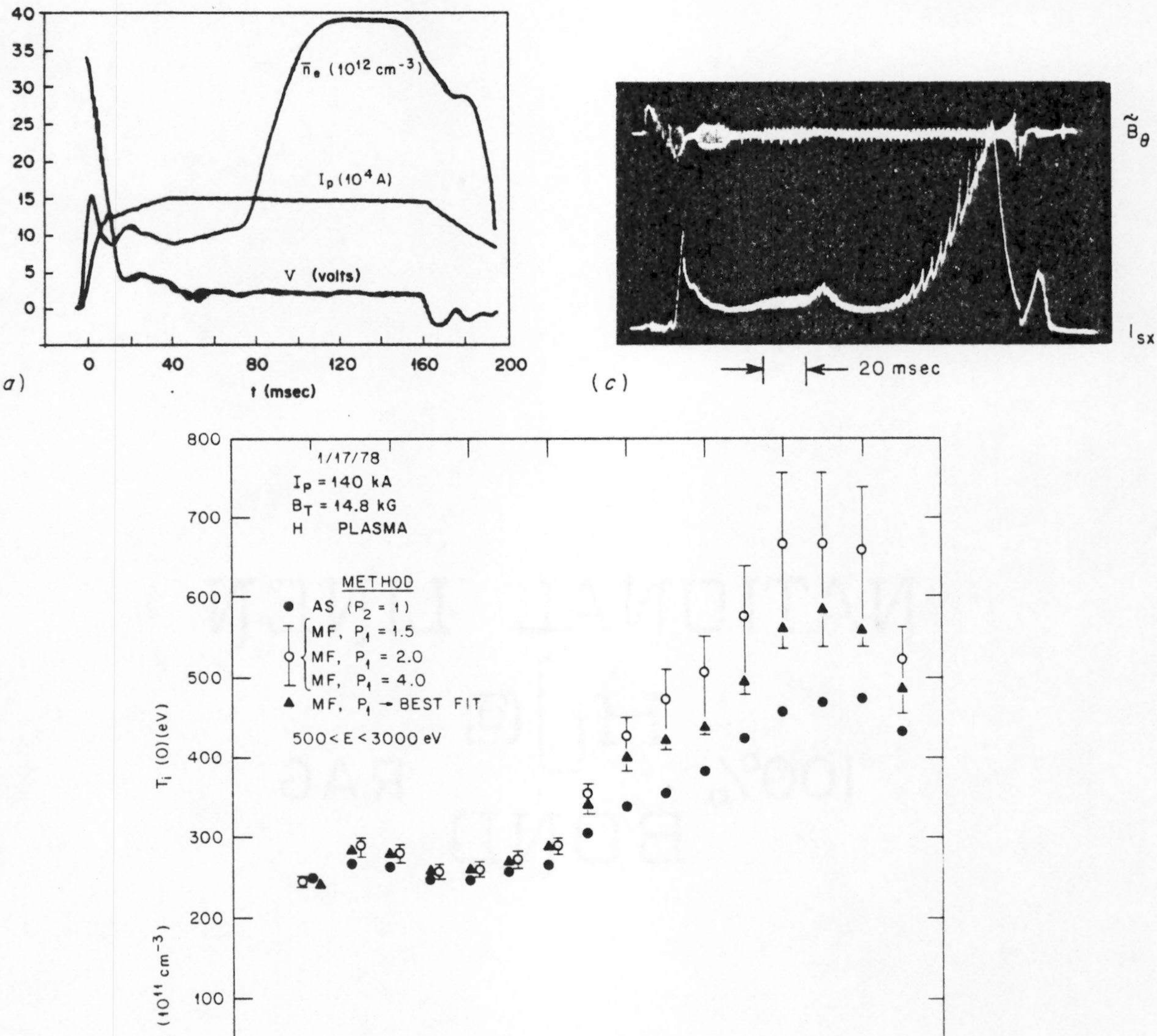

Figure 5-1. Time histories of plasma parameters in a typical ISX-A discharge. Parameters shown are: (a)plasma current, loop voltage, and line-averaged electron density; (b)CX-inferred ion temperatures using several different analysis methods; (c)Mirnov oscillations, B_θ, and PIN diode signals.* * Fig. (c) provided by ISX MHD group.

initiated by means of a "pre-puff" of gas into the machine preceeding the breakdown phase. When the plasma was well-established, as determined by the loop voltage and magnetic signal behaviors, at a low density, a controlled steady flow of H_2 or D_2 was introduced. The immediate response was a rapid increase in line averaged electron density, as measured by a 2 mm microwave interferometer, until an equilibrium value was obtained. It was found that fairly precise density control was possible by adjusting the flow rate of this delayed gas feed. This degree of control, and the capability of operating stably over a wide range of densities (typically $1 \times 10^{13} < \bar{n}_e < 6 \times 10^{13}$ cm^{-3}) are believed due to the cleanliness of ISX-A plasmas, in which Z_{eff} values between 1.0 and 2.0 were typically observed. The cleanliness, in turn, was the result of all-metal (stainless steel) construction of the primary vacuum chamber and the complete avoidance of high Z materials, such as tungsten and molybdenum, which had often been used as limiter materials in previous tokamaks.[7,8]

In Fig. 5-2 we plot ion temperatures measured in deuterium plasmas during density scan experiments. Here the importance of the using a more physical analysis procedure is demonstrated. The open circles in these figures denote central ion temperatures inferred by the asymptotic slope (AS) method discussed in Chapter 4. The solid circles with error bars designate values inferred by the model fit (MF) technique. By taking account of the central neutral target deficiency, profile effects, and neutral attenuation, this method

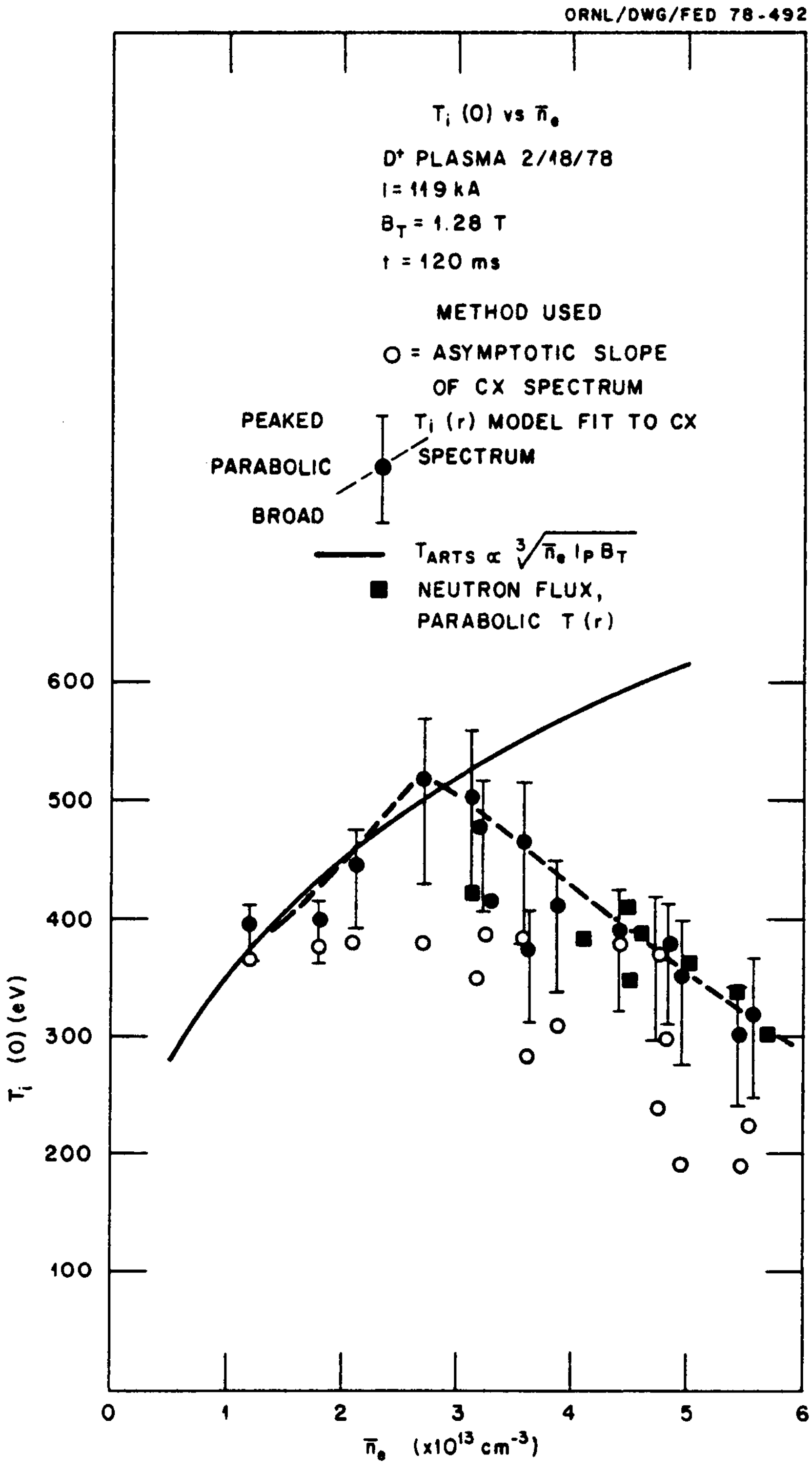

Figure 5-2. Ion temperature variation with density in deuterium plasmas. Values inferred from CX by AS and MF analysis are compared with those obtained from Artsimovich's formula, and neutron data.

gives temperatures which are up to 30% higher than values inferred by the AS method. The error bars reflect the profile uncertainty; in these cases a more peaked profile gives a higher temperature estimate. The magnitude of the discrepancy between the two analysis methods depends on both the density and the degree to which the asymptotic tail of the distribution is represented by the data. It has appeared necessary to perform the full MF treatment in each case; no simple and reliable correction "formula" has emerged.

Where the density was sufficient to produce a significant DD neutron yield, ion temperatures were also inferred from absolute measurements of the neutron fluxes*. These temperatures are also plotted in Fig. 5-2, showing good agreement with the CX measurements.

As a benchmark, it is useful to compare peak ion temperatures measured in ohmically heated tokamaks with a simple formula, due to Artsimovich,[1] which was derived from a point model assuming "plateau" confinement scaling, and classical power transfer from electrons to ions. Artsimovich's result is given by Eq. 5.1

$$T_i(0) \cong \text{const.} \times 6 \times 10^{-7} \times \frac{(\bar{n}_e I_p B_T R_o{}^2)^{0.33}}{A_i^{0.5}} \qquad 5.1$$

---

*Neutron data were provided by J. T. Mihalczo.

where the constant is determined within a factor of order unity, embodying any dependence on any ion temperature profile shape. The units used in this equation are eV for T_i, cm^{-3} for $\bar{n}_e$, amperes for I_p, gauss for B_T, cm for R_o, and amu for A_i. The density dependence implied by this formula is plotted with the data in Fig. 5-2. The agreement is good up to the point where the measured ion temperature is maximal (except that the A_i dependence is not obeyed; A_i was set to 1 despite the use of deuterium), but at higher densities, the formula clearly does not apply. In order to explain this departure it is necessary to perform a more careful power balance, taking the electron temperature into account. Artsimovich's formula reflects no electron temperature dependence because it presumes $T_e >> T_i$, under which condition the dependence is weak. It will be seen in the following section that the ion temperature dependence seen in Fig 5-2 may be reproduced in power balance calculations.

Neutral densities inferred from CX analysis are plotted as a function of density in Fig. 5-3. Despite the increased gas feed rate needed to sustain a higher-density discharge, the neutral density at the position of the CX analyzer actually decreases with density, in an approximately exponential fashion. In light of the calculated results presented in Section 4.5, however, this observation is not surprising. The denser, and therefore thicker, plasmas prevent the neutrals from migrating a great distance from their sources; this is especially true in the cases shown for ISX-A,

ORNL/DWG/FED 78-493

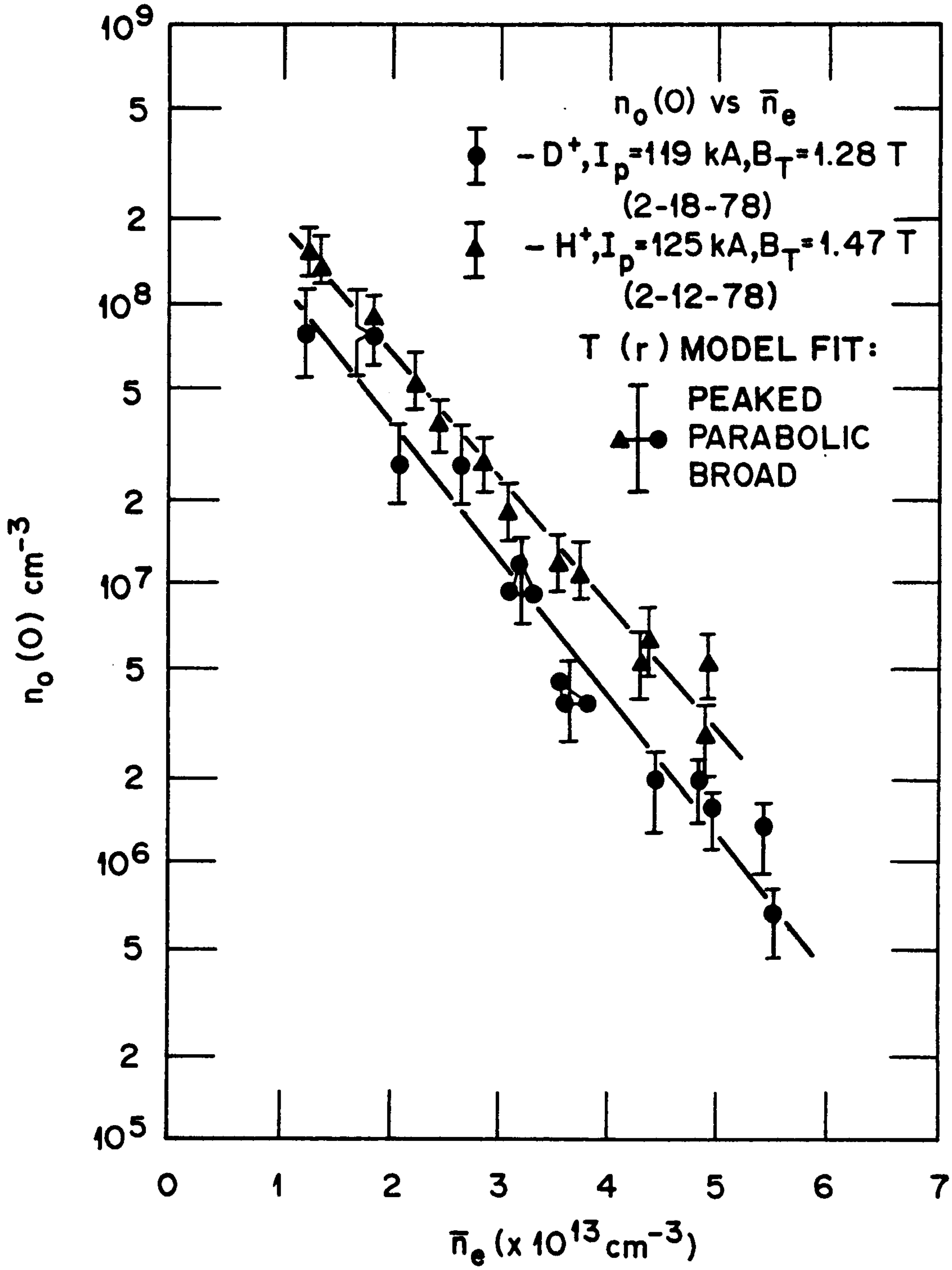

Figure 5-3. Neutral density variation with density in hydrogen and deuterium plasmas. As discussed in the text, this must be regarded as a local measurement only, not usable for estimates of charge exchange losses.

where titanium gettering of the wall was used, presumably reducing the reflection coefficient for neutrals.

5.2 ELECTRON-ION POWER BALANCE ANALYSIS OF THE DENSITY SCANS

The electron density and temperature profiles are well measured in tokamaks, including ISX, by laser Thomson scattering.* In ohmically heated plasmas, ions derive virtually all their energy by classical power transfer from the electrons. Thus we can use the measured electron profiles and classical power transfer to test whether the ion temperature is consistent with ion energy loss by neoclassical heat conduction, without having to model the electron confinement as well. Values obtained by this means** using the revised Hinton-Hazeltine neoclassical transport coefficients[57] are plotted in Fig. 5-4, as well as values obtained by arbitrarily doubling these coefficients. The two curves bracket the experimental data, for the most part, leading to the conclusion that ion confinement is explainable in terms of approximately neoclassical ion heat conduction. Moreover, given the electron temperature behavior in ISX-A, the observed maximum in the ion temperature is consistent with the neoclassical theory, also.

---

*Data referred to herein were provided by the ISX Thomson scattering group under the direction of M. Murakami.

**The transport simulations were performed by H. C. Howe.

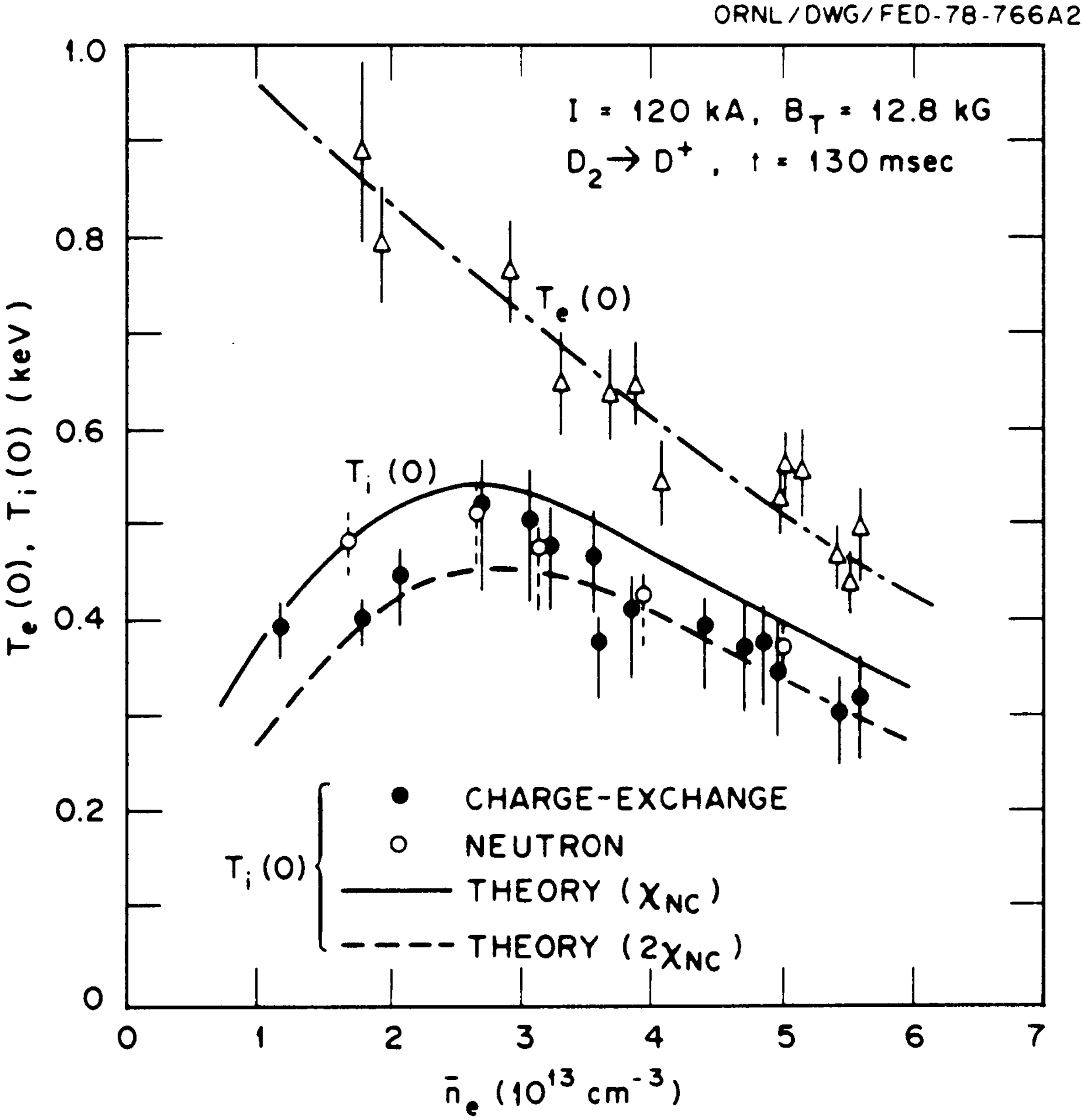

Figure 5-4. Comparison of measured ion temperatures with values obtained in ion power balance calculations which use one and two times neoclassical ion heat conduction.

The ion temperature behavior is reflected in that of the gross plasma energy confinement time, using the experimental definition $\tau_E = \frac{W_e + W_i}{P_{OH}}$ as shown in Fig. 5-5. The low-density trend exhibits the dependence often observed in tokamaks, $\tau_E \propto \bar{n}_e$ commonly referred to as "Alcator scaling."[5] ISX-A obeys this scaling up to a line-averaged density of about 3×10^{13} cm^{-3}, except that the magnitude of the scaling coefficient is a factor of ~2 higher than the empirical value, which was derived by the authors of Reference (5) from the published results of a number of ohmically heated tokamaks. The departure from this trend at higher density can be attributed to the increasing importance of ion losses to the gross power balance.

The last point is reinforced by the results plotted in Fig. 5-6, which are obtained from power balance calculations. We define gross energy confinement times τ_{Ee} and τ_{Ei}, for electrons and ions respectively, in Eq. 5.2.

$$\tau_{Ee} \equiv \frac{W_e}{P_{OH} - P_{ei} - \dot{W}_e} \qquad 5.2a$$

$$\tau_{Ei} \equiv \frac{W_i}{P_{ei} - \dot{W}_i} \qquad 5.2b$$

W_e and W_i are the total stored electron and ion kinetic energy

ORNL/DWG/FED-78-666RA2

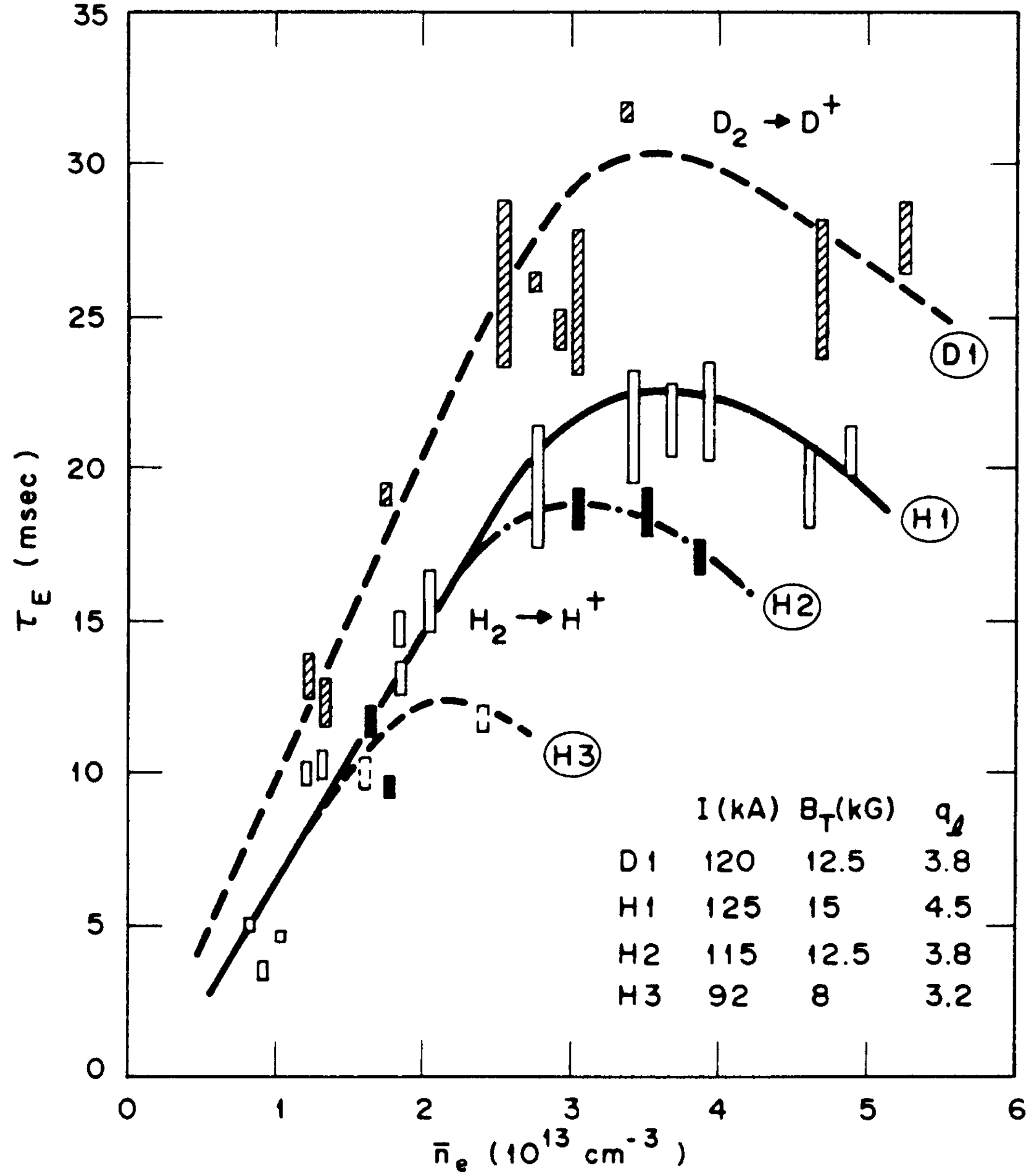

Figure 5-5. Energy confinement time in ISX-A as a function of density. The experimental definition $\tau_E = \frac{(W_e + W_i)}{P_{OH}}$ is used. Non-monotonic behavior reflects ion temperature trend seen in Fig. 5-4.

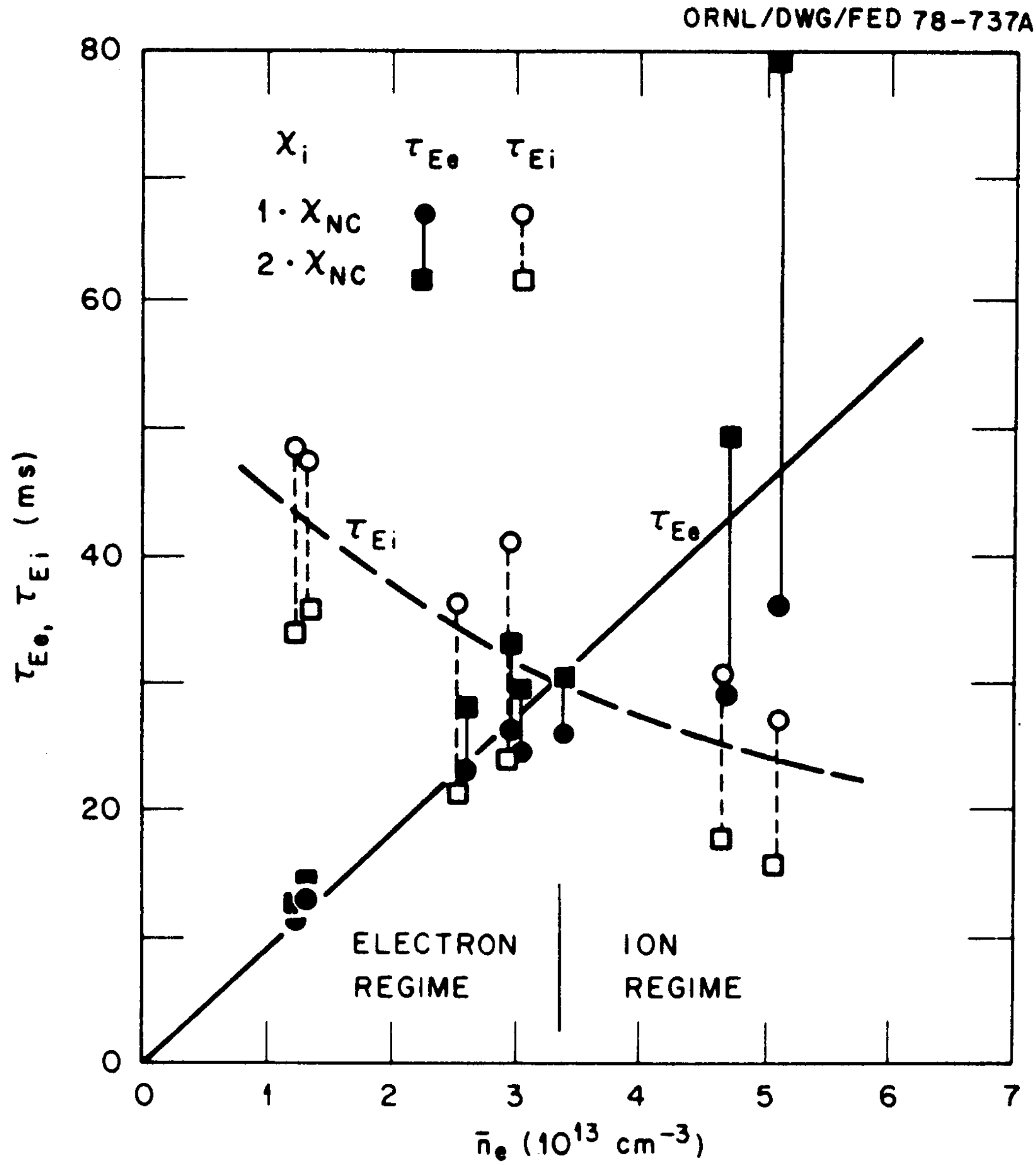

$(n_e)_{crit}$ IS LOW IN ISX-A, BECAUSE

- LARGER $\tau_{Ee}/\bar{n}_e$
- LOWER τ_{Ei} DUE TO LOWER I AND/OR B_T

Figure 5-6. Electron and ion energy confinement times inferred from power balance calculations. A transition from electron loss-dominated to ion loss-dominated confinement is observed. Figure 6-1. Typical parameters for injection-heated discharges in ISX-B. The case shown is discussed further in the text.

contents in joules; P_{OH} is the total ohmic heating power, and P_{ei} the total electron-to-ion power transfer, in watts. In this case the power balance pertains only to the core of the plasma, extending from the center to r = 2/3a. This is done to minimize the dependence on radiative losses and other edge-specific effects; also most of the current, and hence most of the ohmic heating power deposition, is within this radius. The τ_{Ei} dependence is a consequence of the neoclassical ion confinement and the particular profiles which resulted from the power balance calculation. The electron energy confinement time embodies no electron confinement models per se. Rather it is calculated from the measured stored electron energy, and the net electron power input, which is just the ohmic heating power less power transferred to the ions. The density at which the two curves in Fig. 5-6 intersect corresponds closely with the maximum in the confinement time, case D1, and therefore reflects a transition from electron loss- to ion loss-dominated confinement.

This effect is a consequence of worsening ion confinement and closer thermal coupling with the electrons with increasing density. It was observable in ISX because ISX was able to operate in a mode disadvantageous to ion confinement, namely at high density and low plasma current and toroidal magnetic field. Simultaneously, the electron confinement was quite good, apparently due to machine cleanliness and the use of gas puffing to induce favorable MHD behavior. Fig. 5-6 indicates, in fact, that electron energy confinement continues to improve with density, and the scaling $\tau_{Ee} \propto$

$\bar{n}_e$ is suggested, although inconclusively due to the sensitivity to uncertainties in the ion temperature.

5.3 SUMMARY

These studies performed on ISX-A demonstrate the importance of good measurements of ion phenomena in tokamak plasmas, as the observed ion temperature dependence was completely unexpected from prior experience. The need for accurate CX emission modeling to properly analyze the data is also clear, particularly where high density plasmas are being investigated. These were the author's contributions to the experiments.

The results given in this chapter lead to the conclusion that the ion confinement is approximately neoclassical over a wide range of densities in tokamak plasmas. This is true whether the electron losses or the ion losses dominate the gross energy confinement. Clearly, to improve the overall confinement at high densities, it is necessary to improve the ion confinement.

One way to do this is to increase the toroidal field and plasma current, but these are inconsistent with attempts to maximize the beta. Neoclassical theory predicts that raising the ion temperature should have this effect, but this is impossible to isolate experimentally with ohmic heating alone. With power supplied directly to ions from neutral beams, however, one might expect higher temperatures and therefore better high density confinement. Investigation of this question is an important area for ISX-B.

CHAPTER 6

MIXED PLASMA EXPERIMENTS: NEUTRAL BEAM HEATING ON ISX-B

In this chapter we discuss results of CX measurements made in the course of high beta experiments on ISX-B. Recent investigations in tokamak MHD stability theory have predicted the existence of equilibria with toroidal beta values well in excess of 5%.[58] The most favorable configurations for high beta, these studies show, are those with vertically elongated, "D"-shaped cross sections. Since the realization of high beta equilibrium is of great economic significance for fusion reactors, because it minimizes the size and toroidal field strength required for such systems, the ISX-B tokamak was constructed to investigate this area experimentally.

To study the theoretically optimum configurations in ISX-B, shaping control has been incorporated to produce and compare elliptical, "D"-shaped, and circular cross section plasmas. One particular objective is to determine the stability limits in each of these configurations; to ensure that the maximum attainable beta values are stability-limited rather than power-limited, a machine of moderate size (major radius R_0 = 93 cm, minor radius a = 27 cm) was designed, with provision for intense neutral beam injection heating (3 MW). By comparison, the Princeton Large Torus (PLT) has approximately six times the circular plasma volume, with only 2.4 MW injection.

Neutral beam heating experiments in ISX-B were begun in November, 1978. At this writing, the maximum power obtained from the two 35-40 keV beams has been about 1.0 MW into a circular plasma. While this does not approach the design capacity of the system, it is enough to reach a physics regime where the plasma is beam-dominated in terms of its power balance. That is, since the ohmic power input in these experiments is on the order of 0.1-0.2 MW (100-145 kA plasma current, 1-2 volts loop voltage), neutral beams are supplying most of the power during the injection pulse.

In such experiments, it is obviously imperative to make good measurements of both electron and ion temperatures, but as has been mentioned in Chapter 2, there is a potential difficulty in making the CX measurement in the presence of neutral beam injection, especially intense injection. The physics of neutral injection in tokamaks is well developed,[59] but a brief summary is appropriate here to elucidate the effect on CX measurements.

The injected monoenergetic neutrals (actually, there are three components at full, half, and one-third beam voltage due to molecular dissociation in the drift tube, but they can be regarded as three independent monoergetic beamlets) are ionized by electron and proton impact or by charge exchange with thermal ions, resulting in fast ions. Since injection is tangential to the toroidal direction in ISX-B, the fast ions are born with small pitch angles; i.e. they are roughly parallel to the magnetic field. However, they quickly slow down and scatter in pitch angle by classical Coulomb interaction with the plasma; in so doing they heat first electrons, and then ions, and some are lost in the process through charge exchange or by being scattered into unconfined orbits. Eventually a steady-state, anisotropic, fast ion distribution evolves, which can distort even a perpendicular CX neutral spectrum, as was seen in Fig. 2-1, producing a long asymptote whose apparent "temperature," if interpreted as such, would be several (5-10) keV. Such an interpretation is incorrect, however, because the fast ions comprise only a small fraction of the total ion population and no single measurement can characterize the distribution due to its anisotropy. Thus the need for mass identification and analysis of the thermal and fast ion components is clear.

To date the major interest has been in the thermal ions in ISX-B, since only the single perpendicular chord has been accessible. The experimental procedure has therefore been to inject hydrogen beams into deuterium plasmas. This allows for the possibility of using thermal DD neutron emission as an additional ion temperature diagnostic. Data presented in this chapter will demonstrate the contributions made by the mass-energy analyzer in these studies.

We digress here to remark that the fast ions themselves are of interest as well for a number of reasons. In a device such as ISX-B, they make a very substantial contribution to the plasma pressure, and hence to beta. One also anticipates a significant fueling effect of the injected particles,[60] and thus some impact on the particle balance. It is also possible to use the fast ions as a diagnostic, using their classical scattering and slowing-down properties to determine plasma parameters which affect them, such as Z_{eff}.[11] Therefore, more effort will be given in the near future to studying fast ions as well as thermal ions. To this end, the mass-energy analyzer of this report is presently being reconfigured as a scanning tangential analyzer, and a scanning mass-energy analyzer of a different design is being implemented as a new perpendicular analyzer. Both analyzers will also be able to use a diagnostic beam for flux localization, a technique described in Chapter 2. With these improved capabilities, it should be possible to study the fast ion spectrum in great detail, and to investigate some new features of the bulk ions as well, for example, the presence or absence of beam-induced toroidal rotation.

6.1 ILLUSTRATIVE CASE: 1 MW INJECTION

In this section, we demonstrate the application of the mass-energy analyzer in an experiment incorporating the highest injection power used to date on ISX-B, 1 MW. This power was obtained from two H^o neutral beams, and was measured by calibrated calorimetric targets in the beamlines*. The target plasma was D^+ at a line density of approx. $2.5\text{-}3.5 \times 10^{13}$ cm^{-3}; the ohmic heating current was 140 kA, the toroidal magnetic field was 1.15 T, and the

*The sources and beamlines were developed by the Fusion Energy Division's Plasma Technology Section; beam operations and calibrations were provided by P. H. Edmonds, S. C. Bates, and J. Kim.

plasma cross section was circular or slightly elongated. Time histories of discharge parameters are displayed in Fig. 6-1. We observe in this figure the "density clamping" phenomenon which has recently been discovered in ISX-B, a beam-induced effect in which the normally monotonic density rise is abruptly halted shorly after injection begins. The density was measured in this case by both 2 mm microwave* and 0.385 mm far infrared (FIR)** interferometers.

In Fig. 6-2 are superimposed plots of both hydrogen and deuterium neutral flux density spectra at several times during the discharge. These spectra represent composites of data taken during a sequence of approximately 25 nominally identical discharges. The deuterium spectra, representing the bulk ions, show clear evidence of neutral beam heating; moreover, they remain nearly linear over several decades, indicating Maxwellian behavior before and during the injection heating phase. It must be remembered, however, that these are emitted flux spectra, not local distribution functions; they display a concave-upwards curvature which is typical of CX spectra, reflecting the strong contribution to the lower energies from the edge layers, where the neutral target densities are greatest.

---

*2mm data were provided by J. B. Wilgen.

**FIR data were provided by D. P. Hutchinson and colleagues.

ORNL DWG 79-2654 FED

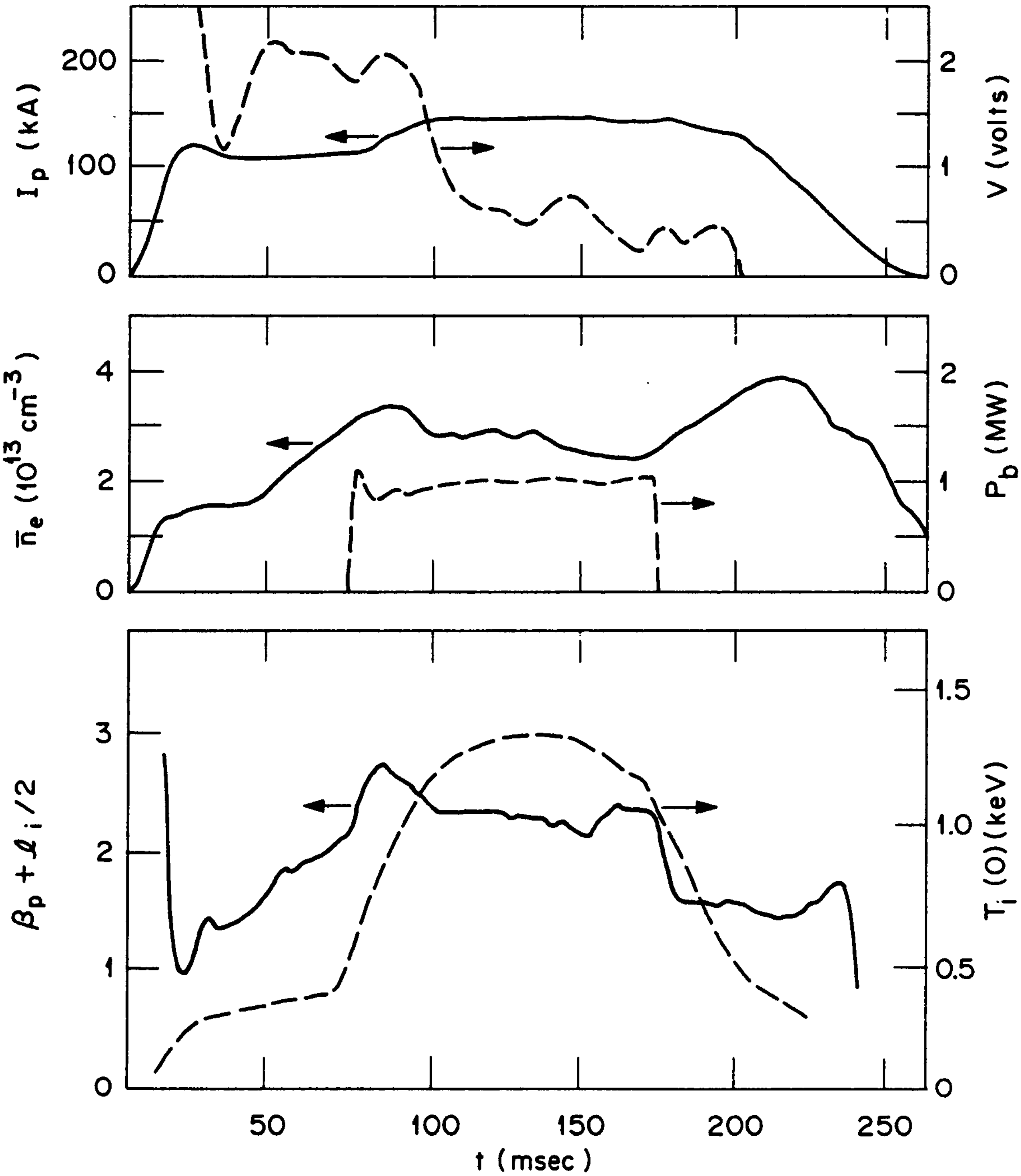

Figure 6-1. Typical parameters for injection-heated discharges in ISX-B. The case shown is discussed further in the text.

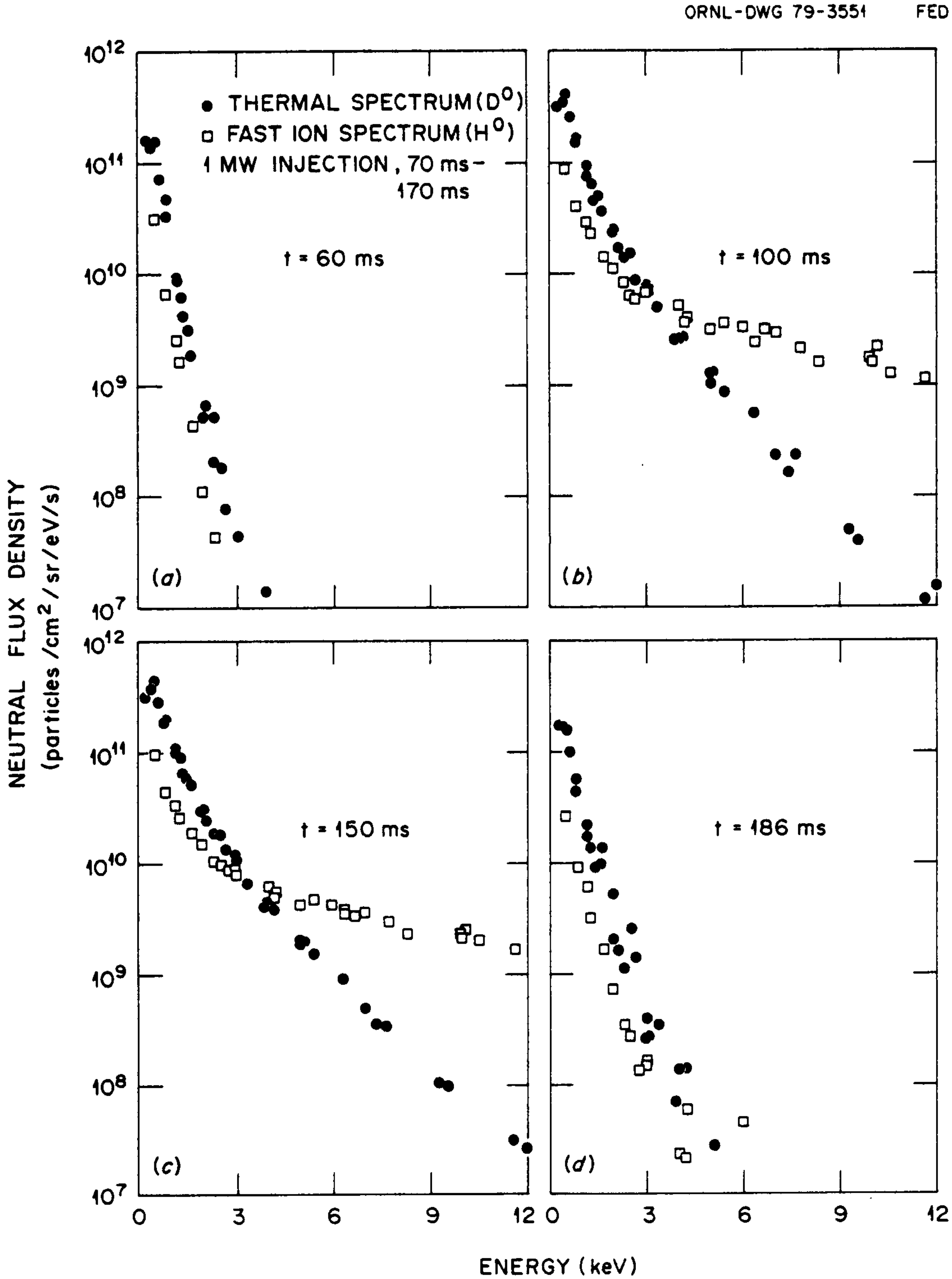

Figure 6-2. Neutral flux spectra at different times during injection-heated discharges. The thermal and fast ion components were measured by mass-resolved charge exchange analysis.

In the hydrogen spectra, one observes a small thermal population prior to injection. This probably results from hydrogen introduced in previous shots by injection, which had been adsorbed by the wall, then desorbed by recycling in the present shot. After injection begins, the fast ion tail builds up continuously until it reaches a steady state. It dominates the total CX flux for all energies greater than about 3 keV, yet the mass analysis is able to resolve the deuterium spectrum out to at least 10 keV with no apparent contamination by the fast ions. Without this capability, it would be impossible to measure the ion temperature during injection heating.

The thermal data were analyzed by the methods of Chapter 4, with the ion temperature results plotted in Fig. 6-3. As was pointed out before, the fixed-chord restriction requires that some assumption be made concerning the T_i profile shape. Here, it was assumed that the profile was parabolic ($p_1 = 2$, $p_2 = 1$, using the parameters introduced in Chapter 4). The sensitivity of the results were tested by using $p_1 = 1.5$ and 4, which gave, respectively, higher and lower values of $T_i(0)$. These ion temperatures, obtained by MF analysis of the data between 0.4 and 5.5 keV, are indicated by the solid circles and error bars in Fig. 6-3. The measured flux spectrum and the calculated flux spectrum resulting from the MF analysis of the data taken at 120 ms are shown in Fig. 6-4.

As another check on the analysis, we fit the data over different energy bands in the spectrum. Ideally, the results should be independent of this choice, but in fact we anticipate some variation

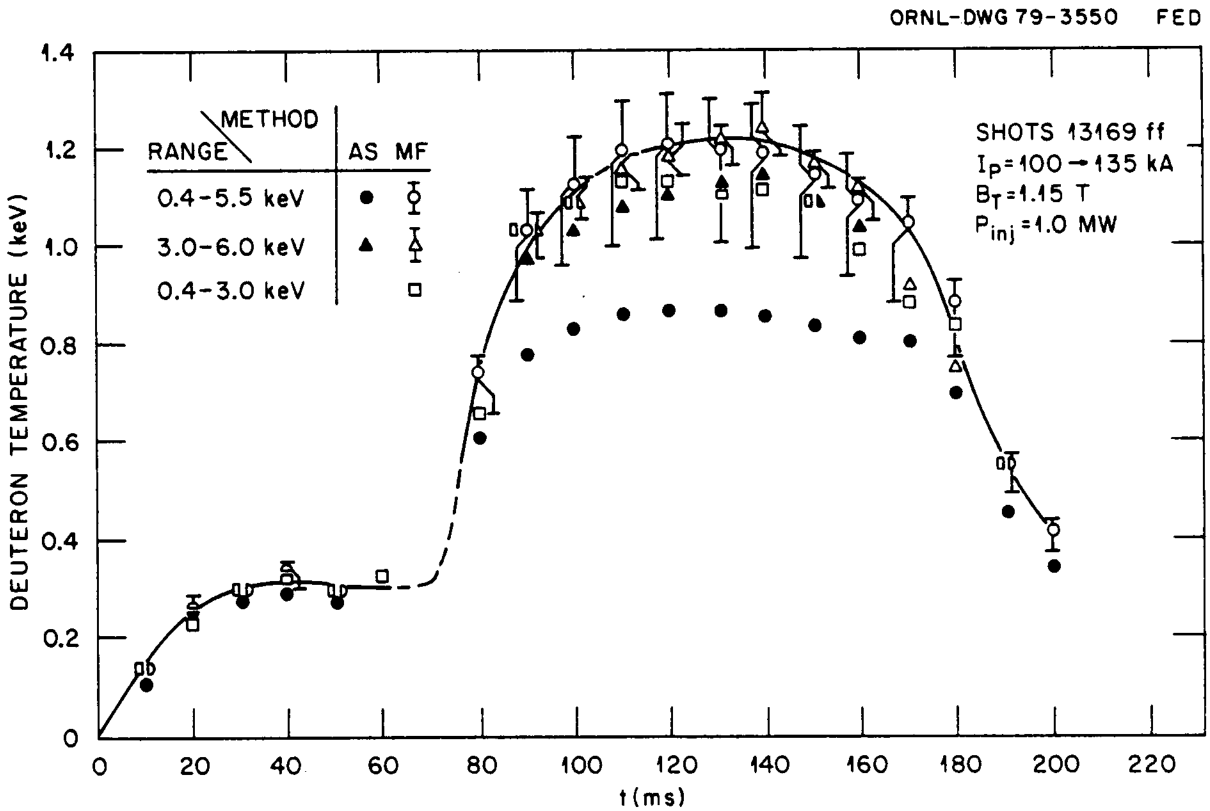

Figure 6-3. Ion temperature inferred from CX in several analyses of CX data, for 1 MW injection on ISX-B.

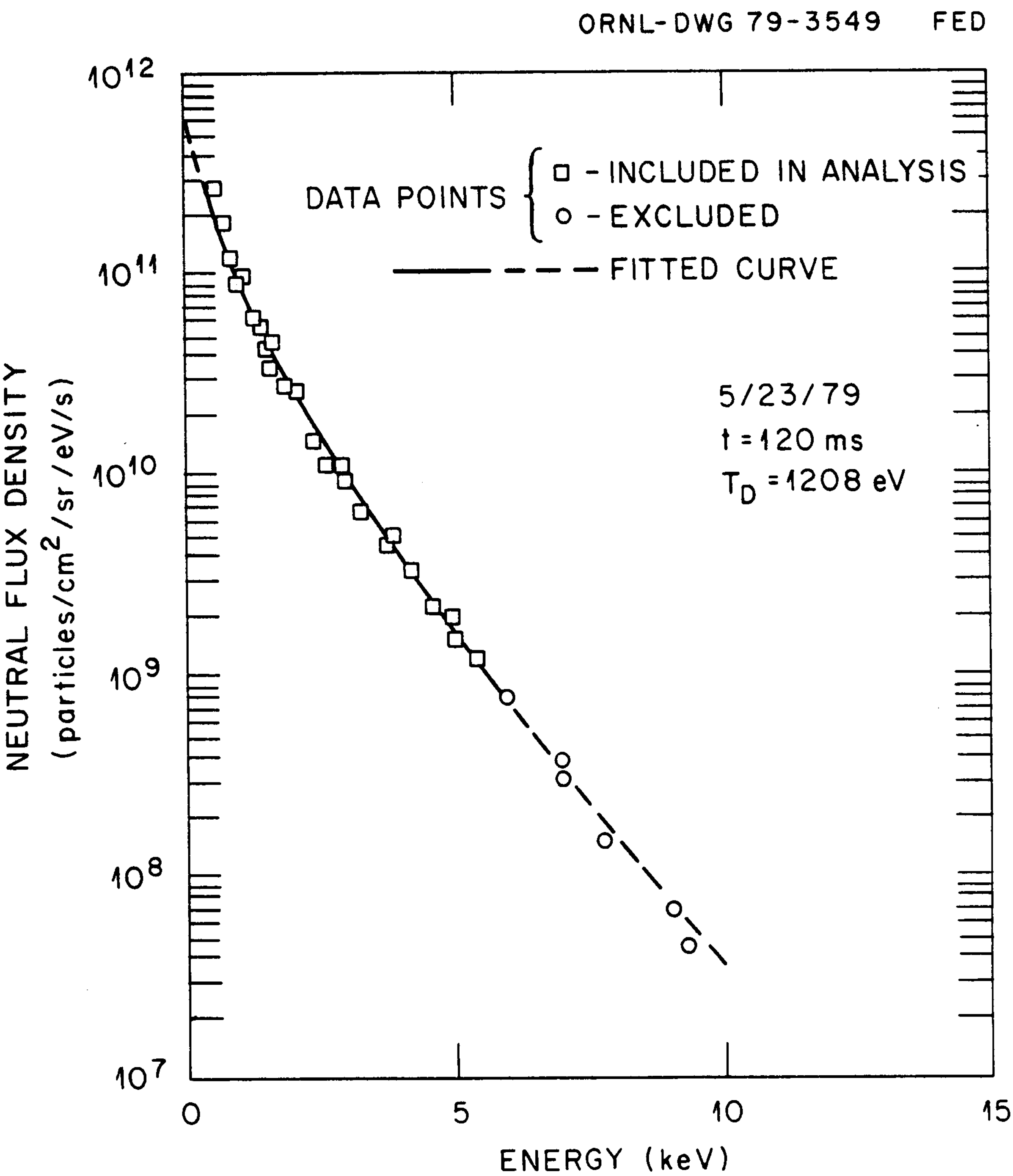

Figure 6-4. Fitted and measured flux for 120 ms point of 1 MW injection case.

resulting from the arbitrariness of the assumed profile. In light of the discussion of the asymptotic approximation of the CX spectrum, we expect the highest energies to best represent the center of the plasma. However, as signal strength decreases with increasing energy, care must be taken not to use energies so high that the spectrum is overwhelmed by noise, such as electrical pickup, hard x-rays and ultraviolet photons, and poor counting statistics. Lower energy data are free of those problems, but do not represent the center as well. From the different symbols in in Fig. 6-3, it is seen that the model fits in several different energy ranges give fairly consistent results. When the lower energy data are excluded, the nominal ion temperature remains nearly unchanged, but the error bars are reduced. This implies that the data points between 3.0 and 6.0 keV represent the center better, so that values closer to the true ion temperature are obtained for any profile choice, than the data between 0.5 and 5.5 keV. The fact that the parabolic values are the same for both ranges indicates that the parabolic profile must be close to the actual T_i profile.

The physical nature of the modeling problem is illustrated in Fig. 6-5. The profiles in this figure pertain to the 120 ms point of Fig. 6-3. The ion temperature profile is parabolic by assumption, and the peak value is that determined as a result of the MF procedure. The density, not shown, was also assumed to be parabolic, with a line-averaged value equal to that obtained from the interferometers. The neutral density profile calculated in the last

ORNL-DWG 79-3548 FED

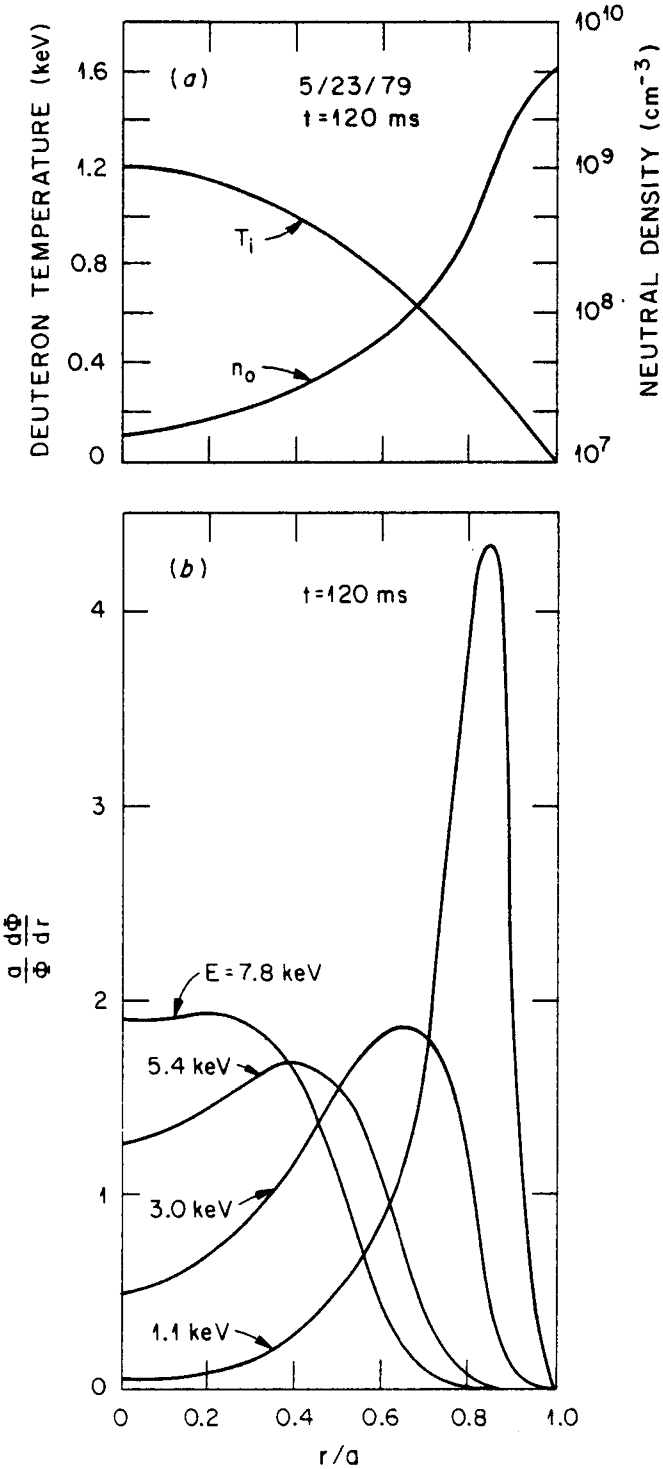

Figure 6-5. Profiles showing origins of measured CX flux. The modeling procedure assumes the ion temperature profile (a), and calculates the neutral density profile (a) and CX flux origination profiles (b) at several energies. Central behavior is best represented by the most energetic neutrals, signal strength permitting.

MF iteration is also shown in Fig. 6-5a. In Fig. 6-5b are displayed flux origination profiles for four different energies. This simply shows where the detected flux at a particular energy originates in the plasma, and is effectively the integrand of Eq. 4.8, normalized to unit area under each curve. It is seen that at E = 1.1 keV $\cong T_i(0)$, most of the signal originates near r = 0.85a, where T_i = 400 eV $\cong 1/3 \times T_i(0)$. Even at E $\cong 5 \times T_i(0)$, the flux comes mainly from a layer extending from one-fifth to one-half the plasma radius. Only the very highest energies begin to be dominated by central contributions, and even at E $\cong 7 \times T_i(0)$, the profile is far from its asymptotic limit, that is, a delta function, as was derived in Section 4.3 (see Eq. 4.9). We have thus illustrated that which was indicated previously; that the AS analysis requires a very asymptotic spectrum (E > $7 \times T_{io}$ in this case) to be valid, and otherwise makes a significant error in the inferred temperatures, as Fig. 6-3 shows.

6.2 ION POWER BALANCE STUDIES AT P_{inj} = 630 kW

Power balance calculations may be used to simulate ion confinement with injection as was done for the ohmic heating studies in ISX-A. We consider three well-documented (that is, good laser profiles and CX spectra were obtained) experiments in which the ohmic heating current, toroidal field, and injection power were kept approximately constant, at values of 110-115 kA, 1.15 T, and 630 ± 20% kW, respectively. The density was varied to give low ($\bar{n}_e = 1.6 \times 10^{13}$), medium ($3.1 \times 10^{13}$) and high ($5.2 \times 10^{13}$ cm^{-3}) density cases.

Time histories of the density, injection pulse timing, and ion temperature are displayed in Figs. 6-6, 6-7, and 6-8 for the three respective cases. The ion temperatures were determined by the author using MF analysis of the CX data, subject to the same profile assumptions made in the previous section. The densities were measured by 2 mm microwave interferometer.

The electron temperature, and electron and ion density, profiles for the medium density case are shown in Fig. 6-9*. The electron density and temperature profiles are measured by laser Thomson scattering. The ion density is a calculated fraction of the electron density, determined from the measured Z_{eff} (3.1) by assuming iron ($Z_0 \leq 26$) to be the impurity species.

The ion power balance calculations are analogous to those performed for ohmic heating experiments such as those described in the previous chapter. Additionally, it is necessary to calculate the power derived from the beams. This is a plausible calculation since it embodies only classical processes and has generally led to results which are consistent with experiment. A simplified treatment is used here, in which the fast ions are assumed to remain on their birth flux surfaces; the deposition profiles, in turn, are calculated from

---

*The profiles and the power balance calculations described in this section were provided by the ISX Thomson scattering group, under the direction of M. Murakami.

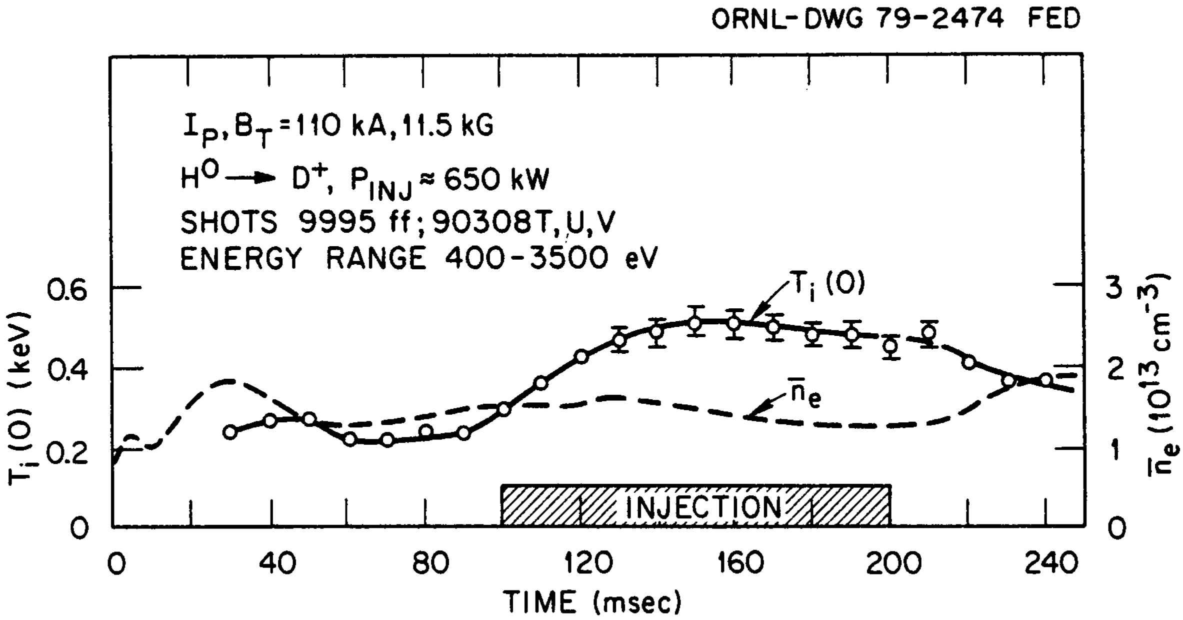

Figure 6-6. Density and ion temperature histories for the low density case.

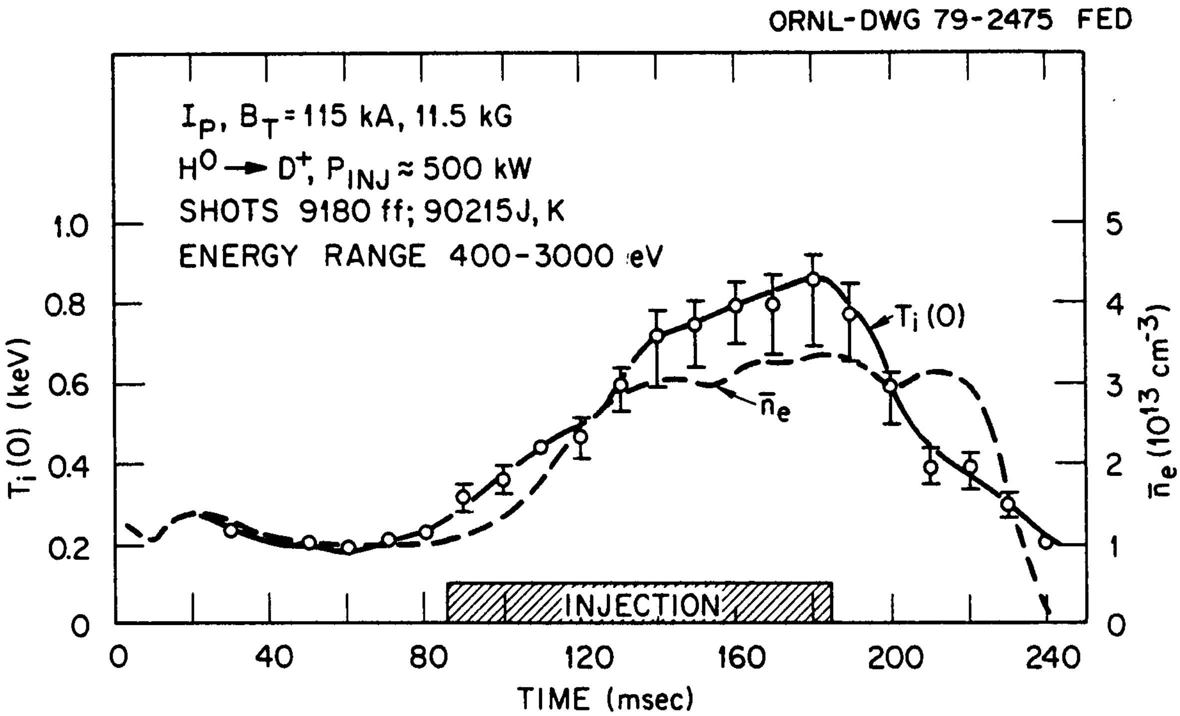

Figure 6-7 Density and ion temperature histories for the medium density case.

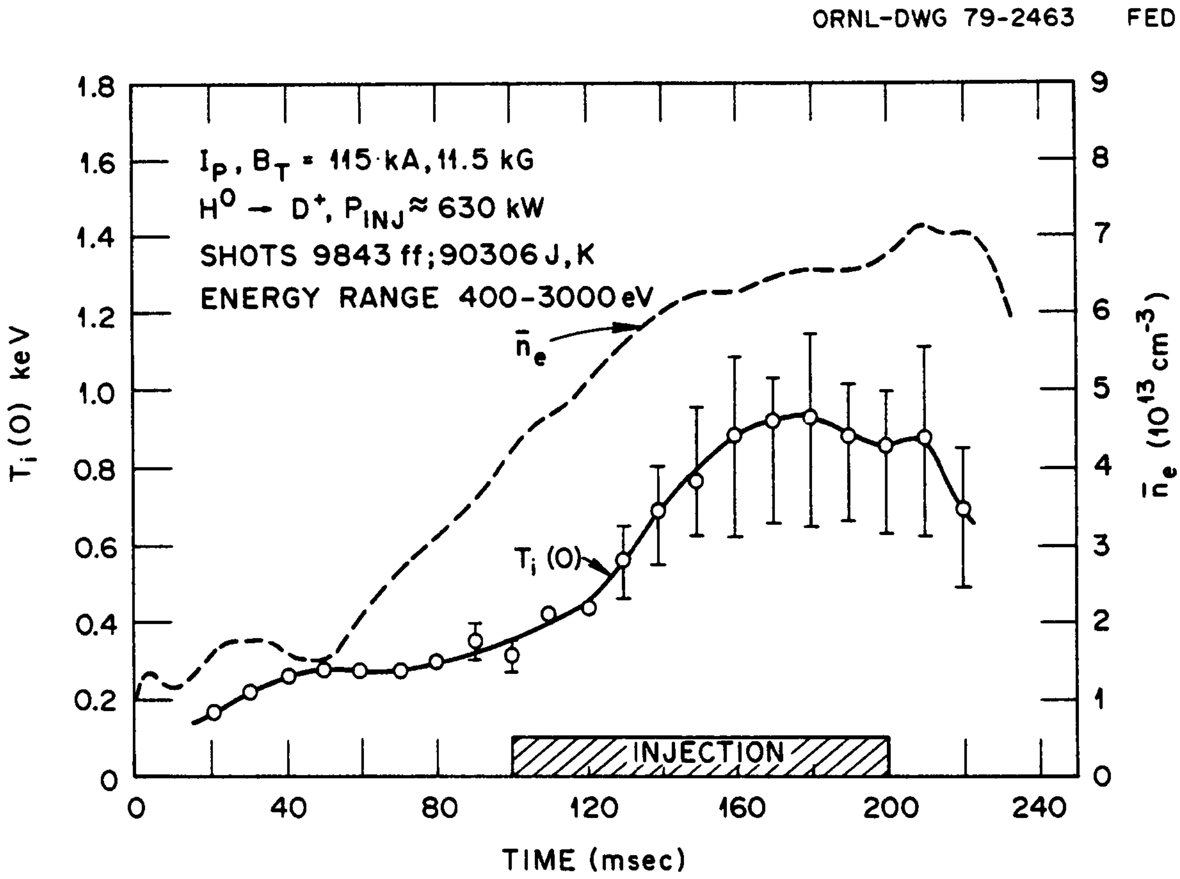

Figure 6-8 Density and ion temperature histories for the high density case.

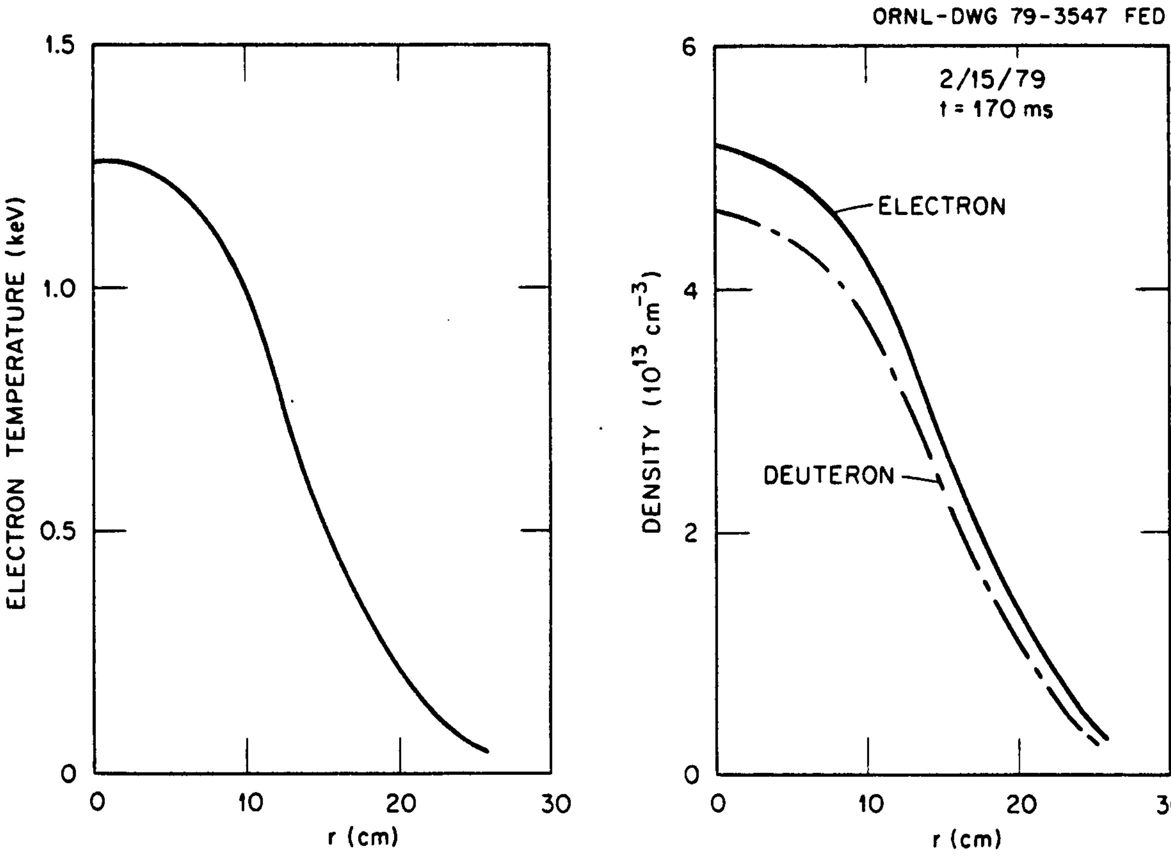

Figure 6-9. Laser profiles for the medium density case. Deuteron density was inferred from the Z_{eff} measurement.

the beam trajectory and the local mean free paths for the various trapping processes. Power transfered from fast ions to electrons and bulk ions is calculated at each radial position from the moments of an analytic solution to the Fokker-Plank equation which governs the slowing-down and scattering process.

As in the ohmic heating studies there are two principal free parameters: the neutral density, which enters in the calculation of both fast and thermal ion charge exchange losses, and the ion heat conduction coefficient. Different values of these parameters were tried in an effort to make the power balance calculations reproduce the observed ion temperature. The results are given in Table 6-1. The high density power balance is relatively insensitive to the neutral density; neoclassical heat conduction gives nearly the correct ion temperature, irrespective of neutral variations by a factor of ten. In the medium density case the ion temperature is reproduced either by invoking anomalous confinement (approaching ten times neoclassical) or by assuming a neutral density twenty times the measured value. Similarly, the low density power balance requires a large correction factor to either the CX-measured neutral density or to the neoclassical transport coefficients to obtain agreement with the measured temperatures.

The high density case gives rather conclusive evidence of neoclassical behavior in that regime. The insensitivity of the results to variations about the CX neutral density indicate the unimportance of charge exchange losses relative to neoclassical ion

TABLE 6-1

ION POWER BALANCE CALCULATIONS

	MEASURED			CHOSEN		CALCULATED	
	$\bar{n}_e$ (cm^{-3})	T_i^a (eV)	n_o^a (cm^{-3})	n_o/n_{ocx}	K_i/K_{neo}	T_i (eV)	n_o^b (cm^{-3})
HIGH	5.2×10^{13}	850	3.5×10^6	1	1	835	Indeterminate
				1	2	675	
				2.3	1	830	
				0.45	1	840	
MED	3.1×10^{13}	800	9.2×10^6	1	1	1540	2.8×10^8
				1	10	610	
				10	1	1220	
				30	1	850	
LOW	1.6×10^{13}	500	5.3×10^7	1	1	2380	1.1×10^9
				1	2	2126	
				20	1	500	

[a] Measured by CX

[b] Inferred by requiring T_i(calc) = T_i(meas) and $K_i \cong K_{neo}$.

losses. This is due to the exclusion of target neutrals by the thick plasma, and to the fact that the slowing down time of the fast ions is so short (16 ms at r = 0, 8.5 ms at r = 14 cm) that they give up their energy to the plasma before having a chance to be lost by charge exchange.

The other cases are inconclusive, but if neoclassical confinement is simply invoked, based on the results of ISX-A, as well as those of ORMAK, PLT, and other injected tokamaks, then the neutral density must be at least a factor of ten higher than the values inferred by CX analysis. In light of the axial neutral density asymmetries predicted by the 2D calculations in Chapter 4, this result is not surprising. Unfortunately, this leaves one without any direct measurement of neutral density for estimating the charge exchange losses in these power balance calculations. That this is a serious handicap may be seen in Fig. 6-10, which gives, in the form of a block diagram, an accounting of the various losses and power transfers in the medium density power balance, assuming neoclassical transport. Nearly one-third of the injected power is lost by fast ion charge exchange. Most of this loss detracts from the ion heating, since it is the electrons which are heated first by slowing down fast ions. (The critical energy at which energy transfer from fast ions to electrons and bulk ions is equal is approximately $9.3 \times T_e \cong 11$ keV; thus a 40 keV fast ion loses roughly three-fourths of its energy to electrons before heating ions, by which time it is likely to have been lost by charge exchange.)

ORNL-DWG 79-3546 FED

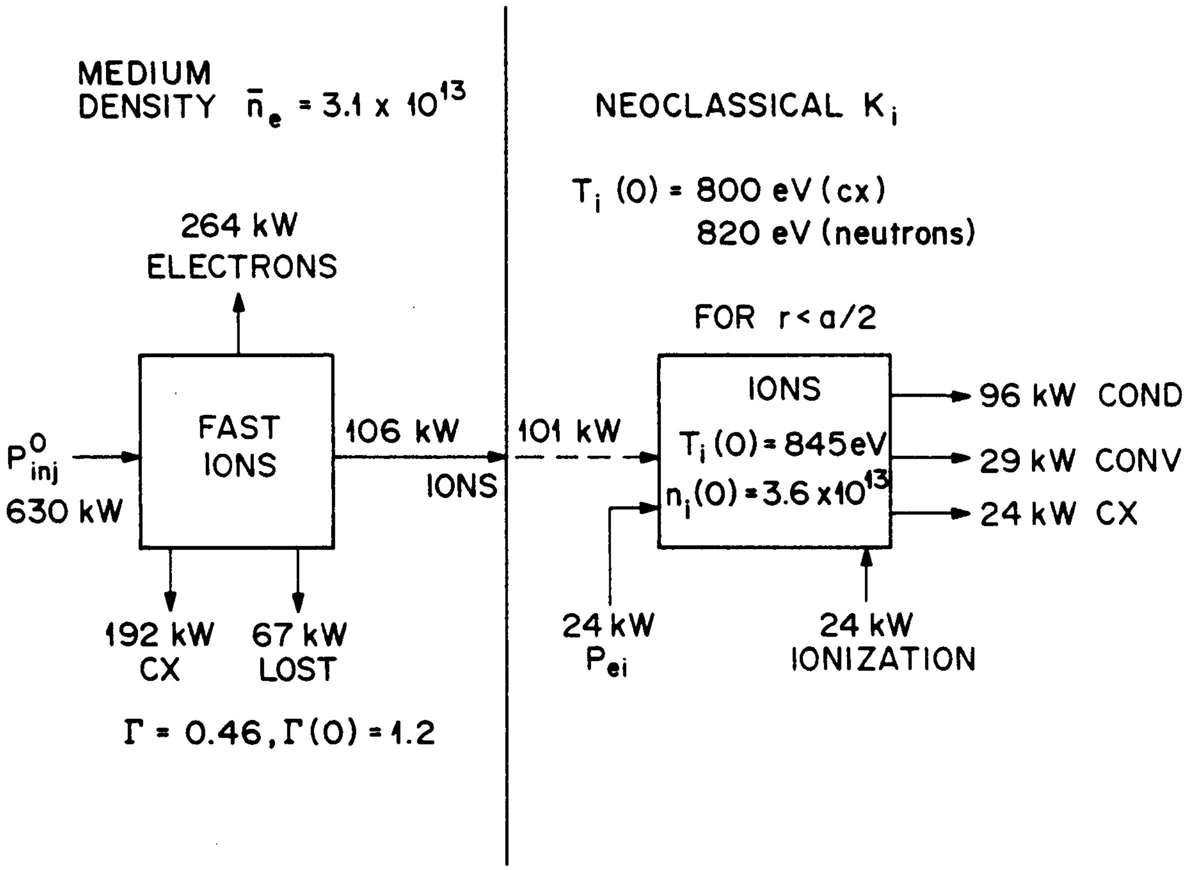

Figure 6-10. Details of ion power balance for medium density case. Neoclassical heat conduction was assumed, and the neutral density chosen to reproduce the measured ion temperature. Loss of fast ion energy is predominantly through charge exchange.

We conclude from these cases that ion confinement is again consistent with neoclassical transport theory, at least in the high density regime, where the role of charge exchange losses is minimal. At low and moderate densities, the confinement is quite sensitive to charge exchange losses. The neutral densities inferred by CX diagnostics undoubtedly lead to underestimates of the actual losses. The 2D neutrals calculations support this conclusion, but the model does not yet provide sufficient accuracy to make a reliable correction to the measurements. Clearly there is a need for toroidally resolved neutral density measurements, particularly in proximity to gas valves and limiters, to improve the estimates of charge exchange losses.

6.3 OTHER RESULTS

The results presented so far, and indeed the bulk of this report, have been concerned with the measurement of ion temperature by CX analysis. While this is certainly the most important contribution made by this diagnostic, there is other information which may be obtained as well, particularly in neutral beam injection experiments. Examples of this type of data are presented in this section; at this time, they are not well developed because they require more investigation and additional diagnostic information which has not been available to date. However, they illustrate some of the more specialized topics which may be addressed by CX and indicate some of the studies to be pursued further on ISX-B in the near future.

6.3.1 Anomalous Structure in the Neutral Spectrum

In Section 2.1 it was emphasized that one advantage of CX analysis is its ability to measure, albeit in a chord-averaged sense, the ion distribution function as opposed to moments or other velocity space integrals. In most cases, Maxwellian behavior is observed, at least in the bulk ions. However, a few instances of non-thermal behavior have been observed. One such example is given in Fig. 6-11: this experiment is the medium-density case of the preceding section and the figure is equivalent to Fig. 6-7, except that two additional ion temperature plots have been added. These are a second CX-inferred curve, where the data was fit between 0.5 and 6.0 keV instead of the original 0.5-3.0 keV, and a plot of values inferred by absolute neutron flux analysis. The results all converge in the latter half of the injection pulse, but earlier, the different interpretations disagree in such a way as to suggest the existence of an enhanced tail on the thermal deuteron distribution. This conclusion is verified by examination of the thermal spectrum itself, shown in Fig. 6-12a, which shows the distortion quite clearly 20 ms after the start of injection and a well-behaved spectrum 65 ms later. We note that the early injection phase was accompanied by a monotonic build-up of the density; thus we might inquire whether the ion tail was a consequence of the low density or a phenomenon associated with the neutral beam turn-on per se. Other data bear out the former explanation; in cases where the density remained low throughout the injection phase, such as the low density case of the previous

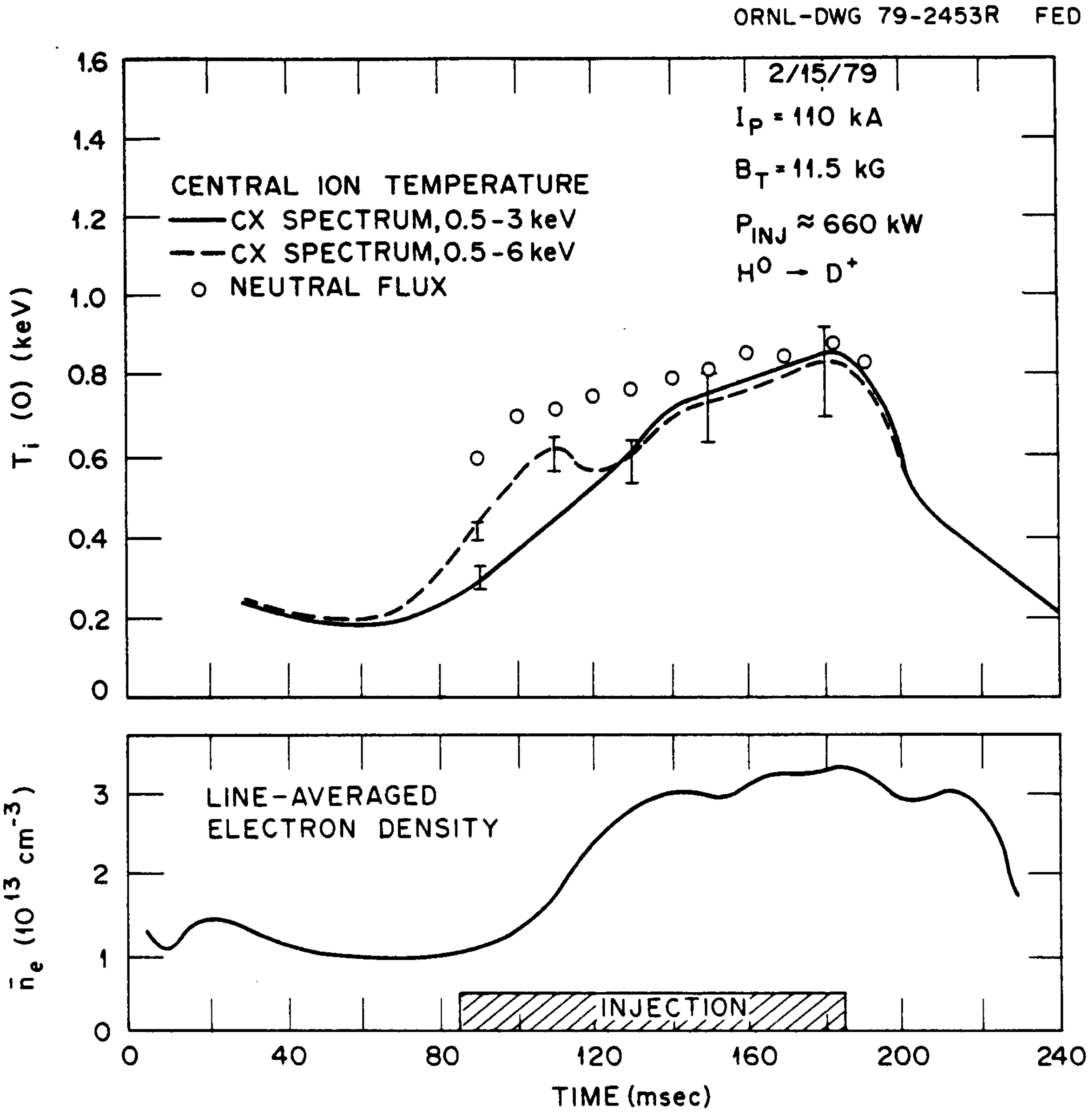

Figure 6-11. Model dependence of inferred ion temperature due to spectral distortion.

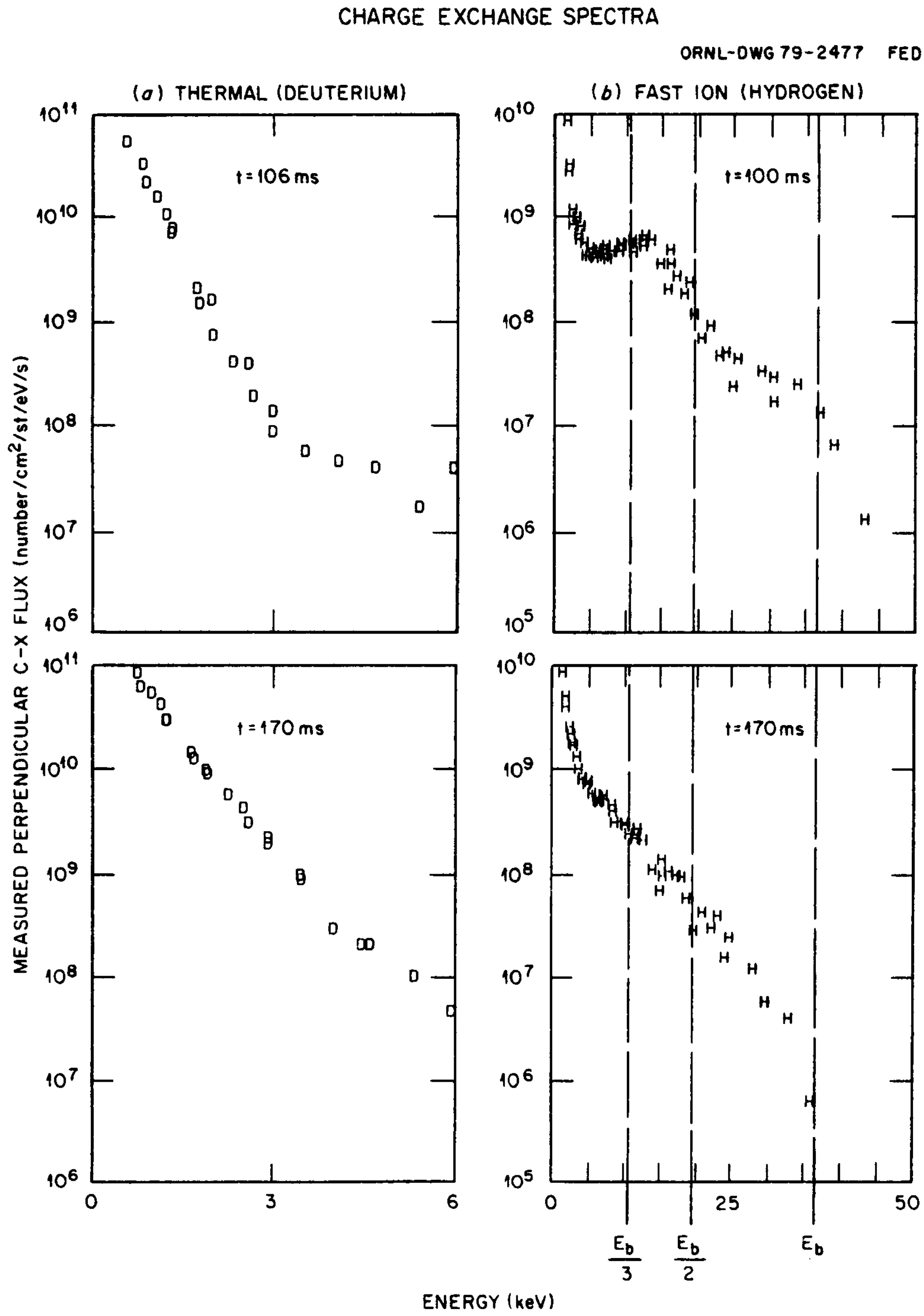

Figure 6-12. Thermal and fast ion spectra showing early and late time behavior. Distortion in thermal (a) spectrum leads to erroneous ion temperature measurement if included in the analysis (cf. Fig. 6-11). Early fast ion spectrum (b) shows beam species related structure, but relaxes later in time.

section, both the energy band-dependent ion temperature interpretations and the distorted spectra themselves, were obtained. Presumably this is a beam-driven distortion which is observable at low densities because of the longer relaxation times for non-thermal distributions. However, the exact mechanism for such a distortion is not explained at this time, although qualitatively similar phenomena have been observed in other experiments, for example, T-11[13] and ATC.[12]

In the same medium-density experiment, some interesting behavior, illustrated in Fig. 6-12b, was observed in the fast ion spectrum as well. At early times, a remarkable degree of structure, for a perpendicular spectrum, is exhibited. Features apparently corresponding to the one-third, one-half, and full energy components of the neutral beams are observed, while later in the discharge no such structure is seen. Once again, the effect appears to be associated with low density, in view of its disappearance in the above case, and the fact that it is not seen in other cases, where the density is higher throughout the shot. One possible explanation of this effect is that it is a normal manifestation of the classical fast ion behavior.[61] Pitch angle scattering, which is governed essentially by a diffusion term in the Fokker-Planck equation, causes fast ions to be seen at near-perpendicular pitch angles before they have slowed down appreciably, the latter process being governed by a dynamical friction. Later in time, the spectrum is filled in by older fast ions which have had a chance to slow down. Moreover, after the beam turns off, the spectrum collapses from the high energy end, an observation which is consistent with this classical interpretation. More detailed study of fast ion behavior requires information on the tangential spectrum as well as the perpendicular.

6.3.2 Ripple-Induced Fast Ion Loss

One unique component of the ISX-B experimental program is the study of ripple-assisted injection and of field ripple effects in general. For these purposes a pair of coils has been installed underneath the tokamak which, when energized, produce a local, poloidally asymmetric perturbation in the toroidal field.[62] Later, a vertical neutral beam injector will be incorporated in order to perform an experimental test of ripple-assisted injection, a scheme which utilizes the vertical drift of ions trapped in a local ripple to transport fast ions ionized near the outside of the plasma into the center.[63] If successful, it would reduce the neutral penetration, and hence energy, requirements for neutral injection in TFTR and other large devices.

Before attempting such experiments, it has been necessary to investigate the effects of such a perturbation on the plasma itself and, in particular, on fast ion confinement. Such effects are important from the standpoint of bundle divertors as well as ripple injection, both of which incorporate toroidally asymmetric ripples. One result of these preliminary studies is displayed in Fig. 6-13, which shows time histories of the plasma current and injection and ripple field timing. Also shown are time histories of fast ion

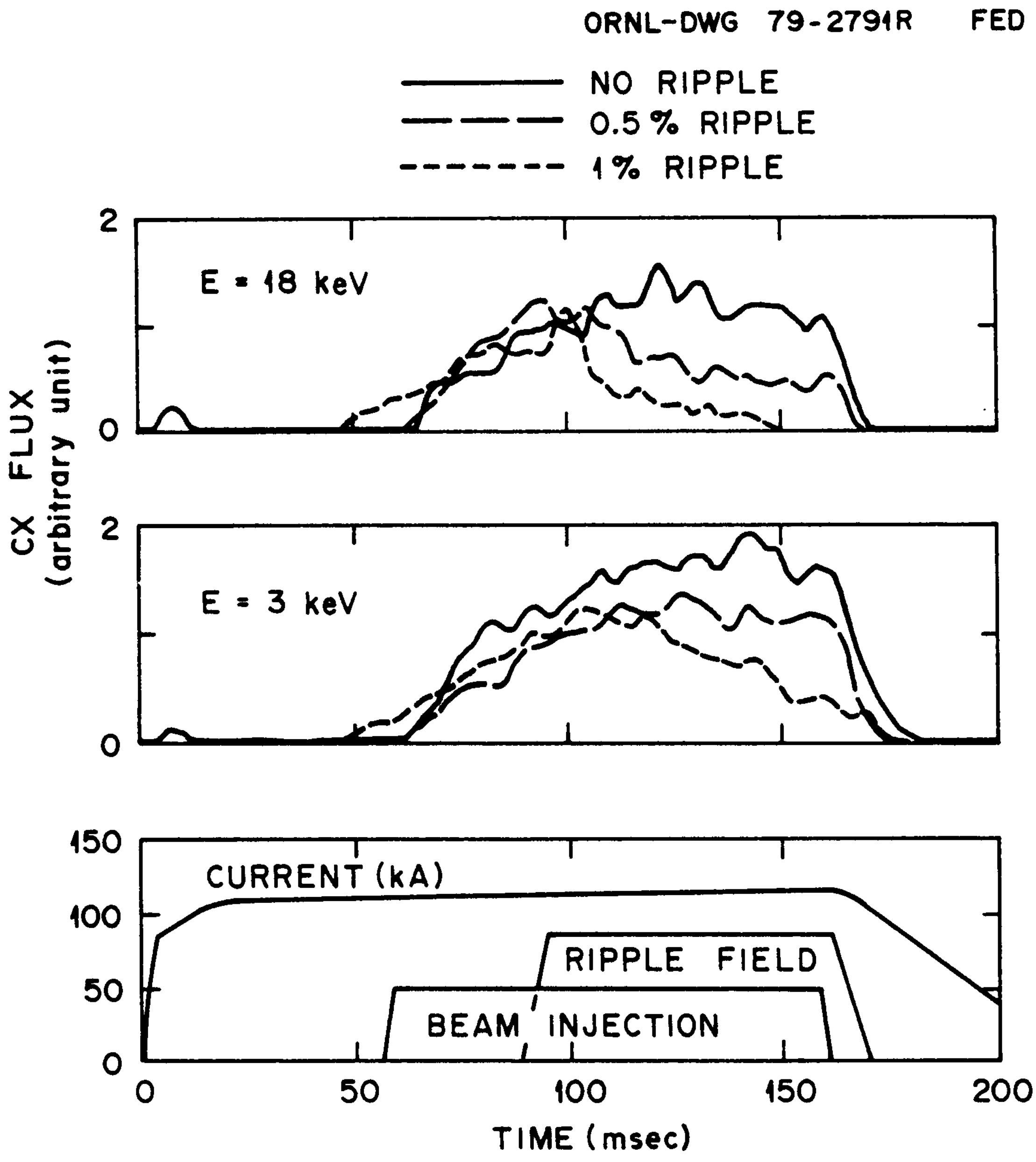

Figure 6-13. Time histories showing loss of confined fast ions due to introduction of field ripple.

charge exchange flux at energies of 3 keV and 18 keV for ripple strengths of 0, 0.5% and 1.0% of toroidal field at the midplane. The decrease in these signals after the ripple is turned on reflects a partial loss of fast ion confinement, which worsens with increasing energy and increasing ripple strength. The effects on overall plasma equilibrium, i.e. density and ion and electron temperatures, were somewhat less severe. These studies are still in progress and will also benefit from tangential and variable-chord fast ion measurements.

CHAPTER 7

MIXED PLASMA EXPERIMENTS: PELLET FUELING ON ISX-B

Recent experiments in ISX-B have demonstrated the effectiveness of plasma fueling by injection of solid hydrogen pellets.* A pneumatic accelerator has been used to inject pellets of up to 1 mm diameter at velocities up to 10^5 cm-s^{-1} into ISX-B plasmas. The principal results to date have been clear observations both of full pellet ablation in the discharge and of increased plasma density due to the ablated pellet. In contrast to experiments on ORMAK, in which smaller ($\leq$ 0.21 mm dia.) and slower ($<10^4$ cm-s^{-1}) pellets penetrated only a few centimeters with no observable fueling,[22] quite the opposite problem has been encountered in ISX: pellets are often observed to completely traverse the plasma, only partially ablated, and to produce a gas burst upon impact with the distant wall. Positive results, that is, full ablation and stable density increase, have been obtained under two general types of operating conditions: 1) ohmic heated discharges in which the initial density is low and the electron temperature high ($\geq$ 1 keV) and 2) neutral beam heated discharges.

---

*The principal investigators in these studies are S. L. Milora and C. A. Foster (ORNL Fusion Energy Division, Plasma Technology Section), and C. E. Thomas (M.I.T.).

In these experiments, hydrogen pellets (and neutral beams) have been injected into deuteron plasmas. Thus, in the ohmic-heated cases, the mass-energy neutral analyzer effectively distinguishes between the pellet-introduced ions and the target ions. In the beam-heated cases, beam- and pellet-introduced ions are both of the same isotope, but the most energetic ions, at least, are disinguishable as fast ions; thus a partial identification of all three components may be made. Mass-resolved CX measurements made by the author therefore provide some unique insight in these experiments and we consider them in this chapter. Comprehensive analysis of the pellet studies is outside the scope of this report, however, so we shall discuss only the CX data and the conclusions which may be drawn from them.[64]

7.1 OHMICALLY HEATED PLASMAS

In this section we present results from pellet fueling experiments in ohmically heated discharges in ISX-B. The experiment was carried out under conditions found most conducive to complete pellet ablation, namely high current (140 kA) and toroidal field (1.48 T), and low initial density ($<10^{13}$ cm^{-3}). Pellets were injected at t = 100 ms, where the shot duration was 150 ms. A clear increase in the line-averaged density was observed using the vertical 2 mm microwave interferometer, but unfortunately, a quantitative estimate of the increase was impossible because of the difficulty in following such a large and rapid density change with the 2 mm system. Data from the FIR interferometer and Thomson scattering system were unavailable in this experiment.* It is not yet clear whether high electron temperatures (>1 keV) or runaway electrons, both of which are associated with low-density plasmas, are responsible for the ablation in this case.[65]

Data from the CX analyzer, displayed in Fig. 7-1, shows the fueling effect in terms of hydrogen ions appearing immediately after pellet injection. Their neutral fluxes build up to a maximum value in 20-30 ms, which probably reflects the time taken for the initially cold pellet ions to be heated by the electrons to plasma temperature. Thereafter, they either remain roughly constant or decay slowly, indicating that the hydrogen ions are well-confined for the remainder of the shot. It must be recognized, however, that these are chord-averaged signals which naturally embody effects of the instantaneous neutral density, and ion density and temperature profiles, which are not well-characterized in this case; thus their interpretation is not unambiguous.

The deuterium fluxes shown in Fig. 7-1 exhibit some interesting characteristics, also. Pellet injection is followed by a nearly total disappearance of these signals, then a roughly linear build-up for the remainder of the discharge, by which time they have reached a level greater than or equal to their pre-pellet levels. One possible

---

*However, a recent repetition of the experiment, with these systems in operation, essentially confirms the original results, and indicates a three- to four-fold line-averaged density increase, to about 3.5×10^{13}.[66]

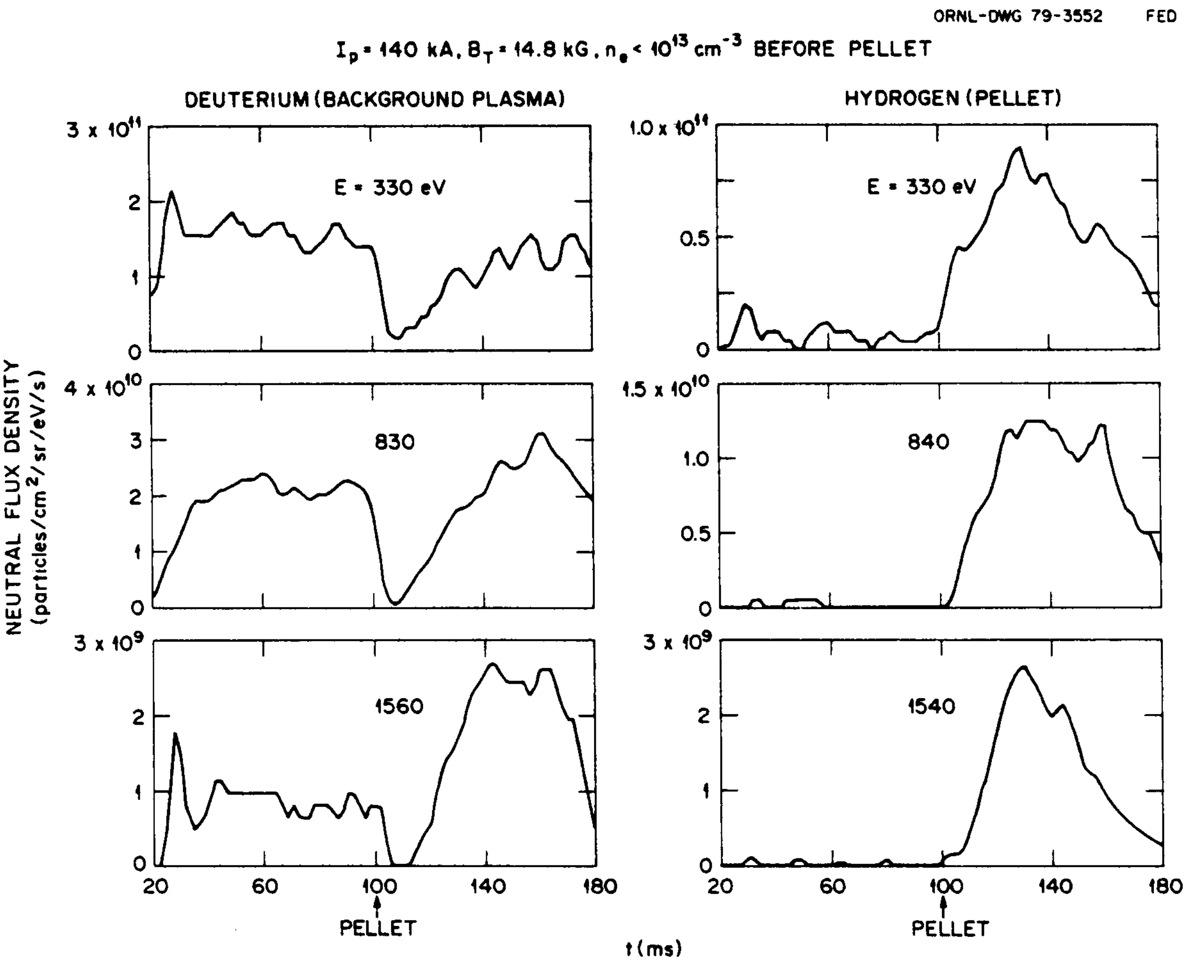

Figure 7-1. Time histories of pellet (H) and background (D) neutral fluxes for Ohmic discharges in ISX-B.

explanation for the disappearance is that the deuterons quickly equilibrate (τ_{eq} = 20 μs) with the cold protons, and thus cannot be seen at the energies detectable by the neutral analyzer. Another is found in the dynamics of pellet ablation: theory and experiment both indicate the presence of a dense neutral cloud of ablated material surrounding the pellet.[22] Thus, one might expect thermal deuterons to charge exchange with atoms in this cloud, resulting in an instantaneous exchange of the hot deuteron population for a cold proton population. In either case, the deuterons are later restored by the continuing gas feed and possibly by wall recycling, and reheated by ohmic heating power channeled through the electrons. One might wonder whether the CX analyzer could detect the large burst of neutrals which result from the second scenario, but again, this is a highly localized neutral source at the pellet location only, and as the CX system is approximately 90 degrees removed from the pellet apparatus, no such signal has been observed. On the other hand, the energy released by the escaping neutrals in such an exchange ought to be observable by a pyroelectric radiometer which views a region of the plasma through which the pellet passes. Since no such result is obtained,[67] the second explanation seems the less likely.

Ion temperatures computed from the hydrogen and deuterium flux spectra by the AS method are plotted in Fig. 7-2. AS analysis was used because of the aforementioned uncertainties in the density and the profiles and to avoid results which might thus appear as artifacts of the analysis. The AS analysis, of course, fails to

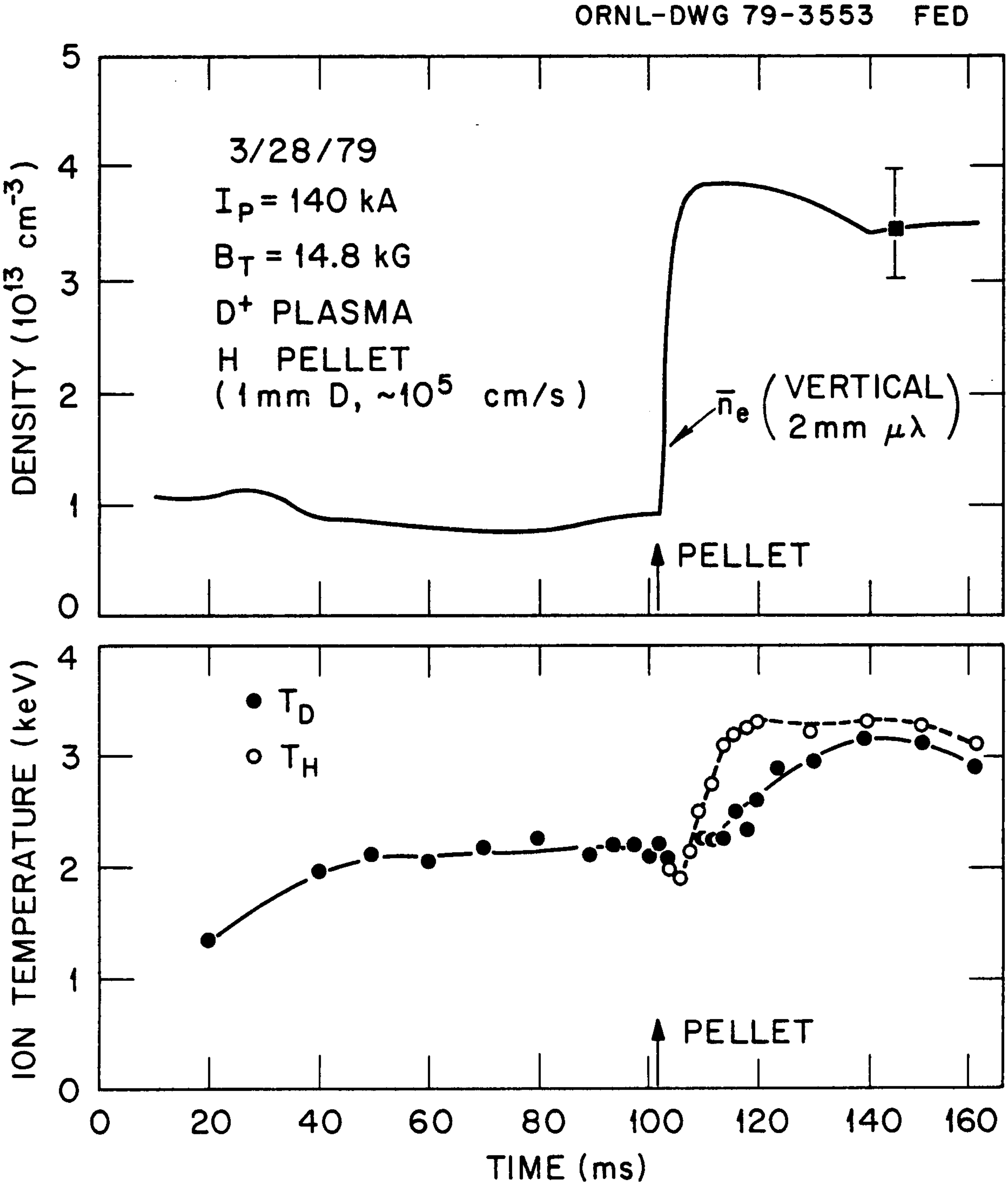

Figure 7-2. Ion temperature and density histories for pellet fueling of Ohmic discharges. AS analysis was used because of uncertainties in the density measurement. True ion temperature after pellet injection is higher than shown.

account for the profile and neutral attenuation effects, but is a more direct indication of the behavior of the CX data themselves. Before pellet injection, the discharge reaches an equilibrium having a deuteron temperature of about 200 eV; the proton temperature is unmeasurable due to the very weak signal strength. After pellet injection, the proton temperature rises within about 20 ms, as suggested by the flux signals, to a value of about 325 eV. The deuterons, once their signals return, also rise in temperature, somewhat more slowly than the protons, to about 310 eV. The higher temperatures at the end of the discharge are most likely due to the increased density, which results in more of the ohmic heating power being transfered to the ions.

7.2 NEUTRAL BEAM HEATED PLASMAS

With pellet fueling in neutral beam heated discharges, results similar to those of the ohmic heating cases were obtained from the CX analyzer. Deuterium and hydrogen neutral flux time signals are again displayed, in Fig. 7-3. Again, there is a sudden drop in the deuteron signal in evidence, though not as complete as with ohmic heating alone, and the subsequent recovery is considerably faster as well (within 10 ms). This may be due to the fact that the pellet penetration was not as deep and that more power was available to reheat the ions afterward.

In Fig. 7.3f, a hydrogen signal reflecting typical behavior of the flux at fast ion energies is seen. After beam injection begins, there is a roughly linear increase for approximately 45 ms, until it

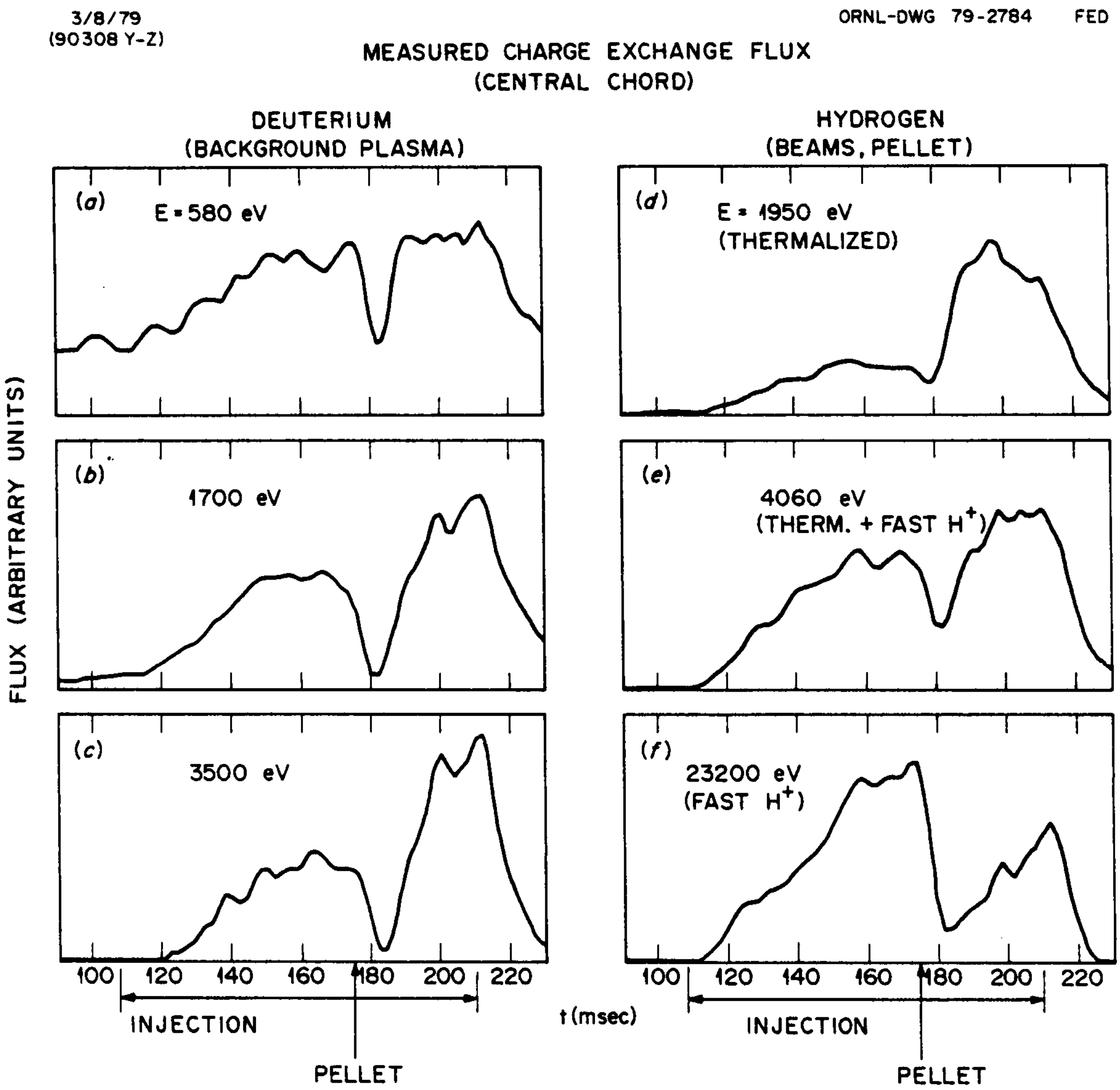

Figure 7-3. Time histories of pellet (H) and background (D) neutral fluxes for injected discharges in ISX-B.

reaches a steady state level. The pellet causes a dramatic drop in this signal, presumably due to the interaction of the fast ions with the ablation cloud, followed by a renewed buildup of the fast ion distribution, exactly repeating the initial phase of the injection pulse. In the low-energy hydrogen signal (Fig. 7-3d), the evolution of a thermalized beam-introduced ion population is initially observed. Pellet arrival is followed by only a slight drop in flux, then a large and immediate increase to a level about four times that which preceded the pellet, reflecting, as before, the thermalization of pellet-introduced protons, and possibly indicating a rapid thermalization of the fast ions as well. At intermediate energies (Fig. 7-3e), a combined effect is observed: both the drop seen in the fast ion flux and the over-recovery seen in the warm ion flux are found here. The time scale of the recovery is much faster than signal's own initial buildup, and slightly slower than that of the warm ion signal. We conclude that the recovery phase represents both thermalized pellet ions heating up and beam ions replenishing the fast ion population "from above" in energy.

The ion temperature too exhibits a trend similar to that of the ohmic heating cases, as shown in Fig. 7-4. Because more reliable density information was available in this case, MF analysis was used. From it, we infer a rather sizable ion temperature increase beginning at the time of pellet injection. AS analysis of the same data also gives a temperature increase, but only of approximately 10%. As before, the higher temperature is due in part to the increased

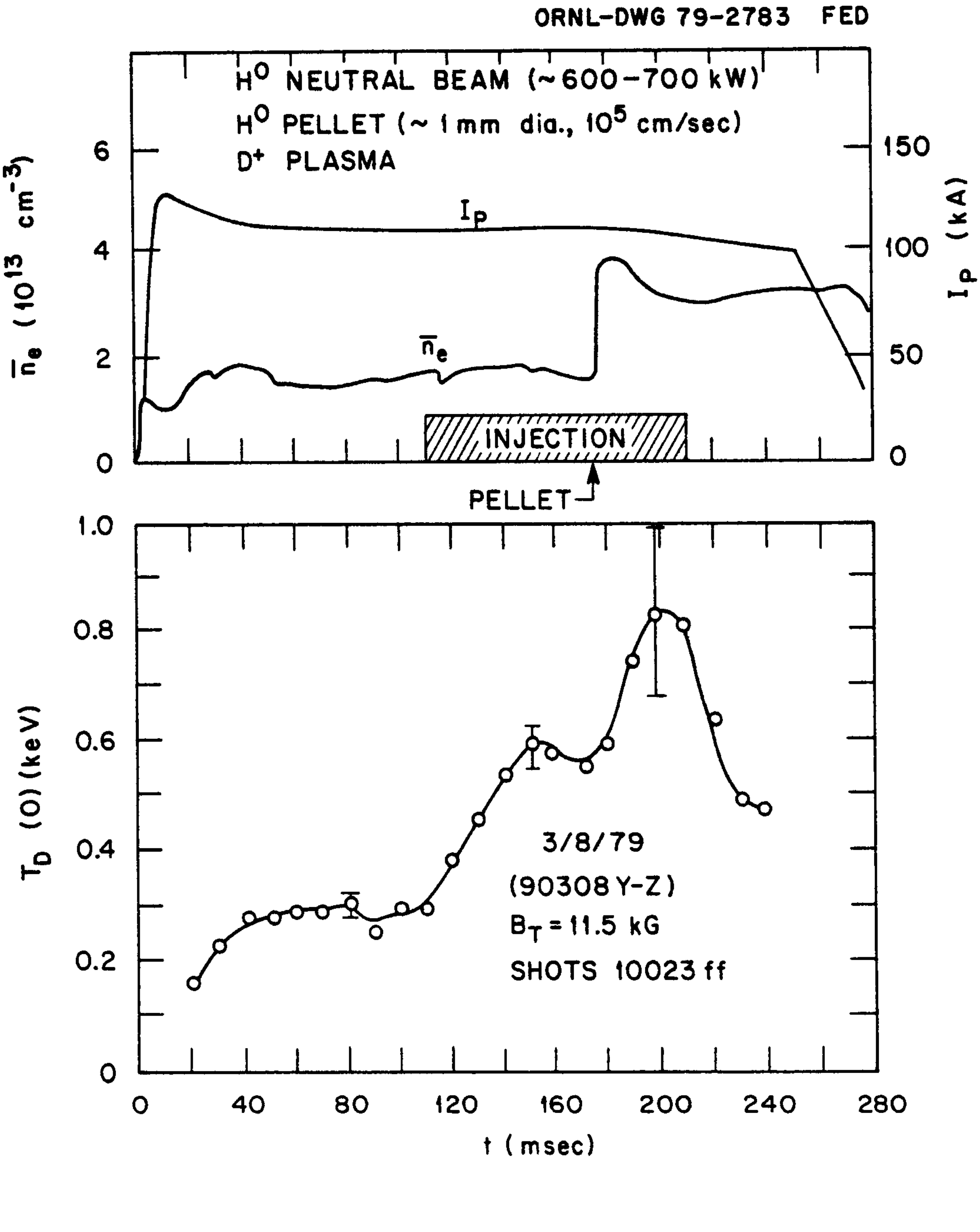

Figure 7-4. Ion temperature, density, and plasma current histories for pellet fueling of injected discharges. MF analysis was used in this case.

density producing better transfer of electron energy to the ions. Additionally, the higher density would be expected to lead, in this case, to improved beam trapping (ionization) and reduced charge exchange losses, as was discussed in Chapter 6.

These results indicate that pellet ablation is enhanced by neutral beam injection, as only partial ablation was obtained in the same discharge, but without beams. It is clear that there is a direct interaction between the thermal and fast ions and the pellet; this results in a dramatic drop in fast ion CX signal which may represent either an undesirable loss of fast ions or a very desirable thermalization of the fast ion population. The exact contribution of the beams and fast ions to the ablation process is not known. Fueling is reflected in increased hydrogen signals at low energies, with evidence of good particle confinement, in common with the ohmic heating experiments.

LIST OF REFERENCES

LIST OF REFERENCES

1. Artsimovich, L. A., Nucl. Fusion 12 (1972) 215.

2. Furth, H. P., Nucl. Fusion 15 (1975) 487.

3. Artsimovich, L. A. et al., in "Plasma Physics and Controlled Nuclear Fusion Research" (Proc. 3rd Int. Conf., Novosibirsk, 1968) 1 (1969) 17.

4. Swain, D. W., Smith, T. E., Sigmar, D. J., Murakami, M., ORNL/TM-5985 (1977).

5. Jassby, D. L., Cohn, D. R., Parker, R. R., Nucl. Fusion 16,6 (1976) 1045.

6. Murakami, M., Burrell, K. H., et al. in "Plasma Physics and Controlled Nuclear Fusion Research" (Proc. 7th Int. Conf., Innsbruck, 1979) 1 (1979) 269.

7. Isler, R. C., Crume, E. C., Howe, H. C., Nucl. Fusion 19,6 (1979) 727.

8. Equipe TFR, in "Plasma Physics and Controlled Nuclear Fusion Research" (Proc. 6th Int. Conf., Berchtesgaden, 1976) 1 (1977) 69.

9. Colchin, R. J., Jernigan, T. C., J. Nucl. Mater. 63 (1976) 83.

10. Murakami, M., Neilson, G. H., Howe, H. C., Jernigan, T. C. et al., Phys. Rev. Lett. 42 (1979) 655.

11. Berry, L. A. et al., in "Plasma Physics and Controlled Nuclear Fusion Research" (Proc. 6th Int. Conf., Berchtesgaden, 1976) 1 (1977) 49.

12. Ellis, R. A., Eubank, H. P., Goldston, R., Smith, R. R., Nagashima, T., Nucl. Fusion 16 (1976) 524.

13. Vlasenkov, V. S. et al., in "Plasma Physics and Controlled Nuclear Fusion Research" (Proc. 6th Int. Conf., Berchtesgaden, 1976) 1 (1977) 49.

14. Neilson, G. H., Lyon, J. F., Murakami, M., in "Heating in Toroidal Plasmas" (Proc. 2nd Joint Varenna-Grenoble Int. Symposium, Grenoble, 1978) 1 (1978) 49.

15. Eubank, H. P., Goldston, R. J., et al., in "Plasma Physics and Controlled Nuclear Fusion Research" (Proc. 7th Int. Conf., Innsbruck, 1978) 1 (1979) 167.

16. Haselton, H. H. et al., in "Heating in Toroidal Plasmas" (Proc. 2nd Joint Varenna-Grenoble Int. Symposium, Grenoble, 1978) 1 (1978) 67.

17. Charlton, L. A., Swain, D. W., Neilson, G. H., ORNL/CSD/TM-92 (1979) (to be published in IEEE Trans. Plasma Sci.).

18. Golant, V. E. in "Heating in Toroidal Plasmas" (Proc. 2nd Joint Varenna-Grenoble Int. Symposium, Grenoble, 1978) 2 (1978) 149.

19. Alikaev, V. V., in "Heating in Toroidal Plasmas" (Proc. 2nd Joint Varenna-Grenoble Int. Symposium, Grenoble, 1978) 2 (1978) 307.

20. TFR Group, in "Heating in Toroidal Plasmas" (Proc. 2nd Joint Varenna-Grenoble Int. Symposium, Grenoble, 1978) 2 (1978) 207.

21. "Proceedings of the Fusion Fueling Workshop" (Princeton, N. J., 1977) U.S.D.O.E. (1978).

22. Foster, C. A., Colchin, R. J., Milora, S. L., Kim, J., Turnbull, R. J., Nucl. Fusion 17 (1977) 1067.

23. Kim, J. et al., ORNL/TM-6896 (1979).

24. Osher, J. E. in Plasma Diagnostic Techniques, Huddlestone, R. H. and Leonard, S. L., eds., Academic Press, New York (1965) 517-601.

25. Petrov, M. P., Sov. J. Plasma Phys. 2,3 (1976) 201.

26. Lyon, J. F. et al., in "Fusion Energy Division Annual Progress Report for Period Ending December 31, 1976", ORNL-5275 (1977) 62-63.

27. Kislyakov, A. I. et al., IPP 2/230 (Max Planck Institut fur Plasmaphysik Report), 1976.

28. Afrosimov, V. V. et al., Sov. Phys. Tech. Phys. 20,1 (1975) 33.

29. Barnett, C. F. et al., "Atomic Data for Controlled Fusion Research", ORNL-5206 1 (1977) A.4.2.

30. Hutchinson, D. P., Vander Sluis, K. L., ORNL/TM-5071 (1975).

31. Neilson, G. H., ORNL/TM-6823 (1979).

32. Berry, L. A. et al., in "Plasma Physics and Controlled Nuclear Fusion Research" (Proc 5th Int. Conf., Tokyo, 1974) 1 (1975) 101.

33. Medley, S. S., FRCR-125 (1976).

34. Davis, S. L., Medley, S. S., Brusati, M., PPPL-1478 (1979).

35. Girard, J. P. (C.E.N., Fontenay-aux-Roses), private communication.

36. Summer, D. D. R. (U.K.A.E.A., Culham) private communication.

37. Armentrout, C. J. (General Atomic Co.) private communication.

38. Mihalczo, J. T., Neilson, G. H., Lyon, J. F., Worsham, R. E., in "High Temperature Plasma Diagnostics" (Proc. 2nd Topical Conference, Santa Fe, 1978) LA-7160-C (1978) 105.

39. Baity, F. W., Quon, B. H., in "Fusion Energy Division Annual Progress Report for Period Ending December 31, 1976, ORNL-5275 (1977) 9.

40. Dandl, R. A. et al., ORNL/TM-6457 (1978) 21-29.

41. Barnett, C. F., Ray, J. A., Nucl. Fusion 12 (1972) 65.

42. Allison, S. K., Kamegai, M., Rev. Sci. Inst. 32,10 (1961) 1090.

43. Mullard type B419 are used.

44. Siemens type EA218 is used.

45. Ray, J. A., Barnett, C. F., IEEE Trans. Nucl. Sci., NS17,1 (1970) 44.

46. Dushman, S., Scientific Foundations of Vacuum Technique, Wiley, New York (1962) 90-91.

47. Barnett, C. F. et al., "Atomic Data for Controlled Fusion Research", ORNL-5206 1 (1977) A.4.4, A.5.28.

48. Bandet, R., Dupas, L. EUR-CEA-FC-662 (1972).

49. Uckan, N. A., Tsang, K. T., Callen, J. D., ORNL/TM-5438 (1976).

50. Dnestrovskij, Yu. N. et al., Nucl Fusion 19, 3 (1979) 293.

51. Gilligan, J. G. et al., Nucl. Fusion 18, 1 (1978) 63.

52. Burrell, K. H., J. Comput. Phys. 27,1 (1978) 88.

53. Hogan, J. T., Clarke, J. F., J. Nucl. Mater. 53 (1974) 1.

54. Kelley, G. G., private communication.

55. Modifications to NEUCG to handle volume sources were made by H. C. Howe.

56. Towner, H. H., Goldston, R. J., Bull. APS 24, 8 (1979) 1107.

57. Hinton, F. L., Hazeltine, R. D., Revs. Mod. Phys. 48 (1976) 239.

58. Dory, R. A., Peng, Y.-K. M., Nucl. Fusion 17,1 (1977) 21.

59. Callen, J. D. et al., in "Plasma Physics and Controlled Nuclear Fusion Research" (Proc. 5th Int. Conf., Tokyo, 1974) 1 (1975) 645.

60. Neilson, G. H., Lyon, J. F., in "Proceedings of the Fusion Fueling Workshop" (Princeton, N. J., 1977) U.S.D.O.E. (1978) 39.

61. Goldston, R. J. (PPPL) private communication.

62. Goldston, R. J. et al., "Engineering Problems of Fusion Research" (Proc. 7th Symposium, Knoxville, 1977) (1977) 1333.

63. Jassby, D. L., Goldston, R. J., Nucl. Fusion 16,4 (1976) 613.

64. A publication on ISX-B pellet fueling experiments is forthcoming.

65. Milora, S. L., private communication.

66. Wilgen, J. B., private communication.

67. Bush, C. E., private communication.

68. Banford, A. P., The Transport of Charged Particle Beams, Spon, London (1966) 63-76.

APPENDIXES

APPENDIX A

OPTICAL PROPERTIES OF MAGNETOSTATIC MOMENTUM ANALYZERS

In this appendix we discuss the first order optical properties of typical magnetic field configurations used for ion momentum analysis, following Banford.[68] Unfortunately, it is found that these effects tend to be weak in configurations where they might be useful. Moreover, focussing in one dimension is generally accompanied by defocussing in the other dimension, a disadvantage when the detector to be used is a "point" rather than a "line." For these reasons we conclude that there is no advantage in using these subtle effects in CX spectrometers, and indeed they may be detrimental unless precise field shaping is incorporated.

Consider an ion momentum spectrometer consisting of a pair of identical pole faces of arbitrary shape, separated by a vacuum gap (g cm) which is short compared to transverse pole face dimensions, (L cm; g << L). A magnetic field normal to the pole faces is imposed in the gap; to a zeroth approximation, the field is uniform (B_o Tesla) in the gap and zero elsewhere. The trajectory of an incident ion of momentum p in the midplane of this system may be trivially constructed: it is linear outside the magnet and circular with radius of curvature $R = p/eB_o$ in the magnetic field, as depicted in Fig. A-1a.

Next consider first order [O(g/L)] departures from this idealized trajectory due to fringing fields near the edges of the magnet and divergence in the incident beam. Banford derives the

ORNL-DWG 79-3554 FED

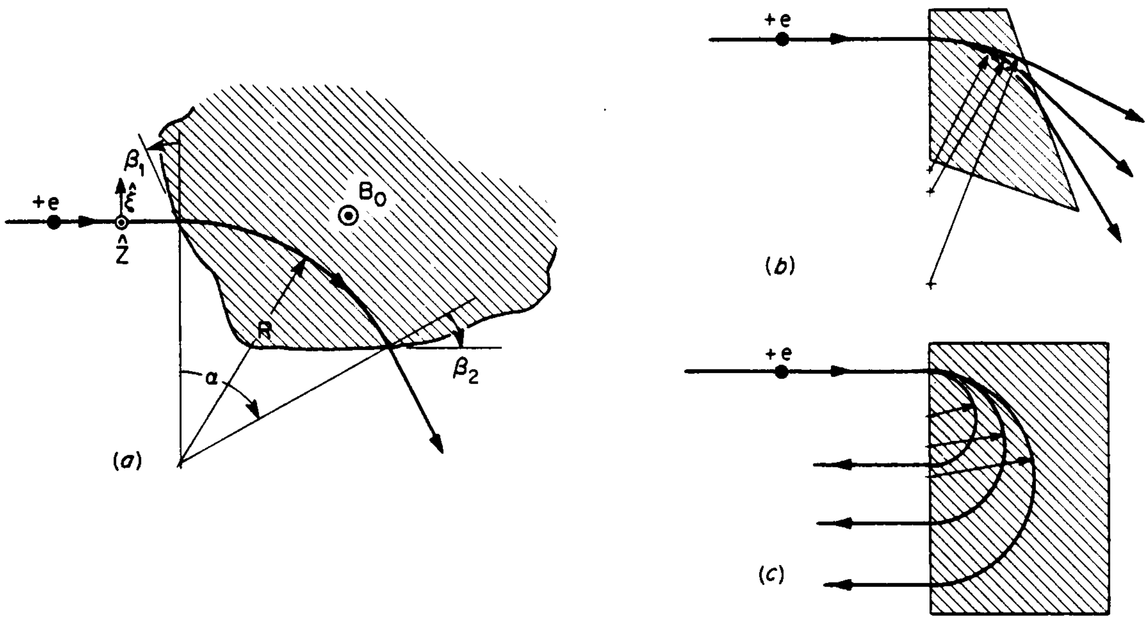

Figure A-1. Geometry for analysis of magnetic momentum analyzers. (a)definition of symbols used in text. Small (b) and large (c) angle momentum analyzers defined.

optical properties of this system by means of a ray tracing treatment of displacements in the two coordinates normal to the zero order trajectory, ξ and z, where ξ is in the plane of the trajectory. In terms of the three angles α, β_1, and β_2 defined in Fig. A-1a, these properties may be represented by two systems of lenses whose axes are the developed zero order trajectory. These models are given in Figs A-2a and A-2b for ξ and z displacements respectively. Clearly the edge optics depend on the sign of the angle with which the trajectory enters and leaves the magnet; focussing in one dimension is accompanied by defocussing in the other. Thus it is difficult (though not impossible in principle, since the bulk effect can be used to focus in ξ while the edges focus in z, with proper choice of angles for all values of R) to take advantage of these properties when the beam must be focussed onto "point" detectors, such as channeltrons, as opposed to a surface.

Using the angle α, a momentum analyzer can be classified as either a small angle or large angle deflector, as shown in Figs. A-1b and A-1c. In the former, an example of which is the Soviet analyzer[28] in the mass-energy configuration, R is large compared to the magnet dimension L. The particles are only deflected through a small angle in the magnet and most of the trajectory separation for different momenta occurs beyond the magnet. Here it would be useful to be able to focus the beamlets, but from Fig. A-2 we see that the characteristic focal lengths are large multiples of R. Hence the focussing is quite weak; for it to be of any use would require large

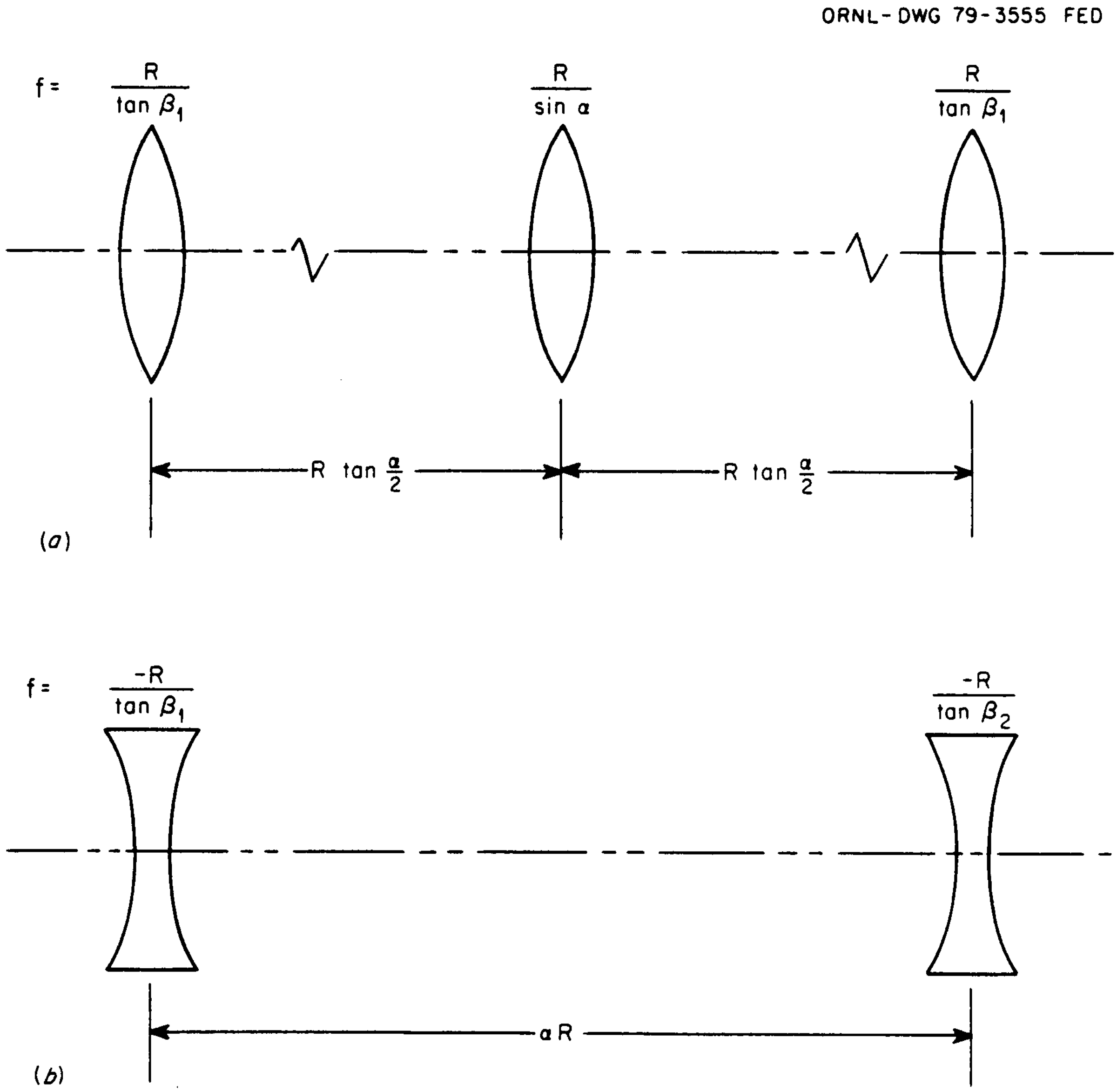

Figure A-2. Equivalent lens systems for magnetic analyzer optics. (a)in plane of trajectory. (b)normal to plane.

spacing between the magnet and detectors and elimination of any error fields (e.g. from coils or flux leakage) in the drift space.

In a large angle spectrometer, such as the 180 degree instrument described in Chapter 3, a large enough magnet (L >> R) is used that significant trajectory separation is obtained within the magnet itself. Detectors, or in this case the entrances to energy filters, may be located so as to intercept the ions where they leave the magnet. With $\alpha = 180^o$, particles enter and leave the normal to the pole face edge, so $\beta_1 = \beta_2 = 0$ and thus there are no first order optical effects due to the edge. The bulk effect is such that the entrance slit has an image at any exit slit. Thus the divergence of the emerging beam is no better or worse than that of the incident beam. This is quite acceptable, however, because focussing is not necessary due to the close proximity of the energy filters to the magnet.

APPENDIX B

ANALYSIS OF CYLINDRICAL ELECTROSTATIC ANALYZERS

The energy filters used for mass selection in the mass-energy analyzer are made from concentric pairs of cylindrically-shaped conductors subtending an arc of about 40 degrees. Voltages of about 0.1 × the desired particle energy are applied to the conductors to produce a radial electric field between them. A large energy dispersion (~33%) is obtained, enough to distinguish between momentum-analyzed ions of mass numbers 1 and 2, without the need for precise (non-linear) tracking between the magnetic and electrostatic fields. The trajectories of ions in this configuration are analyzed in this appendix.

We also ask whether stray fields from the magnet might produce an unacceptable distortion of the energy filter trajectories. It is shown that, while there is indeed such distortion, it occurs in such a way that it can be almost completely compensated by a constant correction factor to the theoretically determined plate voltage required to select ions of a particular energy. This fact makes the fringing field quite tolerable, and complicated field-shaping measures are thus unnecessary.

B.1 IDEALIZED CONFIGURATION

We use an idealized, but adequate, model of this device, as diagrammed in Fig. B-1. The voltages on the outer (+V) and inner (-V) plates are equal in magnitude and opposite in polarity to minimize any pre-acceleration of incident ions and to keep the

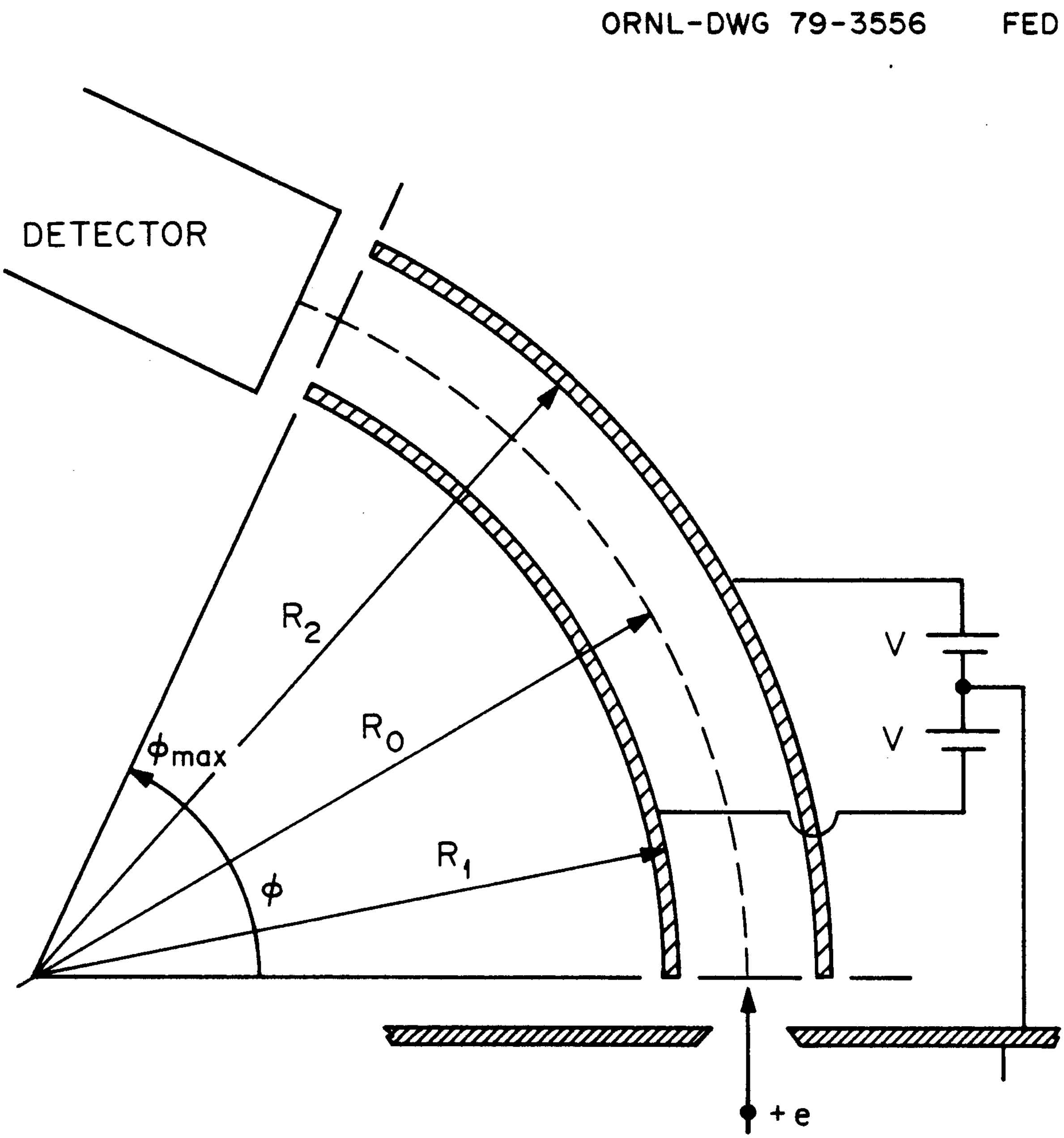

Figure B-1. Geometry and biasing for analysis of cylindrical electrostatic analyzers.

electrostatic fields as localized as possible. The radial motion of an ion of charge +e and energy E incident in the ϕ direction at $R = R_o$, $\phi = 0$, is governed by an effective potential which is the sum of the electrostatic and "centrifugal" potentials, given by Eq. B.1.

$$U = 2\, E_o\, \ell n\, \left(\frac{R}{\sqrt{R_1 R_2}}\right) + E\, \frac{R_o^2}{R^2} \qquad \text{B.1}$$

where $E_o = eV/\ell n(R_2/R_1)$. This can be approximated, to first order in the parameter $(R_2 - R_1)/(R_2 + R_1)$, by a parabolic well:

$$U = E_o\left(1 + \ell n\, \frac{ER_o^2}{E_o R_1 R_2}\right) + \frac{2E_o^2}{R_o^2 E}\left(R - R_o\sqrt{\frac{E}{E_o}}\right)^2 \qquad \text{B.2}$$

The potential function and its parabolic approximation are plotted in Fig. B-2 for a particle with energy $E = 1.1 \times E_o$. Its radial motion is a fractional cycle of a simple harmonic oscillation. From conservation of angular momentum, the angular velocity is found to be constant to first order, so the equations for the trajectory are given approximately by Eq. B.3

$$R = R_o\sqrt{\frac{E}{E_o}} + R_o\left(1 - \sqrt{\frac{E}{E_o}}\right)\cos\left(\frac{2E_o}{\sqrt{mE}\, R_o}\right)t \qquad \text{B.3a}$$

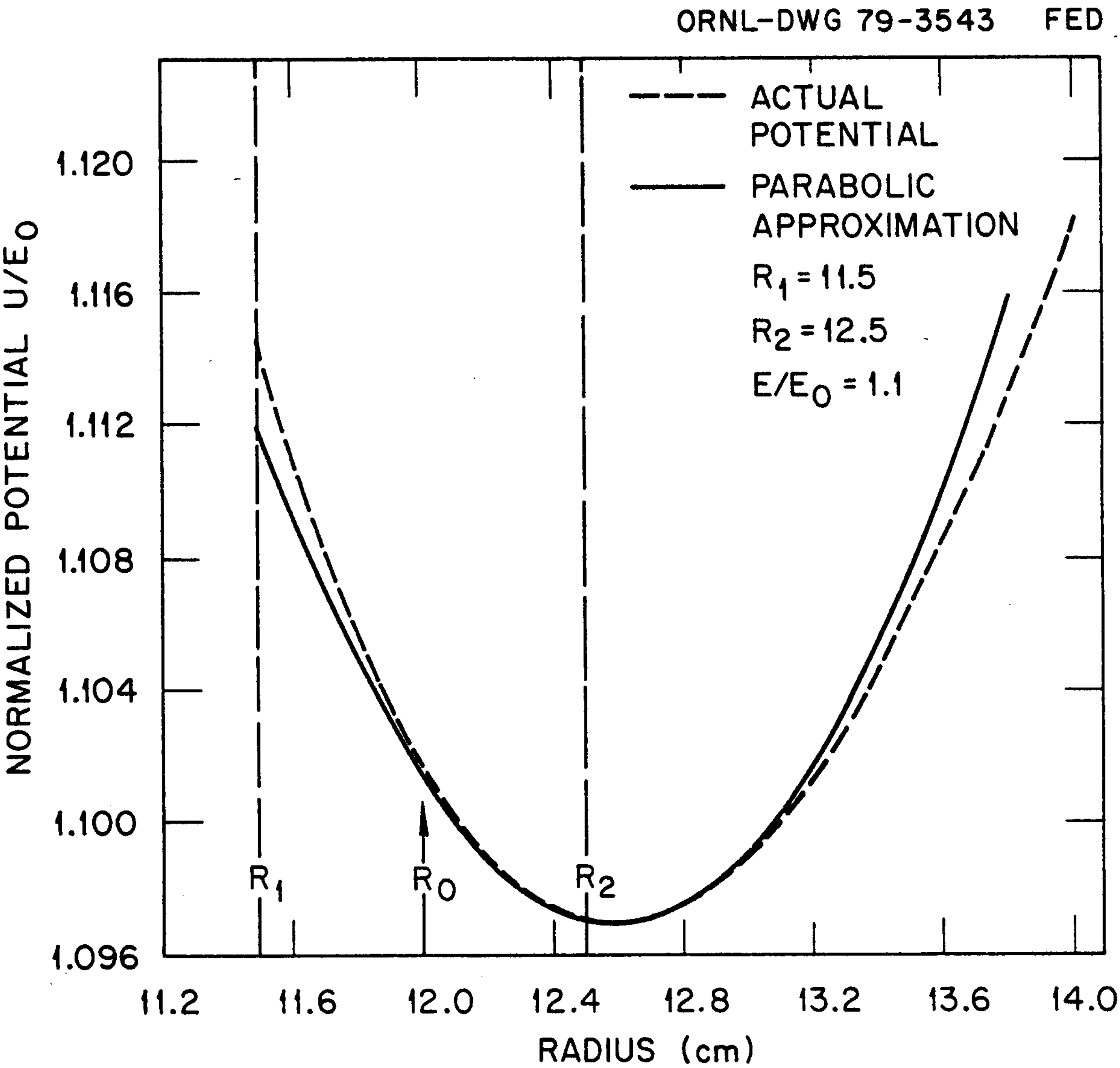

Figure B-2. Effective potential for radial motion in cylindrical analyzers. Actual potential and parabolic approximation are shown.

$$\dot{\phi} = \sqrt{\frac{2E}{m}}\,\frac{R_o}{R^2} \rightarrow \phi \cong \sqrt{\frac{2e}{m}}\,\frac{t}{R_o} \qquad \text{B.3b}$$

By now it is clear that E_o is actually the nominal pass energy of the filter, where the centrifugal and electrostatic forces balance such that the particle remains centered between the plates. The energy dispersion may be found by setting $\phi = \phi_{max}$ in Eq. B.3b and solving for E/E_o with $R = R_1$ and R_2. For the values in use, namely $R_1 = 11.5$ cm, $R_2 = 12.5$ cm, and $\phi_{max} = 0.71$ rad, we obtain $0.84 < E/E_o < 1.17$ so the full width dispersion, expressed by Eq. B.4, is about 33%.

$$\left(\frac{\delta E}{E}\right)_{FW} \cong 2\,\frac{R_2 - R_1}{R_o \phi_{max}^2} \qquad \text{B.4}$$

B.2 EFFECT OF WEAK, STRAY MAGNETIC FIELD

We now suppose that a weak magnetic field B_z is imposed parallel to the cylindrical plates, to simulate the symmetry plane fringing fields for the momentum analyzer. The field exerts on the particle a radial force $ev_\phi B_z$ which can be represented by an effective radial potential term

$$U_B = 2E\frac{R_o}{R_B}\,\ell n\,\frac{R}{\sqrt{R_1 R_2}} \qquad \text{B.5}$$

where $R_B = \sqrt{2mE}/eB_z$. Assuming the fringing field to be proportional to the gap field, R_B is proportional to the radius of curvature of the particle's trajectory in the momentum analyzer, which is a geometrical constant for each channel. Therefore R_B is a constant for any particle which reaches the filter, irrespective of its mass and energy.

The new total effective potential is obtained by subtracting Eq. B.5 from Eq. B.1 (since the magnetic force opposes the electrostatic force). This is minimized with respect to R to find the center of the potential well for particles of a particular energy, and this radius is equated to R_o to find the energy for which the trajectories are centered. This turns out to be $E = E_o/(1 + R_o/R_B)$, which implies that the voltages required for a given energy are a factor $(1 + R_o/R_B)$ greater due to the fringing field. In this analyzer the average fringing field is about 7-8% of the gap field (cf. Fig. 3-8), so the R_B are about 13 times the gap field radii of curvature, or about 33 to 111 cm. Since R_o = 12 cm, the corrected voltages required to select the desired energy should differ by about 10% to 37% from those computed in the idealized analysis. This agrees well with the empirical findings in Table 3-2. We further expect from these results that the voltage-to-energy ratios, once determined empirically, should be invariant with mass and energy, and this expectation is borne out as well.

VITA

George Hutchinson Neilson, Jr. was born in Medford, Massachusetts on July 23, 1949. He attended public schools in Wellesley, Massachusetts and Welland, Ontario, Canada, and was graduated from Washington Park High School in Racine, Wisconsin in June, 1967. He entered the Massachusetts Institute of Technology, Cambridge, Massachusetts, in September, 1967, and received the degrees of Bachelor of Science and Master of Science in Electrical Engineering in September, 1973. During that period, he was employed by the General Radio Company, Concord and Bolton, Massachusetts, as an M.I.T. Co-operative student; by the Lawrence Livermore Laboratory, Livermore, California, as a summer student; and by M.I.T.'s Research Laboratory of Electronics, as a Research Assistant.

The author was a Member of Technical Staff of the Hughes Aircraft Company, Torrance, California, from 1973 to 1974. In July, 1974, he joined the research staff of the Oak Ridge National Laboratory, Oak Ridge, Tennessee, as an experimental physicist in the ORMAK program. He entered the University of Tennessee, Knoxville, the same year, conducted his graduate research at ORNL, and received the Doctor of Philosophy degree with a major in Physics in December, 1979. Mr. Neilson remains on the ORNL staff as a Research Associate in the Fusion Energy Division, and is involved with the ISX experiment.

The author is a member of Tau Beta Pi and of the American Physical Society.

He is married to the former Linda Ruth Roy of Southbridge, Massachusetts, and has one daughter, Rebecca.